Spatially Controlled Reconstitution of PIP Lipid Synthesis and Small GTPase Activation on Supported Membranes

by

Sophia Doerr

A dissertation accepted and approved in partial fulfillment of the

requirements for the degree of

Doctor of Philosophy

in Biology

Dissertation Committee:

Dr. Melanie Spero, Chair

Dr. Scott Hansen, Advisor

Dr. Michael Harms, Core Member

Dr. Diana Libuda, Core Member

Dr. Raghuveer Parthasarathy, Institutional Representative

University of Oregon

Spring 2026

© 2026 Sophia Doerr

This work is openly licensed via CC BY 4.0.



DISSERTATION ABSTRACT

Sophia Doerr

Doctor of Philosophy in Biology

Spatially Controlled Reconstitution of PIP Lipid Synthesis and Small GTPase Activation on Supported Membranes

Two classes of molecules that are ubiquitously important for signal transduction at the plasma membrane of eukaryotic cells are phosphatidylinositol phosphate (PIP) lipids and small GTPases. Since the misregulation of these molecules has severe consequences for cellular function, the activities of lipid modifying enzymes and GTPase regulators are subject to tight spatial and temporal control mediated by numerous interconnected pathways and feedback circuits. In this work, we develop and apply in vitro reconstitution approaches to systematically dissect the biochemical mechanisms that modulate the localization, activity, and communication of membrane-associated signaling molecules. In Chapter Two, we reconstitute the membrane recruitment and activity of the lipid kinases PI4KIIIα and PI3Kγ, which generate PI(4)P and PI(3,4,5)P_3 (PIP_3) lipids, respectively. Like other members of the mammalian PI3K superfamily, these enzymes are regulated through complexing with adaptor proteins, membrane recruitment by lipidated signaling molecules, and phosphorylation by protein kinases. We show that PI4KIIIα membrane localization is inhibited by a nanobody targeted to the interface of the TTC7 adaptor protein and the membrane-bound EFR3 protein. We also find that PI4KIIIα catalytic activity is attenuated by phosphorylation of a previously uncharacterized tyrosine

residue in the PI4KIIIα kinase domain. We then demonstrate that the PI3Kγ enzyme complex can be recruited and activated by the GβGγ complex, an interaction primarily mediated by the PI3Kγ p101 regulatory subunit. However, when GβGγ-dependent PI3Kγ activity is opposed by lipid phosphatase activity, activation of Ras GTPase is sufficient to trigger rapid PIP_3 production by PI3Kγ. In Chapter Three, we establish an in vitro platform for spatiotemporally controlling the activation of membrane-conjugated Ras GTPase using light inputs and the purified components of the iLID (improved Light-Inducible Dimer) system. This approach has been used extensively to study cell signaling in vivo and we demonstrate its utility for biochemical reconstitution assays. In Chapter Four, we couple light-inducible Ras activation to PI3Kγ-dependent PIP_3 synthesis and examine how the dynamics of this reconstituted signaling pathway are shaped by positive feedback circuits and global inhibition. This work reveals the importance of activation thresholds and membrane diffusion in determining how self-propagating reactions evolve in time and space. Together, these studies establish a versatile experimental framework for interrogating relationships between membrane-associated signaling molecules and provide insight into the networks of biochemical reactions that govern intracellular signal propagation and coordinate cellular behaviors.

*This dissertation includes previously published and unpublished co-authored material.

CURRICULUM VITAE

Sophia Doerr

GRADUATE AND UNDERGRADUATE SCHOOLS ATTENDED

University of Oregon, Eugene, OR

Amherst College, Amherst, MA

DEGREES AWARDED

Doctor of Philosophy, Biology, 2026, University of Oregon

Bachelor of Arts with Honors, Biochemistry & Biophysics, 2019, Amherst College

PROFESSIONAL EXPERIENCE

Graduate Researcher, University of Oregon,
Sep 2021 – Jun 2026

Cell Biology Teaching Assistant, University of Oregon,
Mar 2026 – Jun 2026
Introductory Biochemistry Teaching Assistant, University of Oregon,
Sep 2025 – Dec 2025
Cellular Biochemistry Teaching Assistant, University of Oregon,
Mar 2025 – Jun 2025,
Mar 2024 – Jun 2024
Marine Science Teaching Assistant, University of Oregon,
Mar 2022 – May 2022
Developmental Biology Teaching Assistant, University of Oregon,
Dec 2021 – Mar 2022
Introductory Cell Biology Teaching Assistant, University of Oregon,
Sep 2021 – Dec 2021

Research Associate, LinkedUp Bioscience, Wakefield, MA
Jul 2019 – Jun 2021

Student Researcher, Amherst College,
Jun 2018 – May 2019

Biochemistry Teaching Assistant, Amherst College,

Jan 2019 – May 2019
Developmental Biology Teaching Assistant, Amherst College,
Sep 2018 – Dec 2018
Organic Chemistry Teaching Assistant, Amherst College,
Jan 2018 – May 2018
General Chemistry Teaching Assistant, Amherst College,
Jan 2017 – May 2017

Student Researcher, University of Canterbury, Christchurch, New Zealand
Jun 2017 – Nov 2017

GRANTS, AWARDS, AND HONORS

John Woodruff Simpson Fellowship for the Study of Biology, 2022 – 2024

Graduate Student Teaching Award, 2022

Lloyd I. Rosenblum Memorial Fellowship for the Study of Biology, 2021 – 2022

Gregory S. Call Research Fellowship, 2018

PUBLICATIONS

Doerr, S., Olavarrieta-Colasurdo, A. & Hansen, S. D. Reconstitution of Ras-PI3Kγ membrane communication and feedback using light-induced signaling inputs. *Accepted at Nature Communications* (2026).

Amaris, A., Waddell, G. L., Noteboom, A. J., **Doerr, S.**, Drew, E. E., Collins, S. E. & Hansen, S. D. SHIP1 partitions between cortical oscillations and membrane puncta to regulate neutrophil chemotaxis. *BioRxiv* (2026).

Shaw, A. L., **Doerr, S.**, Nyvall, H. G., Jenkins, M. L., Suresh, S., Yip, C., Hansen, S. D. & Burke, J. E. Phosphorylation of the C-terminus of PI4KA inhibits lipid kinase activity. *BioRxiv* (2026).

Suresh, S., Shaw, A. L., Akintola, D. K., Lunke, M., **Doerr, S.**, Rohilla, P., Balla, T., Yip, C. K., Hansen, S. D., Cobb, J. A. & Burke, J. E. Development of an inhibitory TTC7B selective nanobody that blocks EFR3 recruitment of PI4KA. *Journal of Biological Chemistry* **301**, 110886 (2025).

Atajanova, T., Kang, E. M., Postnikova, A., Price, A. L., **Doerr, S.**, Du, M., Ugenti, A. & Ragkousi K. Lateral cell polarization drives organization of epithelia in sea anemone embryos and embryonic cell aggregates. *Proc. Natl. Acad. Sci. U.S.A.* **121**, e2408763121 (2024).

Doerr, S., Zhou, P. & Ragkousi, K. Origin and development of primary animal epithelia. *BioEssays* **46**, 2300150 (2023).

Doerr, S. & Ragkousi, K. Cell polarity oscillations in mitotic epithelia. *Current Opinion in Genetics & Development* **57**, 47–53 (2019).

ACKNOWLEDGMENTS

First and foremost, thank you to my advisor Dr. Scott Hansen. From day one of Cellular Biochemistry, I could tell that your uniquely creative and interdisciplinary approach to biology was going to become my absolute favorite approach to biology. Thank you for entrusting these tricky and incredibly fun reconstitutions to someone without a biochemistry research background and for enthusiastically supporting me along the way.

Thank you to my exceptional committee for all your encouragement over the years. Thank you Dr. Melanie Spero for chairing my committee and for modeling science communication at the highest level. Thank you Dr. Diana Libuda for welcoming me to UO and the IMB, for teaching me genetics, and for making me a better presenter. Thank you Dr. Mike Harms for consistently making concepts I never thought I could grasp (metabolic flux equations, complicated statistical tests, molecular dynamics simulations, and others) accessible to me. Thank you Dr. Raghu Parthasarathy for lending a physics perspective to my projects and for teaching me how to analyze imaging data. Despite several years of microscopy experience, the first time I truly understood what an image was and how we extract information from it was during your class.

Thank you to the members of the Hansen Lab, past and present. Thank you Dr. Grace Waddell, Dr. Benjamin Duewell, and Dr. Naomi Wilson for your patience and mentorship. Thank you Noah Smith, Cedric Stahel, Sarah Peabody, Katie Faris, Ethan Busi, Reed Talus, and Strata Kim. Thank you Andrés Olavarrieta-Colasurdo for all your help when I still didn't quite understand what I was doing. Thank you especially to the

current iteration of the lab: Emma Drew, Sam Fernandez-Ortiz, Thea Amaris, Mary Ruth Shifflet, Asa Noteboom, Zadie Niedergang, and Jake Weiner. Your fun and collaborative energy (and all the excellent food you bring in) is why I look forward to coming to campus every day.

An extra thank you to Emma Drew for walking me through every form I ever filled out in grad school, using gluten free flour in all your baking, and always being eager to chat. You joining the Hansen Lab was almost certainly the best thing to happen to me at UO. Of course, a thank you to Emma would be incomplete without a thank you to the wonderful Luci Camorani and Maggie and Sully.

Thank you to all the other fantastic people I have had the privilege of getting to know at UO. Thank you Rob Porch and Nicole Sagui for helping me start grad school on such a positive note and encouraging my espresso habit. It's been fun to watch you undergo parallel, yet somehow remarkably different, PhD experiences in microbial ecology and electrochemistry. Thank you Stu Johnson. I will never forget the magical day we dumped out the liquid nitrogen dewar in the loading dock. Thank you Dr. Sofia Rebecka Carlson and Dr. Sophia Rebecca Phillipps (referred to as Carl and Phil). I am extremely grateful for your friendship and mentorship. Best of luck to everyone in the IMB community as you navigate a future devoid of Sophfias.

Thank you to everyone who supported me from afar. Thank you to my mom, Birgit Doerr, my dad, Thomas Doerr, and my sister, Charissa Doerr. Thank you to Dr. Claire Lay, Kyra Wortley, Ellie Scholtz, Caitlyn Lee, Dr. Claire Rostov, and Dr. Katie Rosenberg.

Thank you to Anthony Dario. Your burgers, chicken curries, and crème brûlées (in addition to your endless kindness and willingness to indulge my scientific fixations) have fueled this journey.

Finally, thank you to my carnivoran muses. Together, Heidi, an overflowing source of positive feedback, and Ami, a reliable source of negative feedback, maintain balance in my life.

This work was funded by Dr. Scott Hansen's NSF CAREER award (MCB-2048060).

DEDICATION

This dissertation is dedicated to all the organisms who showed me kindness during this journey. May your signaling molecules remain properly regulated.

TABLE OF CONTENTS

Chapter Page

DISSERTATION ABSTRACT **3**
CURRICULUM VITAE **5**
ACKNOWLEDGMENTS **8**
DEDICATION **11**
TABLE OF CONTENTS **12**
LIST OF FIGURES **16**
CHAPTER ONE: DISSERTATION INTRODUCTION **18**
Regulation of PIP lipid interconversion at the plasma membrane 18
The role of Ras GTPase at the plasma membrane 20
Reconstitution of membrane signaling reactions on Supported Lipid Bilayers (SLBs) 21
CHAPTER TWO: REGULATION OF MEMBRANE RECRUITMENT AND ACTIVATION OF LIPID KINASES PI4KIIIα AND PI3Kγ **25**
INTRODUCTION 25
RESULTS 33
Nanobody targeted to TTC7-EFR3A interface inhibits membrane recruitment of PI4KIIIα 33
Phosphorylation of Y2090 attenuates PI4KIIIα activity without disrupting EFR3A-mediated membrane recruitment 37
GβGγ-dependent PI3Kγ membrane recruitment and activation is enhanced in the presence of active Ras GTPase 43

Ras activation allows PI3Kγ activity to overcome PTEN opposition 46

DISCUSSION 47

METHODS 53

Protein expression, purification, and labeling 53

Supported lipid bilayer experiments 65

Single particle tracking and analysis 69

BRIDGE TO CHAPTER THREE 70

CHAPTER THREE: RECONSTITUTION OF SPATIOTEMPORALLY CONTROLLED RAS ACTIVATION USING LIGHT-INDUCED HETERODIMERIZATION 72

INTRODUCTION 72

RESULTS 74

A 488 nm light pulse results in transient iLID-SspB heterodimerization on supported lipid bilayers 74

SspB membrane recruitment can be spatially controlled 76

SspB membrane recruitment can be tuned by varying the intensity of activating light 78

Membrane-tethered Ras can be locally and transiently activated with light 81

DISCUSSION 84

METHODS 85

Protein expression, purification, and labeling 85

Supported lipid bilayer experiments 91

Data analysis 95

BRIDGE TO CHAPTER FOUR 95

CHAPTER FOUR: POSITIVE FEEDBACK DRIVES THE SPATIOTEMPORAL AMPLIFICATION OF RAS ACTIVATION AND PIP_3 GENERATION IN VITRO 97

INTRODUCTION 97

RESULTS 99

A chimeric GEF mediates a positive feedback loop 99

Light-inducible Ras feedback circuit requires a threshold density of activated Ras molecules to exhibit amplification 101

Positive feedback drives Ras(GTP) spatial amplification as a Fisher-KPP wave 102

Diffusion modulates spatial coupling between Ras activation and PIP_3 synthesis 106

DISCUSSION 111

METHODS 115

Protein expression, purification, and labeling 115

Supported lipid bilayer experiments 117

Fisher-KPP wave simulations 121

Data analysis 123

BRIDGE TO CHAPTER FIVE..... 125

CHAPTER FIVE: CONCLUDING REMARKS..... 126

APPENDIX: SUPPLEMENTARY INFORMATION PERTAINING TO CHAPTERS THREE AND FOUR..... 130

REFERENCES 136

LIST OF FIGURES

Figure Page

Figure 1.1 PIP lipid and Ras GTPase signaling reactions at the plasma membrane ... 20

Figure 1.2 Reconstitution of membrane signaling reactions on SLBs 22

Figure 2.1 Nanobody targeted to TTC7-EFR3A interface inhibits membrane recruitment of PI4KIIIα 36

Figure 2.2 Phosphorylation of Y2090 attenuates PI4KIIIα activity without disrupting EFR3A-mediated membrane recruitment 41

Figure 2.3 GβGγ-dependent PI3Kγ membrane recruitment and activation is enhanced in the presence of active Ras GTPase 45

Figure 2.4 Ras activation allows PI3Kγ activity to overcome PTEN 46

Figure 3.1 A 488 nm light pulse results in transient iLID-SspB heterodimerization on supported lipid bilayers 75

Figure 3.2 SspB membrane recruitment can be spatially controlled 77

Figure 3.3 SspB membrane recruitment can be tuned by varying the intensity of activating light 79

Figure 3.4 GEF-SspB membrane recruitment can be tuned by varying the intensity of activating light 80

Figure 3.5 Membrane-tethered Ras can be locally and transiently activated with light 82

Figure 4.1 A chimeric GEF mediates a positive feedback loop 100

Figure 4.2 Light-inducible Ras feedback circuit requires threshold density of activated Ras molecules to exhibit amplification 102

Figure 4.3 Positive feedback drives Ras(GTP) spatial amplification as a Fisher-KPP wave 104

Figure 4.4 Diffusion modulates spatial coupling between Ras activation and PIP_3 synthesis 108

Supplementary Figure 1 SspB membrane recruitment as a function of pattern size 130

Supplementary Figure 2 Calibration of LED power for iLID activation 131

Supplementary Figure 3 Repetitive low light-induced membrane recruitment of GEF-SspB does not trigger Ras(GTP) amplification 131

Supplementary Figure 4 Fisher-KPP waves simulated in the absence of logistic growth and GAP-mediated decay 132

Supplementary Figure 5 Fisher-KPP waves simulated over a range of diffusion coefficients 133

Supplementary Figure 6 Membrane-anchored GβGγ reduces the rate of Ras(GTP) wave expansion 134

Supplementary Figure 7 Lipid diffusion coefficient measured by single particle tracking 135

CHAPTER ONE

DISSERTATION INTRODUCTION

Regulation of PIP lipid interconversion at the plasma membrane

Biochemical reactions involving phosphoinositide lipids govern growth, division, differentiation, metabolism, cytoskeletal dynamics, membrane trafficking, and death across cell types[1–3]. These lipids are produced via modifications to phosphatidylinositol (PI), which consists of two acyl chains, a glycerol backbone, and an inositol headgroup. Differential phosphorylation of hydroxyls at the 3, 4, and 5 positions of the inositol headgroup results in seven mono-, bis-, and tris-phosphorylated species of phosphoinositide phosphate (PIP) lipids that define the identities of intracellular membranes and engage with diverse, spatially restricted signaling pathways[3]. Three PIP lipid species present in the inner leaflet of the plasma membrane are PI 4-phosphate (PI(4)P), PI (4,5)-bisphosphate (PIP_2), and PI (3,4,5)-trisphosphate (PIP_3) (**Fig. 1.1**)[3].

PI(4)P is generated from PI at the plasma membrane by the PI4KIIIα (type III PI 4-kinase alpha) complex. PI4KIIIα activity has been implicated in the progression of a number of human diseases including hepatitis C viral infection[4,5] and pancreatic cancer[6,7] yet its molecular regulation remains poorly understood. PI4KIIIα belongs to the PI3K superfamily of kinases, all of which rely on lipidated proteins to localize to membrane surfaces in proximity to their lipid substrates[2]. In Chapter Two, we discuss how the spatial localization of the PI4KIIIα complex is controlled by the palmitoylated protein EFR3. We also investigate phosphorylation of PI4KIIIα as a potential mechanism for regulating

PI(4)P production. Plasma membrane PI(4)P is exchanged for phosphatidylserine (PS) from the endoplasmic reticulum[8] and converted to PIP_2 by PIP5K (PI 4-phosphate 5-kinase). Constitutively present in the cytoplasmic surface of the plasma membrane, PIP_2 interacts with a wide range of signaling molecules to direct processes including vesicular transport and cytoskeletal reorganization[9,10].

Cell surface receptor activation triggers the phosphorylation of PIP_2 to generate PIP_3 via the plasma membrane recruitment of Class I PI3K enzymes (**Fig. 1.1**). Although they catalyze a different reaction, these kinases also belong to the PI3K superfamily and share structural and regulatory features with PI4KIIIα. PIP_3 is a second messenger that is produced extremely rapidly in spatially defined regions of the plasma membrane due to positive feedback circuits[11–15]. PIP_3 synthesis is at the core of many dramatic cellular restructuring events such as polarized migration and asymmetric division and misregulation of PI3K signaling is a frequent driver of human cancers and immune diseases[3,16]. In Chapter Two, we explore how the activity of the immune-cell specific PI3Kγ (PI 3-kinase gamma) isoform is regulated downstream of activated receptors by interactions with membrane-anchored GβGγ subunits and the active form of Ras GTPase. We interrogate the distinct functions served by the p110γ catalytic subunit and the p101 regulatory subunit of the PI3Kγ complex in responding to GβGγ and Ras. We then examine how PI3Kγ integrates these two signaling inputs to overcome antagonism by PTEN (Phosphatase and Tensin Homolog) lipid phosphatase, a well-documented tumor suppressor[17].

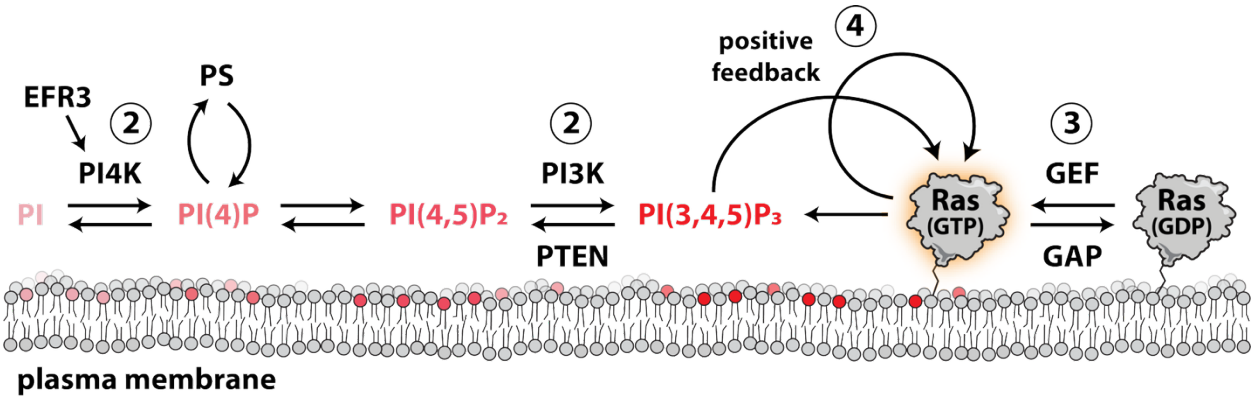

Figure 1.1 PIP lipid and Ras GTPase signaling reactions at the plasma membrane
Chapter 2 of this dissertation focuses on the regulation of PI4KIIIα and PI3Kγ, which phosphorylate PI and PIP_2 lipids to generate PI(4)P and PIP_3 lipids, respectively. PI4KIIIα is recruited to the plasma membrane by EFR3. PI3Kγ activity is promoted by GβGγ subunits and GTP-bound Ras GTPase and is opposed by PTEN lipid phosphatase. Chapter 3 describes a technique for mimicking the asymmetric activation of Ras GTPase by GEFs downstream of cell surface receptors in vitro. Chapter 4 discusses the spatiotemporal amplification of Ras activation and PI3Kγ-dependent PIP_3 generation due to positive feedback circuitry.

The role of Ras GTPase at the plasma membrane

The Ras family of plasma membrane-associated small GTPases, which includes H-Ras, K-Ras, and N-Ras, is best known for the significant role its dysregulation plays in human cancers and developmental disorders[18]. When activated, Ras molecules initiate signaling cascades that promote cell growth, proliferation, and migration by binding a host of effector molecules including Class I PI3Ks. GTPases function as molecular switches which are active when bound to GTP (Guanosine 5′-Triphosphate) and inactive when bound to GDP (Guanosine-5′-Diphosphate). These states are promoted by GEF (Guanine Nucleotide Exchange Factor) activators and GAP (GTPase Activating Protein) inhibitors (**Fig. 1.1**)[19]. Membrane-anchored Ras molecules are activated via receptor agonist-induced recruitment of RasGEFs. In the best-characterized Ras activation pathway, intracellularly phosphorylated receptor tyrosine kinases recruit GRB2 (Growth

Factor Receptor-Bound Protein 2) which locally activates the SOS1 (Son of Sevenless Homolog 1) GEF[16]. Similarly, RasGEFs are recruited by GβGγ subunits which are activated downstream of GPCR (G Protein-Coupled Receptor) ligand binding[20]. Asymmetries in receptor activation and GEF and GAP distribution lead to spatially patterned Ras activation at the plasma membrane[19,21]. In healthy cells, mechanisms of global inhibition and negative feedback control the duration of Ras signaling events in addition to their spatial distribution[22,23]. In Chapter Three, we explore the spatial and temporal regulation of Ras signaling. To enter signaling states, cells must temporarily overcome inhibitory mechanisms. Positive feedback circuits promote the rapid plasma membrane accumulation of active Ras and the effector molecules it communicates to (**Fig. 1.1**)[13,24,25]. GEFs, which often contain multiple protein and lipid binding domains in addition to their catalytic domain, are the most logical mediators of positive feedback within GTPase signaling[26–28]. In Chapter Four, we discuss GEF recruitment-based positive feedback loops and how they drive the spatiotemporal amplification of Ras activation and downstream PI3Kγ-dependent PIP_3 generation in the presence of global inhibition.

Reconstitution of membrane signaling reactions on Supported Lipid Bilayers (SLBs)

PIP lipid and small GTPase signaling reactions occur within enormously complex cellular signal transduction networks abundant in compensatory pathways and interconnected regulatory circuits[15,24,29]. In many cases, interrogating the relationships

between specific molecules or the dynamics of individual signaling reactions is unrealistic in the native cellular context due to confounding variables. For detailed molecular insight, we must turn to in vitro reconstitutions composed of purified molecular components. Biochemical studies of PIP lipid modifying enzymes and small GTPases have historically relied on solution-based measurements that fail to capture the spatial organization and membrane association dynamics of these proteins. However, recent advances in fluorescence microscopy and Supported Lipid Bilayer (SLB) technology have enabled researchers to directly visualize the membrane binding and activity of peripheral membrane proteins with single molecule resolution[30–32]. In this dissertation, we reconstitute molecular interactions and biochemical reactions on SLBs and observe their spatiotemporal evolution using TIRF-M (Total Internal Reflection Fluorescence Microscopy) (**Fig. 1.2**). This imaging technique allows for the visualization of fluorescently labeled signaling molecules and biosensors on membranes with a high signal-to-noise ratio.

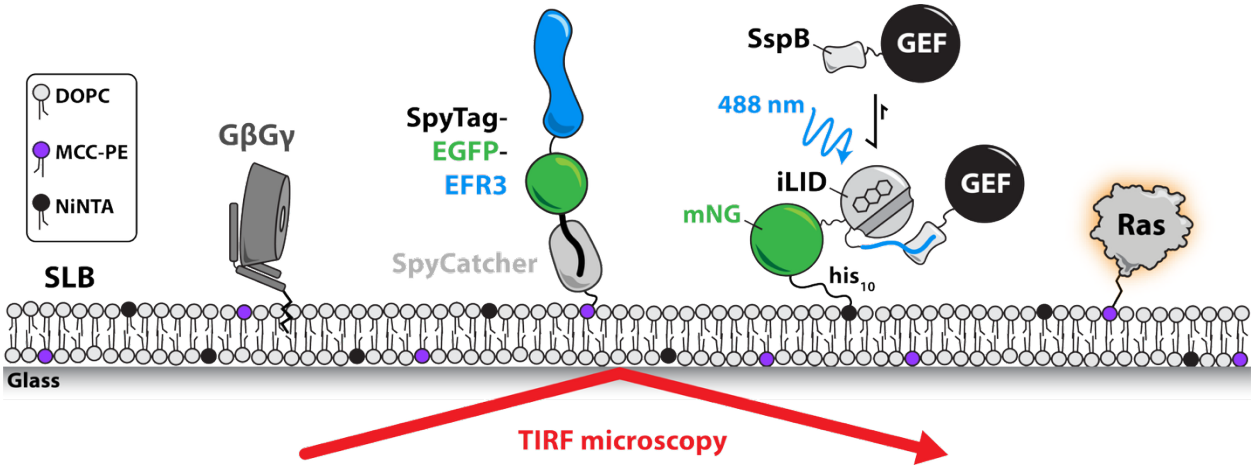

Figure 1.2 Reconstitution of membrane signaling reactions on SLBs

The experiments presented in this dissertation relied on reconstituting signaling reactions on supported membranes and visualizing their spatiotemporal evolution by TIRF microscopy. We anchor GβGγ subunits to bilayers via a native farnesyl group. Ras and SpyCatcher molecules are conjugated to MCC-PE lipids. We covalently attach SpyTag-EGFP-EFR3 to membrane-bound SpyCatcher. We tether his_{10}-mNeonGreen-iLID to NiNTA lipids. Upon illumination with blue light, iLID recruits SspB-GEF to the bilayer, thereby activating Ras.

Membrane recruitment is the most important mechanism by which cortical proteins are regulated and is therefore a key consideration for reconstituting lipid kinase and small GTPase signaling in vitro. We employed a range of strategies for localizing purified proteins to SLBs for the experiments described in this dissertation (**Fig. 1.2**). The simplest case is the GβGγ complex, which is purified from Sf9 insect cells rather than bacteria and contains a native farnesyl group that anchors it to supported membranes. Other proteins require bilayers containing 2% cysteine-reactive maleimide lipids (i.e. MCC-PE) or 2% nickel-chelating lipids (i.e. NiNTA, Nickel Nitrilotriacetic Acid) for membrane localization. We conjugate Ras to maleimide lipids in a physiologically relevant orientation via a C-terminal cysteine[33]. A protein known as SpyCatcher, which contains an N-terminal KCK motif, is similarly conjugated to maleimide lipids. SpyCatcher forms a covalent isopeptide bond with a peptide known as SpyTag[34]. We make use of this interaction to attach a fusion of SpyTag-EGFP and the C-terminus of EFR3 to bilayers. This technique enables the reconstitution of EFR3-mediated PI4KIIIα membrane localization. We also establish a light-inducible system to transiently recruit signaling molecules to defined regions of supported bilayers. This approach relies on the light-activatable iLID (improved Light-Inducible Dimer) protein and its binding partner SspB (Stringent response protein B), which we fused to a RasGEF[35,36]. We tether his_{10}-mNeonGreen-iLID to bilayers

containing NiNTA lipids. When illuminated with blue light, iLID recruits SspB-GEF to the membrane, locally activating membrane-conjugated Ras molecules in a manner reminiscent of asymmetric inputs from cell surface receptors. Together, these innovative biochemical techniques grant us spatial control over membrane-associated signaling proteins and allow us to reconstitute and probe the molecular mechanisms that regulate Ras activation and PIP lipid synthesis at the plasma membrane.

CHAPTER TWO

REGULATION OF MEMBRANE RECRUITMENT AND ACTIVATION OF LIPID KINASES PI4KIIIα AND PI3Kγ

*This chapter contains previously published and unpublished co-authored material.

Doerr, S., Olavarrieta-Colasurdo, A. & Hansen, S. D. Reconstitution of Ras-PI3Kγ membrane communication and feedback using light-induced signaling inputs. *BioRxiv* (2026).

Shaw, A. L., **Doerr, S.**, Nyvall, H. G., Jenkins, M. L., Suresh, S., Yip, C., Hansen, S. D. & Burke, J. E. Phosphorylation of the C-terminus of PI4KA inhibits lipid kinase activity. *BioRxiv* (2026).

Suresh, S., Shaw, A. L., Akintola, D. K., Lunke, M., **Doerr, S.**, Rohilla, P., Balla, T., Yip, C. K., Hansen, S. D., Cobb, J. A. & Burke, J. E. Development of an inhibitory TTC7B selective nanobody that blocks EFR3 recruitment of PI4KA. *Journal of Biological Chemistry* **301**, 110886 (2025).

The work on PI4KIIIα was done as part of collaborative projects led by Dr. John Burke, Dr. Sushant Suresh, and Alexandria Shaw at the University of Victoria. All experiments shown were designed and performed by Dr. Scott Hansen and Sophia Doerr.

INTRODUCTION

The interconversion of phosphoinositide lipid species at the plasma membrane is a central pillar of cellular signal transduction[2]. These reactions are driven by a specialized cohort of lipid kinases and phosphatases. Among these, the Class I-III PI 3-kinases and

the Type III PI 4-kinases constitute the PI3K superfamily, a group of evolutionarily related enzymes that, despite modulating distinct physiological processes, share a conserved catalytic domain architecture. PI4KIIIα (type III PI 4-kinase alpha, also referred to as PI4KA) is an essential lipid kinase that is responsible for phosphorylating the 4 position of phosphatidylinositol (PI) to generate PI 4-phosphate (PI(4)P) at the plasma membrane[1,2,37]. This pool of PI(4)P is important for the plasma membrane enrichment of phosphatidylserine (PS) as PI(4)P provides the energy necessary for transport of PS from the endoplasmic reticulum by the ORP5/8 lipid transfer proteins[8]. PI(4)P is also the necessary precursor of PI (4,5)-bisphosphate (PIP_2) and PI (3,4,5)-trisphosphate (PIP_3) lipids, critical second messengers involved in myriad signaling pathways[1]. The conversion of PIP_2 to PIP_3 is mediated by the Class I PI3K enzymes[38]. A member of this group, PI3Kγ (PI 3-kinase gamma, also referred to as PIK3CG), is highly expressed in myeloid cells including neutrophils and macrophages where it drives key immune processes[39,40]. Importantly, unlike PI4KIIIβ and the Class II PI3Ks, PI4KIIIα and PI3Kγ form stable complexes with regulatory subunits[2]. These enzyme complexes also depend on interactions with lipidated signaling molecules to localize to the plasma membrane, an important mechanism by which their lipid kinase activity is spatially regulated in cells[3]. The experiments presented in this chapter rely on reconstituting PI4KIIIα and PI3Kγ membrane localization and activity in the presence of membrane-tethered regulators on Supported Lipid Bilayers (SLBs).

PI4KIIIα consists of multiple distinct domains. At the N-terminus is an α-solenoid commonly referred to as the horn followed by a domain that allows for the dimerization of two PI4KIIIα proteins. Like its Class I PI3K relatives, PI4KIIIα has a C-terminal bi-lobal kinase domain that is cradled by its helical domain. The predominant form of PI4KIIIα exists as a complex with its accessory proteins, TTC7 (two isoforms: TTC7A and TTC7B) and FAM126 (two isoforms: FAM126A and FAM126B) forming a ~750 kDa dimer of heterotrimers[41,42]. Both TTC7 and FAM126 contribute toward complex stability, with FAM126 not directly interacting with PI4KIIIα but instead acting as a stabilizer of TTC7[43]. An established regulator of PI4KIIIα membrane recruitment is the palmitoylated protein EFR3 (two isoforms: EFR3A and EFR3B)[44]. It anchors PI4KIIIα in proximity to its lipid substrate through contacts between its C-terminus and TTC7 and FAM126[45,46]. In this work, we exclusively examine the membrane recruitment and activity of the complex consisting of PI4KIIIα, TTC7B, and FAM126A (referred to as the PI4KIIIα complex) in the presence of EFR3A. It has been demonstrated that the TTC7B, FAM126A, and EFR3A isoforms together result in the highest affinity version of the PI4KIIIα-EFR3 complex[46]. While this particular combination of PI4KIIIα accessory protein isoforms is likely present across a range of cell types, several of its constituent isoforms are most highly expressed in neuronal tissues[2,47,48].

Dysregulation of the PI4KIIIα enzyme and its regulatory partners has been implicated in numerous human diseases[47–55]. In hepatitis C viral infection, the viral protein NS5A activates PI4KIIIα, leading to the formation of viral replication organelles enriched

in PI(4)P[4,5]. After this discovery was made, multiple well-validated, potent, and selective ATP-competitive PI4KIIIα inhibitors were developed as anti-hepatitis C viral agents[44,56]. However, enthusiasm for these molecules as therapeutics was greatly diminished as knockdown of PI4KIIIα either genetically or pharmacologically caused rapid death in mice[44]. Increased PI4KIIIα activity also plays a role in cancer, with overexpression of PI4KIIIα and EFR3A occurring in pancreatic cancers driven by K-Ras GTPase[6,7]. EFR3A has been shown to directly interact with oncogenic K-Ras[6] and elevated plasma membrane PS levels due to increased PI4KIIIα activity have been found to promote oncogenic K-Ras function and tumorigenesis[7]. The recently confirmed role of PI4KIIIα and EFR3A in cancer has renewed interest in generating pharmacological agents that limit PI4KIIIα signaling in combination with K-Ras mutant-selective inhibitors.

Due to the side effects of ATP-competitive PI4KIIIα inhibitors, there could be advantages to generating novel allosteric modulators of PI4KIIIα signaling. The development of molecules that block EFR3-dependent PI4KIIIα recruitment offers a potential avenue to design innovative therapeutics and provides opportunities to further understand how PI4KIIIα is regulated. One of the most well-validated tools for manipulating signaling proteins are nanobodies, which bind to specific effector interfaces[57,58]. Nanobodies are composed of the variable domains of heavy chain-only antibodies, which lack the light chain of conventional antibodies[59]. This single-domain architecture results in compact molecules (~15 kDa) that can be readily expressed in bacteria, making them attractive tools for therapeutic and diagnostic applications[60]. Using

a yeast surface display selection approach, BioLayer Interferometry (BLI), and Cryogenic Electron Microscopy (cryo-EM), we identified and validated a TTC7B-selective nanobody (referred to as F3IN) that blocks EFR3 binding. Here, we develop a technique to reconstitute EFR3A-dependent recruitment of the PI4KIIIα complex to SLBs and demonstrate that the F3IN nanobody strongly decreases PI4KIIIα membrane localization in a dose-dependent manner. This work represents a proof of concept that PI4KIIIα can be modulated with molecules functioning outside of its ATP-binding site and introduces a nanobody tool that can be used to dissect the roles of the PI4KIIIα accessory proteins in controlling PI4KIIIα activity.

Although progress has been made toward developing PI4KIIIα inhibitors and allosteric modulators, many of the mechanisms by which PI(4)P generation is regulated in cells remain unknown. Recent research has revealed that PI4KIIIα plasma membrane activity may be less uniform and more tightly controlled than was previously assumed[61]. Inhibition of PI4KIIIα disrupts the oscillatory behavior of PI(4)P as well as that of PIP_2 and PIP_2-dependent effectors at the plasma membrane indicating that the spatial patterning of PI4KIIIα activity plays an important role in shaping global cell signaling dynamics. It has been demonstrated that following depletion of the PIP_2 pool through PLC signaling, the CNAβ1 isoform of the calcineurin phosphatase increases PI(4)P generation by dephosphorylating the PI4KIIIα complex[62,63]. In addition, the *Drosophila* protein phosphatase Pez (PTPN14 in mammals) has been shown to increase plasma membrane PI(4)P levels although the target of this phosphatase is unknown[64]. These results suggest

that phosphorylation may play a role in the reversible regulation of PI4KIIIα activity. Although PI4KIIIα has been found to be phosphorylated in many phospho-proteomic Mass Spectrometry (MS) experiments[65], there has been no definitive exploration of the function these phosphorylation sites serve in PI4KIIIα regulation.

Using The Kinase Library[66,67] and Liquid Chromatography-Mass Spectrometry (LC-MS) analysis, we identified Y2090 in PI4KIIIα as a site that can be targeted by multiple tyrosine kinases. This residue is located in the kα12 helix within the kinase domain. The kα12 helix is part of a C-terminal regulatory motif that is conserved across the members of the PI3K superfamily[68–72]. Phosphorylation of residues in this helix have been found in members of the Class I PI3Ks, with all leading to decreased lipid kinase activity[73–75]. By reconstituting EFR3A-mediated PI4KIIIα membrane recruitment on SLBs containing the lipid substrate of PI4KIIIα, we demonstrate that phosphorylation of Y2090 suppresses lipid kinase activity without impacting PI4KIIIα membrane localization.

Like PI4KIIIα, the Class I PI3Ks are recruited to the plasma membrane where they are responsible for catalyzing the conversion of PIP_2 to PIP_3 downstream of cell surface receptor activation[38]. The PI3Kγ isoform is unique among PI3Ks as it is most highly expressed in cells of hematopoetic origin although it is present to a lesser extent across a range of tissue types[40]. PI3Kγ is known to serve critical functions in regulating the adhesion, chemotaxis, Reactive Oxygen Species (ROS) generation, and NETosis of granulocytes and the phagocytosis and cytokine production of dendritic cells and macrophages[39]. This enzyme is activated at the plasma membrane downstream of

GPCRs (G Protein-Coupled Receptors) and RTKs (Receptor Tyrosine Kinases) by direct interactions with membrane-anchored GβGγ subunits and the GTP-bound active form of Ras GTPase[58,76–78].

Since PI3Kγ activity is broadly important for immune cell function, it is unsurprising that defects in the regulation of this enzyme have been linked to numerous inflammatory diseases and cancers[3,39,79]. PI3Kγ plays key roles in the progression of hematogenous cancers and has therefore been identified as a promising therapeutic target in the treatment of leukemias and lymphomas[39]. Unfortunately, since PI3Kγ signaling is a central node that integrates inputs from different classes of cell surface receptors and connects to myriad signaling pathways and feedback circuits across cell types, it is difficult to predict the outcomes and side effects of PI3Kγ inhibitory drugs[79]. PI3Kγ loss-of-function mutations have been reported in patients suffering from immunodeficiencies[80,81]. Interrogating the molecular regulation of PI3Kγ has far-reaching implications for our understanding of cell signaling and disease.

In cells, PI3Kγ exists as a heterodimer of a catalytic subunit, p110γ, and one of two regulatory subunits, p101 or p84. Here, we focus on the regulation of the complex formed between p110γ and p101 and the p110γ catalytic subunit alone. Although p110γ contains a GβGγ binding site, robust binding between PI3Kγ and GβGγ is mediated by the p101 regulatory subunit and neutrophils lacking p101 exhibit defects in PIP_3 generation, ROS production, and directional migration downstream of GPCR activation[77,82]. By contrast, molecules of Ras(GTP), which are activated early in numerous

signaling cascades, bind exclusively to the p110γ catalytic subunit of PI3Kγ, thereby recruiting the kinase to the plasma membrane in proximity to PIP_2 lipids[76]. Asymmetric Ras activation is an important mechanism by which PI3Kγ activity is spatially regulated in cells.

Parallels are commonly drawn between mammalian PI3Kγ and the Class I PI3Ks of the *Dictyostelium* amoeba[14,83]. The *Dictyostelium* PI3Ks are also activated by the GβGγ complex and active Ras, but do not rely on regulatory subunits like p101[14]. Unlike those of other mammalian Class I PI3Ks, the p110γ catalytic subunit is uniquely stable and undergoes autoinhibition mediated by its C-terminal regulatory motif in the absence of a regulatory subunit[84]. Mammalian p110γ may therefore be analogous to a more ancestral form of the enzyme. *Dictyostelium* cells that lack functional Gβ subunits cannot chemotax effectively. However, these cells retain their ability to polarize, divide, and randomly migrate due to a positive feedback circuit formed between Ras activation and PI3K-mediated PIP_3 generation[14]. Here, by measuring PIP_3 generation on SLBs, we demonstrate that free p110γ is robustly activated by Ras(GTP) in the absence of GβGγ whereas the full PI3Kγ complex (p110γ-p101) requires GβGγ for activation. Importantly, Ras activation strongly enhances the activity of the PI3Kγ complex in the presence of GβGγ. These results point to an evolutionary role of p101 in modulating the sensitivity of the enzyme to diverse signaling inputs. Across eukaryotic cells, the tumor suppressor PTEN (Phosphatase and Tensin Homolog), limits spurious PI3K signaling by converting PIP_3 back to PIP_2[17,39,85,86]. We reconstitute PI3Kγ (p110γ-p101 and p110γ) activity in the

presence of PTEN and show that Ras activation functions as a switch that allows PI3Kγ activity to outcompete the reverse reaction.

RESULTS

Nanobody targeted to TTC7-EFR3A interface inhibits membrane recruitment of PI4KIIIα

To target the EFR3-mediated membrane recruitment of the PI4KIIIα complex, we screened a synthetic yeast surface display library of >5×10^8 nanobodies[87] to isolate a nanobody that specifically blocked EFR3A binding to the TTC7B-FAM126A complex[46]. Initially, we used the TTC7B-FAM126A heterodimer as our antigen and performed multiple rounds of cell sorting to obtain a library of candidate nanobodies. To then enrich for nanobodies targeting the EFR3 binding site on TTC7B-FAM126A, we used a complex of TTC7B and a chimeric construct comprising FAM126A fused to the C-terminus of EFR3A to counter-select against our original library. Ultimately, we isolated a highly specific nanobody that we refer to as F3IN. Using BLI, we confirmed that F3IN binds TTC7B-FAM126A with high affinity (KD = 2.9 ± 0.83 nM)[46]. We also found that the F3IN nanobody bound with ~100-fold increased affinity to the full PI4KIIIα-TTC7B-FAM126A complex (KD = 0.030 ± 0.019 nM). We then performed a competition BLI assay to investigate whether F3IN is a competitive inhibitor of EFR3 for the TTC7B binding site[46]. F3IN was loaded onto the biosensor and dipped into a solution containing the PI4KIIIα complex in the presence of increasing concentrations of EFR3A (15–240 nM). We observed a decrease in F3IN-PI4KIIIα binding as the concentration of EFR3A increased.

These results indicate that the F3IN nanobody competes with EFR3A for binding to TTC7B and suggest that it may function as a specific inhibitor of PI4KIIIα membrane localization.

To identify the binding interface of F3IN with the PI4KIIIα complex, we used cryo-EM to generate a three-dimensional reconstruction of the PI4KIIIα-TTC7B-FAM126A-F3IN complex, which allowed for unambiguous determination of the residues mediating the interaction between F3IN and the PI4KIIIα complex[46]. The TTC7B-F3IN interface comprises 415 $Å^2$ of buried surface area. The structure revealed an extended beta strand within CDR3 (Complementarity Determining Region 3) of F3IN that interacts with three TTC7B α helices and orients the nanobody into the cavity normally occupied by the α3 helix of EFR3A, suggesting a mechanism by which F3IN might sterically hinder EFR3A binding. Intriguingly, F3IN also interacts with the PI4KIIIα enzyme, resulting in 280 $Å^2$ of buried surface area. This interface, which is mediated by the N-terminus of F3IN and the N-terminal horn of PI4KIIIα, explains the increased affinity of F3IN for the full PI4KIIIα complex.

To examine if the F3IN nanobody is indeed sufficient to block EFR3A-mediated membrane recruitment of PI4KIIIα, we performed single-molecule TIRF-M (Total Internal Reflection Fluorescence Microscopy) experiments on SLBs. To tether the C-terminal PI4KIIIα binding region of EFR3A to SLBs in an orientation where it was free to interact with PI4KIIIα complexes in solution, we made use of the SpyCatcher-SpyTag system (**Fig. 2.1a**)[88]. We covalently attached SpyCatcher harboring a single N-terminal cysteine

(i.e. thiol) to lipid bilayers containing cysteine-reactive maleimide lipids (i.e. MCC-PE). We then introduced a construct comprising an N-terminal SpyTag-EGFP fused to residues 721 to 791 of EFR3A (referred to as SpyTag-EGFP-EFR3A). We visualized the membrane recruitment of the AF647-labeled PI4KIIIα-TTC7B-FAM126A complex (AF647-PI4KIIIα) in the absence and presence of EFR3A using membrane-tethered EGFP-SpyTag as a negative control (**Fig. 2.1b**). AF647-PI4KIIIα was only robustly recruited to the membrane when EFR3A was present. We then sought to determine if the F3IN nanobody was sufficient to disrupt the EFR3A-PI4KIIIα interaction on SLBs. In the presence of only 2 nM F3IN, we observed a dramatic reduction in the single-molecule membrane binding frequency (**Fig. 2.1b, c**) and bulk membrane recruitment (**Fig. 2.1d**) of AF647-PI4KIIIα on SLBs containing membrane-tethered EFR3A. We also demonstrated that EFR3A-mediated PI4KIIIα membrane binding could be modulated in a dose-dependent manner (**Fig. 2.1e**).

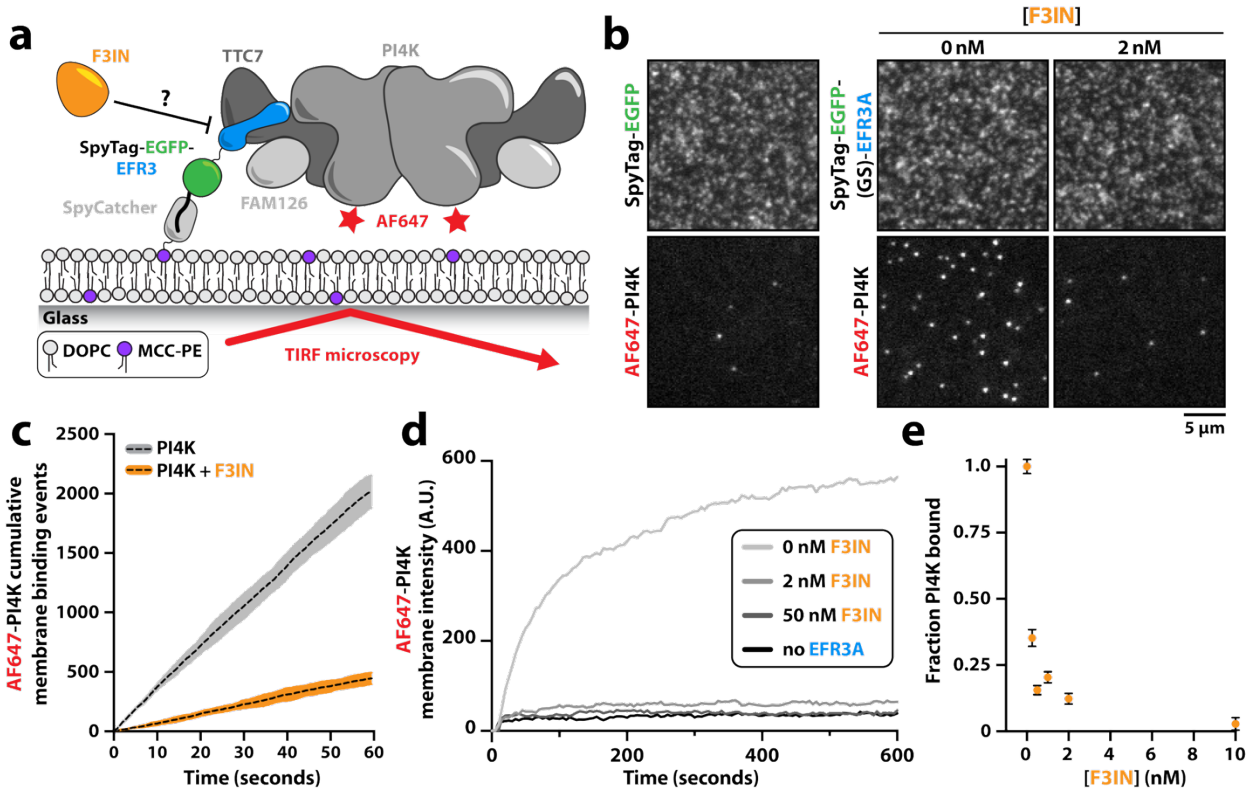

Figure 2.1 Nanobody targeted to TTC7-EFR3A interface inhibits membrane recruitment of PI4KIIIα

(a) Cartoon schematic showing the experimental design for measuring the localization of the AF647-PI4KIIIα complex on an SLB containing tethered SpyTag-EGFP-EFR3A. SpyCatcher is covalently linked to a maleimide lipid (i.e. MCC-PE) and SpyTag-EGFP-EFR3A is conjugated to SpyCatcher via an isopeptide bond. Membrane localization of SpyTag-EGFP-EFR3A and AF647-PI4KIIIα are visualized using TIRF-M. **(b)** Representative TIRF-M images showing the localization of membrane-tethered SpyTag-EGFP-EFR3A and EGFP-SpyTag (top row). Representative images showing the localization of 1 nM AF647-PI4KIIIα in the absence and presence of 2 nM F3IN nanobody (bottom row). **(c)** The single-molecule membrane binding frequency of 1 nM AF647-PI4KIIIα is reduced in the presence of 2 nM F3IN. Total number of membrane binding events was measured on a 3000 µm^2 membrane surface area by single-molecule TIRF-M. Dashed black lines represent means and shaded regions represent standard deviations (n = 3 technical replicates). **(d)** Kinetic traces showing the bulk membrane absorption and equilibration of 1 nM AF647-PI4KIIIα on SpyTag-EGFP-EFR3A or EGFP-SpyTag (i.e. no EFR3A) membranes in the absence and presence of F3IN nanobody. **(e)** F3IN nanobody reduces membrane localization of 1 nM AF647-PI4KIIIα in a dose-dependent manner. Plot shows the normalized AF647-PI4KIIIα membrane fluorescence as a function of F3IN concentration. Error bars represent standard deviation (n = 3 technical replicates). **(b-e)** Membrane composition: 94% DOPC, 2% MCC-PE (SpyCatcher bound), and 4% PI lipids.

Phosphorylation of Y2090 attenuates PI4KIIIα activity without disrupting EFR3A-mediated membrane recruitment

Evidence that protein phosphatases promote the production of PI(4)P at the plasma membrane[62,64] motivated us to investigate phosphorylation as a potential PI4KIIIα regulatory mechanism[89]. One kinase that is known to interact with PI4KIIIα is LCK (Lymphocyte-Specific Protein Tyrosine Kinase), a member of the SRC-family of kinases[90,91]. To determine if PI4KIIIα can be directly phosphorylated by LCK, we purified an active LCK construct and co-incubated varying concentrations of this kinase with the PI4KIIIα-TTC7B-FAM126A complex. The resulting samples were then analyzed using Liquid Chromatography-Mass Spectrometry (LC-MS)[89]. We identified two phosphorylation sites, both on the PI4KIIIα enzyme, that were unique to the LCK-treated samples. One of these sites, Y1154, a residue that is weakly conserved across PI4KIIIα sequences, was only ~50% phosphorylated. We ultimately determined that pY1154 did not impact the stability or activity of the PI4KIIIα complex[42]. By contrast, the other phosphorylation site, Y2090, which is located in the kα12 helix of the kinase domain regulatory motif, was ~90% phosphorylated in the LCK-treated sample. Intriguingly, although this phosphorylation site is rarely annotated in phospho-proteomics datasets, Y2090 is highly conserved across eukaryotes.

To further understand the specificity of Y2090 phosphorylation by tyrosine kinases, we utilized the site-specific kinase prediction tool from The Kinase Library to identify kinases with the highest specificity for the Y2090 site[66,67]. Y2090 was predicted to be

targeted by a distinct set of kinases with DDR1, DDR2, and ALK (Anaplastic Lymphoma Kinase) among the highest-ranked. DDR1 and 2 are non-integrin collagen receptors essential for developmental processes[92,93], while ALK is an oncogenic receptor tyrosine kinase expressed in the nervous system[94]. Notably, SRC-family members were ranked much lower (LCK and SRC were ranked 36th and 47th, respectively, out of 78). Interestingly, INSR (Insulin Receptor), which is a major activator of the PI3K-AKT signaling cascade, was ranked 9th. To experimentally assess kinase specificity toward PI4KIIIα, we treated the complex with a fixed amount (1 µg) of LCK, SRC, or INSR and quantified phosphorylation at Y2090 by LC-MS. While LCK phosphorylated Y2090 to ~90%, INSR kinase phosphorylated Y2090 to ~30%, and SRC phosphorylated Y2090 to ~40%[89]. A substantial cohort of tyrosine kinases are likely capable of phosphorylating PI4KIIIα at Y2090.

To structurally compare untreated PI4KIIIα to PI4KIIIα^{pY2090}, we used HDX-MS (Hydrogen-Deuterium Exchange Mass Spectrometry) and found only one significant difference in deuterium exchange which occurred in residues 2083-2092 of the kα12 helix upon Y2090 phosphorylation. No large conformational changes distant from the direct phosphorylation site were detected. We then performed an initial assessment to determine whether LCK-mediated PI4KIIIα phosphorylation alters its lipid kinase activity by measuring ATP turnover using 100% PI vesicles as substrate. In this experiment, PI4KIIIα^{pY2090} exhibited a ~10-fold decrease in activity compared to the unphosphorylated enzyme[89]. Since we never generated a 100% phosphorylated version of PI4KIIIα, this

observed decrease in activity may be an underestimation of the true effect of phosphorylation. Notably, we found that the intrinsic ability of PI4KIIIα to turn over ATP in the absence of lipid substrate was unaffected by Y2090 phosphorylation, suggesting that phosphorylation does not decrease the ATPase activity of PI4KIIIα and instead likely alters either lipid engagement or catalysis[89].

Although we obtained intriguing results by measuring ATP turnover in the presence of PI vesicles, this experimental system is not a good biological mimic of cellular PI4KIIIα activity since EFR3 is required for robust recruitment of PI4KIIIα to the plasma membrane[44]. We reasoned that the phosphorylation-dependent inhibition observed in the absence of EFR3 could be due to altered membrane binding of the complex, which might have a negligible effect under EFR3 recruitment. We therefore sought to measure PI4KIIIα recruitment and kinase activity on SLBs with lipid compositions that more closely resembled that of the plasma membrane in the presence of membrane-tethered EFR3. For these experiments, we covalently tethered the EGFP-labeled C-terminus of EFR3A to SLBs using the SpyCatcher-SpyTag system, as before (**Fig. 2.2a**). We then visualized the dynamic membrane localization and activity of a single batch of AF647-labeled PI4KIIIα-TTC7B-FAM126A which was divided into an unphosphorylated sample and an LCK-treated sample in which Y2090 was ~90% phosphorylated (AF647-PI4KIIIα and AF647-PI4KIIIα^{pY2090}, respectively). We found that EFR3A-mediated bulk membrane recruitment of AF647-PI4KIIIα was not greatly perturbed by phosphorylation of Y2090 (**Fig. 2.2b, c**). Single-molecule cumulative membrane binding frequency measurements

(**Fig. 2.2d**) and dwell time analyses (**Fig. 2.2e**) further demonstrated that the PI4KIIIα-EFR3A interaction was unaffected by Y2090 phosphorylation. These results are consistent with those of a BLI experiment in which PI4KIIIα and PI4KIIIα^{pY2090} were found to associate with the immobilized C-terminus of EFR3A at nearly identical rates[89].

Although phosphorylation of PI4KIIIα did not affect its membrane dwell time in the presence of EFR3A, we did observe a marked decrease in PI4KIIIα dwell time as we decreased the concentration of SpyTag-EGFP-EFR3A tethered to the supported membrane (**Fig. 2.2e**). When there are fewer molecules of EFR3A present on the membrane, the two EFR3 binding sites of the PI4KIIIα dimer are less likely to simultaneously bind two EFR3A molecules and less likely to form a new interaction if one binding site releases from the membrane, thereby decreasing the mean dwell time of the complex. This trend serves as further confirmation of the critical role served by EFR3 in the regulation of PI4KIIIα membrane localization.

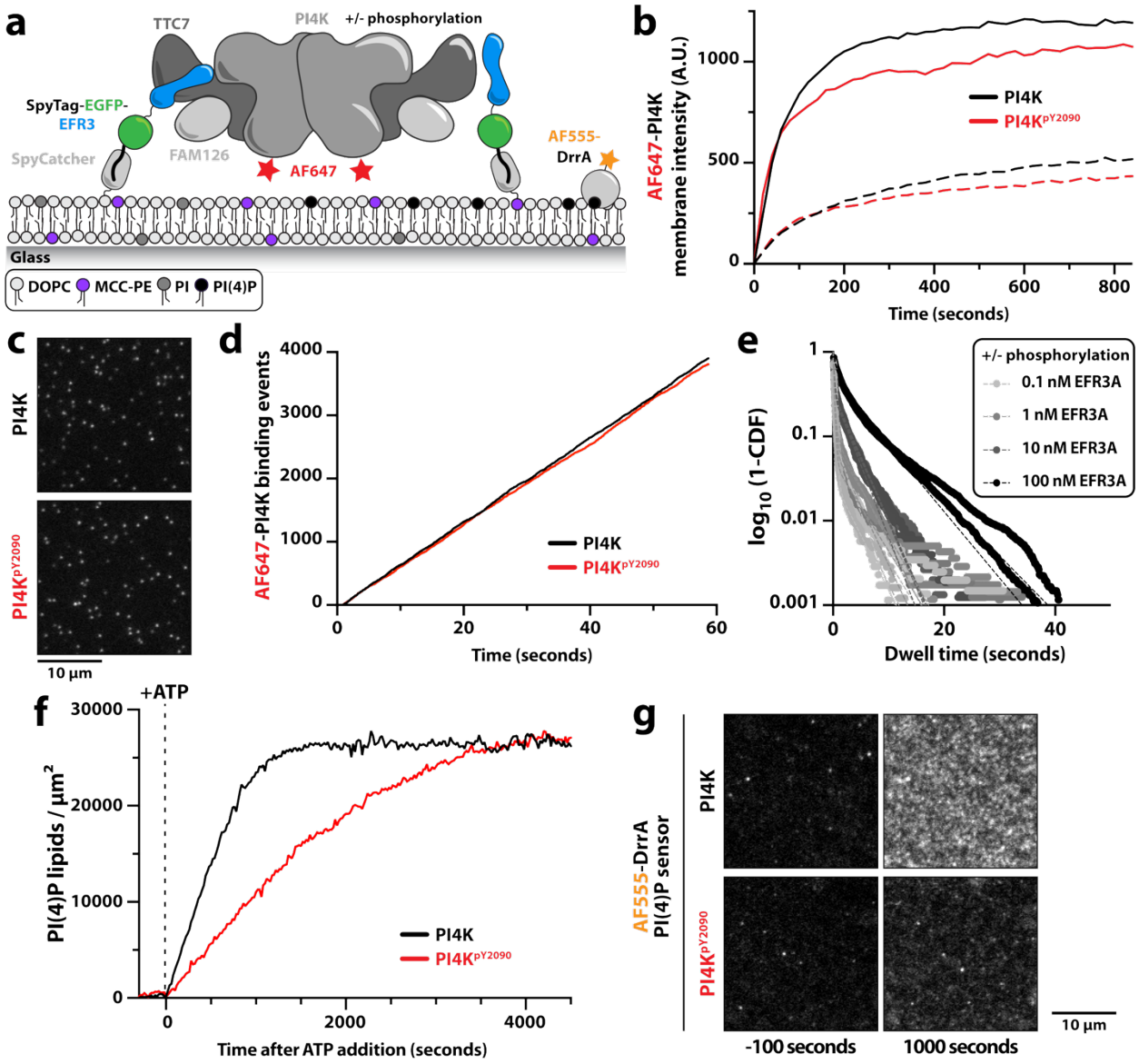

Figure 2.2 Phosphorylation of Y2090 attenuates PI4KIIIα activity without disrupting EFR3A-mediated membrane recruitment

(a) Cartoon showing the experimental design for measuring the localization and activity of the AF647-PI4KIIIα complex on an SLB in the presence of SpyTag-EGFP-EFR3A +/- phosphorylation of by LCK. SpyCatcher is covalently linked to a maleimide lipid (i.e. MCC-PE) and SpyTag-EGFP-EFR3A is conjugated to SpyCatcher via an isopeptide bond. A soluble AF555-labeled PI(4)P biosensor derived from DrrA is used to monitor PI(4)P production. Membrane localization of SpyTag-EGFP-EFR3A, AF647-PI4KIIIα, and AF555-DrrA is visualized by TIRF-M. **(b-d)** Phosphorylation of PI4KIIIα does not perturb interactions with membrane-tethered EFR3A. **(b)** Bulk membrane absorption kinetics of PI4KIIIα and PI4KIIIα^{pY2090} at 2 nM (solid lines) and 0.2 nM (dashed lines). **(c)** Representative TIRF-M images showing the localization of 0.2 nM AF647-

PI4KIIIα +/- phosphorylation on SLBs coated with EFR3A. **(d)** Representative cumulative membrane binding curves of 0.2 nM AF647-PI4KIIIα +/- phosphorylation. Membrane binding events were measured on a 3000 μm^2 membrane surface coated with EFR3A and yielded the following binding frequencies: 4.41 ± 0.2 AF647-PI4KIIIα events • pM^{-1} • μm^{-2} • s^{-1} and 4.43 ± 0.2 AF647-PI4KIIIα^{pY2090} events • pM^{-1} • μm^{-2} • s^{-1}. Errors represent standard deviation (n = 3 technical replicates). **(e)** Representative single-molecule dwell time distributions of 0.2 nM AF647-PI4KIIIα +/- phosphorylation in the presence of membrane-tethered EFR3A at concentrations ranging from 0.1 – 100 nM. Data are plotted as $\log_{10}$(1-cumulative distribution frequency) and fit with a double exponential function (dashed lines). The experiment performed in the presence of 100 nM EFR3A yielded the following time constants: τ_1 = 0.85 ± 0.06 seconds, τ_2 = 6.36 ± 0.28 seconds, α = 0.6, n = 14754 molecules for PI4KIIIα and τ_1 = 0.63 ± 0.02 seconds, τ_2 = 5.55 ± 0.23 seconds, α = 0.5, n = 12120 molecules for PI4KIIIα^{pY2090}. α represents the fraction of molecules with a characteristic dwell time of τ_1. Errors represent standard deviation (n = 3 technical replicates). **(f)** Phosphorylation attenuates PI4KIIIα lipid kinase activity. The production of PI(4)P was monitored by quantifying membrane recruitment of 20 nM AF555-DrrA (PI(4)P probe) prior to and following the addition of 1 mM ATP (dashed line). **(g)** Representative TIRF-M images showing the localization of AF555-DrrA in **(f)** before (-100 seconds) and after (1000 seconds) the addition of 1 mM ATP to stimulate AF647-PI4KIIIα lipid kinase activity. **(b-g)** Membrane composition: 86% DOPC, 10% DOPS, 2% MCC-PE (+SpyCatcher bound), and 2% PI lipids.

To determine whether phosphorylation of PI4KIIIα impacts its lipid kinase activity in the context of EFR3-mediated membrane recruitment, we used an AF555-labeled PI(4)P biosensor derived from *Legionella pneumophila* DrrA (referred to as AF555-DrrA) to monitor the production of PI(4)P on SLBs[95]. This allowed us to simultaneously visualize PI4KIIIα membrane localization and catalytic activity for both phosphorylated and unphosphorylated PI4KIIIα complexes. After allowing AF647-PI4KIIIα to equilibrate on an SLB through interactions with membrane-tethered EFR3A, lipid kinase activity measurements were initiated by adding 1 mM ATP (**Fig. 2.2f, g**). Although similar membrane densities of PI4KIIIα and PI4KIIIα^{pY2090} were achieved, PI4KIIIα^{pY2090} exhibited a notable decrease in lipid kinase activity. These results demonstrate that even when PI4KIIIα is bound to membrane-tethered EFR3, Y2090 phosphorylation attenuates

PI4KIIIα-dependent PI(4)P production and points to a localization-independent cellular PI4KIIIα regulatory mechanism.

GβGγ-dependent PI3Kγ membrane recruitment and activation is enhanced in the presence of active Ras GTPase

PI3Kγ is known to be activated by GTP-bound Ras and GβGγ subunits[28,40,77,78,96]. We set out to determine how these factors localize and activate PI3Kγ using purified proteins on SLBs containing PIP_2, the lipid substrate of this kinase (**Fig. 2.3a, d**). We visualized PI3Kγ localization by imaging AF647-labeled PI3Kγ and simultaneously monitored lipid kinase activity using an AF546-labeled LBD (PIP_3 Lipid Binding Domain) derived from BTK (Bruton's Tyrosine Kinase). As with our PI4KIIIα experiments, we allowed the system to equilibrate before spiking in 1 mM ATP. We conjugated purified H-Ras to SLBs in a biologically relevant orientation using maleimide lipids, as previously described[33], in the presence of GDP and the absence of GTP. To activate Ras, we introduced the catalytic domain of the SOS1 RasGEF (Son of Sevenless Homolog 1 Guanine Nucleotide Exchange Factor, referred to as GEF) in buffer containing GTP. When required, we allowed GβGγ subunits to bind to the SLB via a native farnesyl lipid anchor prior to introducing AF647-PI3Kγ.

We first visualized the membrane localization and activity of the full AF647-PI3Kγ complex (p110γ-p101) and found that Ras(GTP) alone did not facilitate p110γ-p101 membrane localization, whereas membrane-bound GβGγ could both recruit and activate PI3Kγ. Notably, when both Ras(GTP) and GβGγ were present, we observed a ~2-fold

increase in PI3Kγ membrane localization and a corresponding ~2-fold increase in the rate of PIP_3 generation compared to with GβGγ alone (**Fig. 2.3b, c**). These results are consistent with the findings of previous biochemical studies of PI3Kγ activation[96]. Because of its similarities to *Dictyostelium* PI3K, we expected the p110γ catalytic subunit of PI3Kγ to be more sensitive to Ras activation in the absence of GβGγ than the p110γ-p101 complex. We found that, while free p110γ was inactive in the presence of Ras(GDP), spiking in ATP in the presence of Ras(GTP) did indeed result in rapid PIP_3 generation (**Fig. 2.3e**). Although both p110γ-p101 and p110γ are activated by Ras(GTP), the p101 subunit confers the requirement for GβGγ engagement to the PI3Kγ enzyme.

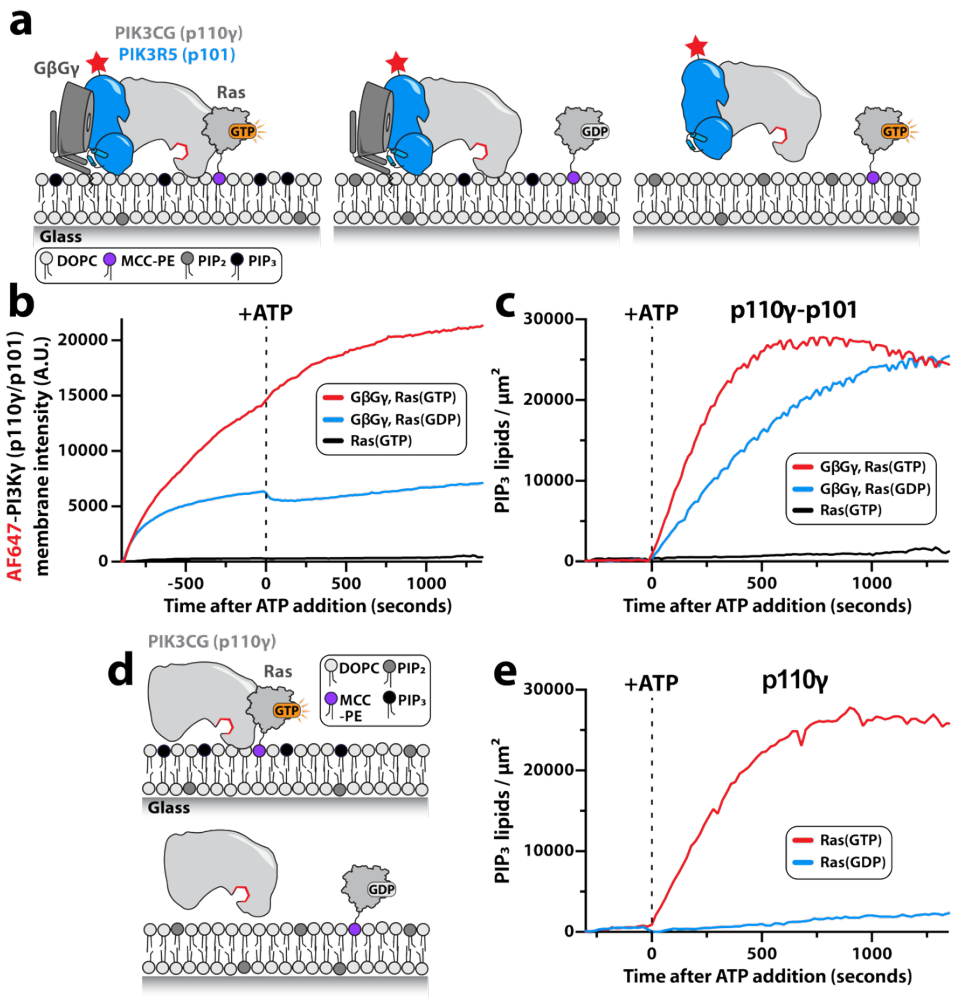

Figure 2.3 GβGγ-dependent PI3Kγ membrane recruitment and activation is enhanced in the presence of active Ras GTPase.
(a) Experimental design for reconstitution of PI3Kγ complex (p110γ-p101) activity on SLBs in the presence of both Ras(GTP) and GβGγ (left), GβGγ and Ras(GDP) (center), or Ras(GTP) only (right). **(b)** Membrane localization kinetics of 2 nM AF647-PI3Kγ (p110γ-p101) in the presence of Ras(GTP), GβGγ, or both inputs. Dashed line marks the addition of 1 mM ATP. **(b)** Kinetics of PI3Kγ (p110γ-p101)-dependent PIP_3 generation in the presence of Ras(GTP), GβGγ, or both inputs measured with 20 nM AF546-LBD prior to and following the addition of 1 mM ATP (dashed line). **(d)** Experimental design for reconstitution of PI3Kγ catalytic subunit (p110γ) activity on SLBs in the presence of Ras(GTP) (top) and Ras(GDP) (bottom). **(e)** Kinetics of PIP_3 generation by 10 nM p110γ in the presence of Ras(GTP) and Ras(GDP) measured using 20 nM AF546-LBD prior to and following the addition of 1 mM ATP (dashed line). **(b, c)** Membrane composition: 94% DOPC, 2% NiNTA, 2% MCC-PE (+Ras bound), 2% PIP_2 lipids, +/- GβGγ-farnesyl. **(e)** Membrane composition: 96% DOPC, 2% MCC-PE (+Ras bound), and 2% PIP_2 lipids.

Ras activation allows PI3Kγ activity to overcome PTEN opposition

In cells, PI3K activity is opposed by the PTEN lipid phosphatase. By including soluble PTEN in our reconstitution, we were able to balance GβGγ-dependent, Ras-independent generation of PIP_3 by the p110γ-p101 complex. When we then rapidly activated a high density of Ras molecules by introducing GEF to this reaction, we found that PI3Kγ activity was able to overcome PTEN-mediated competition (**Fig. 2.4a, b**). Similarly, we found that activating Ras in the presence of the p110γ catalytic subunit and PTEN led to a burst of PIP_3 production (**Fig. 2.4c, d**). The reconstitution consisting of the full PI3Kγ complex (p110γ-p101), Ras, GβGγ, and PTEN may behave analogously to cellular systems in which inputs from multiple pathways must be integrated to initiate a signaling event in the presence of negative regulators.

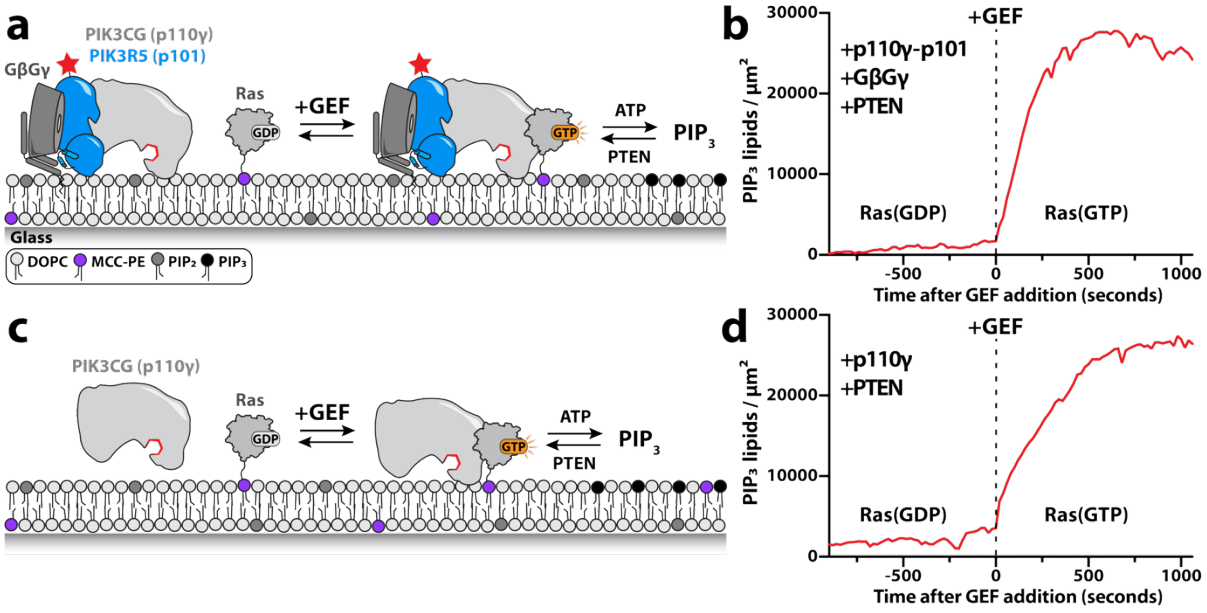

Figure 2.4 Ras activation allows PI3Kγ activity to overcome PTEN opposition.
(a, b) In the presence of membrane-bound GβGγ and Ras(GDP), 5 nM PTEN balances the lipid kinase activity of 2 nM PI3Kγ (p110γ-p101) measured with 20 nM AF546-LBD. PIP_3 production

increases rapidly when Ras is activated by the addition of 50 nM GEF (dashed line). **(c, d)** In the absence of active Ras, 5 nM PTEN balances the lipid kinase activity of 10 nM PI3Kγ catalytic subunit (p110γ) measured with 20 nM AF546-LBD. PIP_3 production increases rapidly when Ras is activated by the addition of 50 nM GEF (dashed line). **(b)** Membrane composition: 94% DOPC, 2% NiNTA, 2% MCC-PE (+Ras bound), 2% PIP_2 lipids, +GβGγ-farnesyl. **(d)** Membrane composition: 96% DOPC, 2% MCC-PE (+Ras bound), and 2% PIP_2 lipids.

DISCUSSION

In this chapter, we present an investigation into the molecular mechanisms that control the plasma membrane localization and lipid kinase activity of two members of the PI3K superfamily, PI4KIIIα and PI3Kγ. PI4KIIIα sustains the PI(4)P pool that mediates PS transport, and acts as the precursor molecule for PIP_2 and PIP_3 generation. Although depletion of plasma membrane PI(4)P through PI4KIIIα inhibition does not have a major effect on the abundance of PIP_2[10,95,97], PI4KIIIα inhibition does dramatically alter oscillations of PI(4)P and PIP_2 which play prominent roles in controlling GTPase- and actin-dependent signaling[61]. This indicates that PI(4)P flux serves a critical function in mediating signaling events downstream of PI4KIIIα and provides an impetus to better understand how PI4KIIIα activity is regulated. The most important regulator of PI4KIIIα plasma membrane localization and activity is EFR3 which is anchored to the plasma membrane via palmitoylation[44]. The C-terminal tail of EFR3 engages with TTC7 and FAM126 and deletion of this region has been shown to abolish PI4KIIIα plasma membrane recruitment[45,46]. To reconstitute PI4KIIIα membrane localization and activity on SLBs in a biologically relevant manner, it was crucial to perform our experiments in the presence of the membrane-tethered EFR3 C-terminus. Using this experimental system, we modulated PI4KIIIα membrane recruitment using a nanobody targeted to the

TTC7-EFR3 interface and investigated how phosphorylation of PI4KIIIα attenuates its lipid kinase activity.

Both gain- and loss-of-function alterations to PI4KIIIα, EFR3, TTC7, and FAM126, have been documented in human disease[4–7,47–55]. Recently, it has been proposed that PI4KIIIα inhibitors may have a place in cancer therapies in combination with PI3K- or Ras-targeting drugs although toxicity continues to present a challenge[6,7]. We reasoned that blocking EFR3-mediated plasma membrane recruitment of PI4KIIIα could be a useful approach for regulating its lipid kinase activity and potentially reveal a novel therapeutic strategy. Nanobodies have emerged as tools for stabilizing and disrupting protein-protein interactions[98]. For example, nanobodies that target the spike protein of SARS-CoV-2 (Severe Acute Respiratory Syndrome Coronavirus 2) disrupt interactions with host receptors by altering its conformational dynamics[99]. In the context of Ras signaling, nanobodies that bind to the SOS1 GEF have been shown to competitively inhibit Ras signaling[57]. Using a yeast display approach, we isolated the F3IN nanobody which binds specifically to TTC7B and competitively inhibits the EFR3-TTC7B interaction. We demonstrated that F3IN decreases EFR3A-mediated PI4KIIIα recruitment to SLBs in a dose-dependent manner. A subsequent experiment in HEK293-AT1 cells found that expression of F3IN led to reduced PI4KIIIα plasma membrane localization and decreased PI(4)P levels[46]. Although these results indicate that the F3IN nanobody may be a useful tool for selectively modulating PI4KIIIα membrane recruitment and activity in vivo, future work will need to more carefully examine the effects of blocking EFR3-mediated PI4KIIIα

recruitment in living systems and determine whether nanobodies represent a viable approach for targeting PI4KIIIα or similar enzymes in disease.

Protein phosphatases including calcineurin[62,63] and the *Drosophila* protein Pez (ortholog of the phosphatase PTPN14)[64] have been shown to play roles in regulating plasma membrane PI(4)P levels, suggesting that phosphorylation of PI4KIIIα or its adaptor proteins may be a key mechanism by which the kinase activity of the complex is regulated in cells. In yeast, phosphorylation of Efr3 disrupts Stt4-Ypp1 (orthologs of PI4KIIIα-TTC7) membrane recruitment and therefore Stt4 activity[100]. Multiple phosphorylation sites also map to the TTC7-FAM126 interfaces of mammalian EFR3A and EFR3B although these sites remain uncharacterized[101]. In this work, we identified a novel phosphorylation site at Y2090 in the kα12 helix of the PI4KIIIα enzyme and demonstrated that phosphorylation of Y2090 substantially decreases PI4KIIIα activity without affecting the structure of the complex or its ability to interact with EFR3A on SLBs. Kinases in the PI3K superfamily share a similar regulatory motif in their C-terminal kinase domain composed of helices kα7–kα12 which surround the activation loop. The final helix, kα12, is particularly important, as truncation of this region has been shown to abolish the lipid kinase activity of PI4KIIIβ, PI3Kα, PI3Kβ, and Vps34[68,102–104]. A recent cryo-EM analysis of the PI3Kα enzyme interacting with lipid nanodiscs revealed that the amphipathic kα12 helix inserts its hydrophobic face into the membrane, yielding a potential mechanism by which this C-terminal feature promotes kinase activity[71]. Notably, multiple studies have reported inhibitory phosphorylation sites within the kα12 helix of

Class I PI3Ks. PI3Kα can be phosphorylated downstream of the hippo kinases at T1061, with phosphorylation dramatically decreasing both its lipid kinase activity and recruitment to negatively charged membranes[75]. Both PI3Kβ and PI3Kδ have been reported to auto-phosphorylate kα12 residues (S1070 in PI3Kβ and S1039 in PI3Kδ)[73,74], leading to reduced lipid kinase activity. Intriguingly, both Vps34 and PI4KIIIβ also harbor reported phosphorylation sites in kα12 (Y884 in Vps34 and Y805 in PI4Kβ). Although the effects of these post-translational modifications have not yet been characterized, a Y884D-W885D mutant of Vps34 exhibits almost no lipid kinase activity[105], suggesting that Y884 phosphorylation would be inhibitory. The putative mechanism of inhibition for all kα12 phosphorylation sites is that adding a negatively charged residue to the helix leads to charge repulsion with negatively charged lipids, preventing kα12 membrane association.

While phosphorylation of Y2090 presents an intriguing potential mechanism by which cells might regulate PI4KIIIα, it remains unclear what role this site plays in the organization of PI4KIIIα signaling and which kinases are involved. DDR1, DDR2, ALK, and INSR are among the tyrosine kinases predicted to show the highest specificity for the Y2090 site[67]. Of these, we only experimentally tested INSR, which indeed resulted in 30% phosphorylation of Y2090. Notably, the SRC-family kinases LCK and SRC, which were predicted to exhibit substantially less specificity for Y2090, resulted in 90% and 40% phosphorylation, respectively. We wondered why Y2090, which proved to be readily phosphorylated, rarely appears in phospho-proteomics datasets. One of the central ways tyrosine kinase signaling can be modulated is through priming phosphorylation, where

upstream residues of the target tyrosine are phosphorylated, causing increased tyrosine phosphorylation[67]. This can complicate identification of phospho-tyrosine sites in MS proteomics. Immediately N-terminal to Y2090 is a threonine at position 2089. Intriguingly, when protein kinases are ranked for Y2090 site specificity with T2089 priming phosphorylation, there is a dramatic increase in the rank of many growth and immune kinases, including multiple members of the INSR, EPHR, EPHR, FGFR, SRC and VEGFR families, with the most highly ranked kinase being the IRR (Insulin Receptor-Related Protein). Many of these potential PI4KIIIα inhibitors are known promoters of PI3K signaling. An attractive interpretation of this trend is that regulation of PI4KIIIα by phosphorylation constitutes a previously unreported negative feedback circuit that acts on PI3K signaling by choking off the pool of PIP_2 substrate or otherwise altering the membrane environment, perhaps though changes to PS density or Ras clustering. A key limitation of our study is that the physiological context driving Y2090 phosphorylation remains undefined. When PI4KIIIα is localized to the plasma membrane, the local cellular environment likely dictates which tyrosine kinase mediates this modification. Future in vivo analyses will provide insight into the role played by Y2090 phosphorylation in the spatial patterning of lipids and crosstalk with other signaling reactions.

The Class I PI3Ks are activated by diverse cell surface receptors and small GTPases in the Ras superfamily[16]. The relationships between these classes of molecules are at the core of numerous signaling cascades[1,3,28]. Best known for its role in myeloid cells, the PI3Kγ isoform has been shown to be activated by GPCR-derived GβGγ subunits

and GTP-bound Ras GTPase and in vivo and in vitro[14,77,78,106]. We observed PIP_3 production by the PI3Kγ complex (p110γ-p101) in the presence of membrane-bound Ras and GβGγ on SLBs. In agreement with previous biochemical studies, we demonstrated that while active Ras alone is unable to robustly activate PI3Kγ, the presence of both Ras(GTP) and GβGγ leads to a ~2-fold increase in PIP_3 generation and that this increase in activity can largely be attributed to enhanced membrane localization of the complex[96]. By contrast, the p110γ catalytic subunit alone displayed substantial PIP_3 production in the presence of Ras(GTP) and the absence of the GβGγ complex. This result does not come as a surprise since human p110γ resembles the PI3K enzymes of the *Dictyostelium* slime mold in which PIP_3 generation is more tightly coupled to Ras activation[14,83]. We then introduced PTEN lipid phosphatase to our reconstitution to oppose p110γ-p101 activity in the presence of GβGγ. Under these conditions, much like for the free p110γ catalytic subunit, Ras activation provided enough of a stimulus to trigger rapid PIP_3 generation that outpaced PTEN-mediated dephosphorylation. The p101 regulatory subunit serves to modulate how signals from GPCRs and Ras GTPases are integrated by PI3Kγ.

Unlike PI(4)P and PIP_2, PIP_3 is extremely rare in resting cells and is produced rapidly during signaling events including cell migration and neurogenesis due to mechanisms of positive feedback[11–15]. PIP_3 functions as a second messenger by scaffolding a host of effector molecules to specific regions of the plasma membrane[1]. Among these are many GEFs which locally activate Ras and other small GTPases that promote PIP_3 synthesis and actin polymerization[13,28,107]. Dendritic actin networks deliver

additional activators[29] and prevent signaling molecules from diffusing away from the plasma membrane, thereby further amplifying PIP_3 generation and GTPase activation. Due to its roles in cell growth, proliferation, and migration, unchecked PI3Kγ activity quickly leads to disease[3,39,79,86]. Together with the potent feedback potential between Ras and PI3Kγ, this may provide an explanation for the p101-mediated requirement for coincident GβGγ signaling. Positive feedback within Ras and PI3Kγ signaling is the focus of Chapter Four.

The findings presented in this chapter provide new opportunities to control the plasma membrane recruitment and activity of lipid kinases and will inform future investigations of cellular signal transduction.

METHODS

Protein expression, purification, and labeling

The ybbr-PI4KIIIα-TTC7B-FAM126A(1-308aa) complex, TTC7B-FAM126A(1-308aa), F3IN nanobody, SpyTag-EGFP-(GS)-EFR3A(721-791aa), and kinase domain of LCK(225-509aa) were expressed and purified by the Burke Lab at the University of Victoria, as previously described[46,89]. The Burke Lab labeled the recombinant PI4KIIIα-TTC7B-FAM126A (1-308) complex containing an N-terminal ybbR13 motif (DSLEFIASKLA) using Sfp transferase and AF647-CoA. The F3IN nanobody was isolated by the Burke Lab from a yeast display library obtained from Dr. A.C. Kruse's laboratory at Harvard Medical School[87].

KCK-SpyCatcher. A his_{10}-TEV-SUMO-KCK-SpyCatcher fusion was expressed and purified from Rosetta(DE3) *E. coli*. The gene sequence used to recombinantly express SpyCatcher was inspired by a previously described construct[88]. Bacteria were grown at 37°C in Terrific Broth to an absorbance of 0.8 at 600 nm. Cultures were shifted to 18°C for 1 hour then induced with 0.1 mM IPTG. Expression was allowed to continue for 20 hours before harvesting. Cells were lysed in 50 mM Na_2HPO_4 [pH 8.0], 400 mM NaCl, 10 mM imidazole, 4 mM βME, 1 mM PMSF, 100 µg/ml DNase by sonication. Lysate was centrifuged at 15,000 rpm (35,000 x g) for 60 minutes in a Beckman JA-20 rotor at 4ºC. NiNTA resin was added to the supernatant and allowed to bind for 2 hours, then washed with 50 mM Na_2HPO_4 [pH 8.0], 400 mM NaCl, 30 mM imidazole, 4 mM βME. Bound protein was eluted in 50 mM Na_2HPO_4 [pH 8.0], 400 mM NaCl, 500 mM imidazole, 4 mM βME. Peak fractions were pooled and loaded onto a desalting column equilibrated in 50 mM Na_2HPO_4 [pH 8.0], 400 mM NaCl, 20 mM imidazole, 5% glycerol, 1 mM βME to remove most of the imidazole. A his_6-SenP2 protease was added to the eluted protein which was then incubated overnight at 4ºC. The cleaved protein was recirculated over NiNTA resin to capture the tag and protease. The flowthrough was concentrated in a 10 kDa MWCO Amicon-Ultra concentrator before loading onto a 120 ml Superdex 75 column equilibrated in 20 mM Tris [pH 8.0], 200 mM NaCl, 10% glycerol, 1 mM TCEP. Peak fractions were pooled, concentrated to 150 µM, and snap frozen in liquid nitrogen for storage at -80ºC.

EGFP-SpyTag. A his_{10}-TEV-SUMO-KCK-EGFP-SpyTag(AHIVMVDAYKPTK∗)[88] fusion protein was expressed in Rosetta (DE3) *E. coli*. Bacteria were grown at 37°C in Terrific Broth to an absorbance of 0.8 at 600 nm. Cultures were then shifted to 18°C for 1 h before inducing with 0.1 mM IPTG. Expression was allowed to continue for 20 hours before harvesting. Cells were lysed in 50 mM Na_2HPO_4 [pH 8.0], 400 mM NaCl, 10 mM imidazole, 4 mM βME, 1 mM PMSF, 100 µg/ml DNase by sonication. Lysate was centrifuged at 15,000 rpm (35,000 x g) for 60 minutes in a Beckman JA-20 rotor at 4ºC. NiNTA resin was added to the supernatant and allowed to bind for 2 hours, then washed with 50 mM Na_2HPO_4 [pH 8.0], 400 mM NaCl, 30 mM imidazole, 4 mM βME. Bound protein was eluted in 50 mM Na_2HPO_4 [pH 8.0], 400 mM NaCl, 500 mM imidazole, 4 mM βME. Peak fractions were pooled and loaded onto a desalting column equilibrated in 50 mM Na_2HPO_4 [pH 8.0], 400 mM NaCl, 20 mM imidazole, 5% glycerol, 1 mM βME to remove most of the imidazole. A his_6-SenP2 protease was added to the eluted protein which was then incubated overnight at 4ºC. The cleaved protein was recirculated over NiNTA resin to capture the tag and protease. The flowthrough was concentrated in a 10 kDa MWCO Amicon-Ultra concentrator before loading onto a 24 ml Superdex 75 column equilibrated in 20 mM HEPES [pH 7.0], 150 mM NaCl, 10% glycerol, and 1 mM TCEP. Peak fractions were pooled, concentrated to 484 µM, and snap frozen in liquid nitrogen for storage at -80ºC.

DrrA. The PI(4)P lipid binding domain, DrrA(544-647aa), was expressed in BL21(DE3) *E. coli* as a his_6-MBP-TEV-GGGGG-DrrA(544-647aa) fusion as previously

described[30]. Bacteria were grown at 37°C in Terrific Broth to an absorbance of 0.8 at 600 nm. Cultures were shifted to 18°C for 1 hour then induced with 0.1 mM IPTG. Expression was allowed to continue for 20 hours before harvesting. Cells were lysed in 50 mM Na_2HPO_4 [pH 8.0], 300 mM NaCl, 0.4 mM βME, 1 mM PMSF, 100 µg/ml DNase using a microfluidizer. Lysate was centrifuged at 16,000 rpm (35,172 x g) for 60 minutes in a Beckman JA-17 rotor at 4ºC. Lysate was circulated over a 5 ml HiTrap Chelating column (GE Healthcare, Cat# 17-0409-01) charged with $CoCl_2$. Bound protein was eluted with a linear gradient of imidazole (0-500 mM). his_6-TEV protease was added to peak fractions to cleave off the his_6-MBP tag. The TEV cleavage was performed while dialyzing the DrrA against 4 liters of buffer containing 50 mM Na_2HPO_4 [pH 8.0], 300 mM NaCl, and 0.4 mM βME for 16 hours at 4ºC. The next day, dialysate containing cleaved protein was recirculated over a 5 ml HiTrap Chelating column to capture the his_6-MBP and his_6-TEV protease. Flowthrough containing GGGGG-DrrA(544-647aa) was concentrated using a 5 kDa MWCO Vivaspin 20 concentrator before loading on to a Superdex 75 size exclusion column equilibrated in 20 mM Tris [pH 8.0], 200 mM NaCl, 10% glycerol, 1 mM TCEP. Peak fractions were pooled and snap frozen in liquid nitrogen for storage at -80ºC.

Sortase-mediated peptide ligation was used to label GGGGG-DrrA(544-647aa) with AlexaFluor555 (AF555) as previously described[30]. In brief, the sortase labeling reaction was prepared by combining 75 µM AF555-LPETGG, 28 µM GGGGG-DrrA(544-647aa), and 5 µM NusA-SortaseA in buffer containing 50 mM Tris [pH 8.0], 150 mM NaCl, 6 mM $CaCl_2$, 1 mM TCEP. The labeling reaction was incubated at 18ºC for 16 hrs.

Unreacted AF555-LPETGG was mostly removed using a Nap25 G25 Sephadex desalting column. The remaining AF555-LPETGG and NusA-SortaseA were separated from AF555-LPETGGGGG-DrrA(544-647aa) using a Superdex 75 size exclusion column equilibrated in 20 mM Tris [pH 8.0], 200 mM NaCl, 10% glycerol, 1 mM TCEP. Peak fractions were pooled and snap frozen in liquid nitrogen for storage at -80ºC.

NusA-SortaseA. A NusA-his_6-SortaseA fusion was expressed in BL21(DE3) *E. coli*. Bacteria were grown at 37°C in Terrific Broth to an absorbance of 0.8 at 600 nm. Cultures were shifted to 18°C for 1 hour then induced with 0.1 mM IPTG. Expression was allowed to continue for 20 hours before harvesting. Cells were lysed in 50 mM Na_2HPO_4 [pH 8.0], 400 mM NaCl, 4 mM βME, 1 mM PMSF, 100 µg/ml DNase by sonication. Lysate was centrifuged at 15,000 rpm (35,000 x g) for 60 minutes in a Beckman JA-20 rotor at 4ºC. NiNTA resin was added to the supernatant and allowed to bind for 2 hours, then washed with 50 mM Na_2HPO_4 [pH 8.0], 400 mM NaCl, 10 mM imidazole, 4 mM βME. Bound protein was eluted in 50 mM Na_2HPO_4 [pH 8.0], 400 mM NaCl, 500 mM imidazole, 4 mM βME. Peak fractions were pooled and dialyzed against 4 liters of buffer containing 20 mM Tris [pH 8.0], 200 mM NaCl, 5 mM βME. Dialysate was concentrated in a 10 kDa MWCO Amicon-Ultra concentrator before loading onto a 120 ml Superdex 75 column equilibrated in 20 mM Tris [pH 8.0], 150 mM NaCl, 10% glycerol, 1 mM TCEP. Peak fractions were pooled and snap frozen in liquid nitrogen for storage at -80ºC. Note that the NusA solubility tag was intentionally left attached to increase the protein's molecular

weight to 75 kDa. This facilitated separation from DrrA(544-647aa) after labeling with AF555.

p110γ(PIK3CG), ybbr-p101(PIK3R5). High Five insect cells were infected with baculovirus to drive the dual expression of human p110γ(PIK3CG, 1-1102aa) and TwinStrept-his$_{10}$-TEV-ybbr-p101(PIK3R5, 1-880aa) from polyhedrin promoters as previously described[96]. The sequence of the ybbR13 motif was DSLEFIASKLA[108]. BACMIDs and baculovirus were generated following protocols previously described[109]. Optimal protein expression conditions were empirically determined to minimize cell death and maximize protein yield (typically 1.5-2% vol/vol final concentration of P2 virus). After 48 hours of protein expression, cells were harvested and pellets were frozen at -80°C. The PI3Kγ complex was purified using previously published protocols[58]. In brief, cells were lysed in 20 mM Tris [pH 8.0], 100 mM NaCl, 10 mM imidazole, 5% glycerol, 2 mM βME, 1 mM PMSF, 100 µg/ml DNase by sonication. After lysis, Triton-X was added to a final concentration of 0.1%. Lysate was centrifuged at 30,000 rpm for 60 minutes in a Beckman TI-45 rotor at 4ºC. NiNTA resin was added to the supernatant and allowed to bind for 1 hour, then washed with 20 mM Tris [pH 8.0], 100 mM NaCl, 10 mM imidazole, 5% glycerol, 2 mM βME. Bound protein was eluted in 20 mM Tris [pH 8.0], 100 mM NaCl, 500 mM imidazole, 5% glycerol, 2 mM βME. Peak fractions were pooled, bound to Strep-Tactin Sepharose resin (IBA 2-1201-002), and washed with 100 mM Tris [pH 8.0], 150 mM NaCl, 1 mM EDTA. Bound protein was eluted in 100 mM Tris [pH 8.0], 150 mM NaCl, 1 mM EDTA, 2.5 mM desthiobiotin (Sigma, Cat #D1411) and a his$_6$-tagged TEV protease

was added to cleave off the his_6 affinity tag. The solution was dialyzed against 4 liters of buffer containing 20 mM Tris [pH 8.0], 150 mM NaCl, 10% glycerol, 1 mM TCEP. The dialysate was concentrated in a 100 kDa MWCO Amicon-Ultra concentrator and loaded on a Superdex 200 gel filtration column equilibrated in 20 mM Tris [pH 8.0], 150 mM NaCl, 10% glycerol, 10% glycerol, 1 mM TCEP. Peak fractions were pooled and snap frozen in liquid nitrogen for storage at -80ºC. To fluorescently label the PI3Kγ complex (p110γ-ybbr-p101), frozen protein was thawed and combined with Sfp transferase and AlexaFluor647-CoA (AF647-CoA) as previously described[58]. The final labeled PI3Kγ complex was separated from unreacted AF647-CoA and Sfp using a Superdex 200 gel filtration column equilibrated in 20 mM Tris [pH 8], 150 mM NaCl, 10% glycerol, 1 mM TCEP, 0.05% CHAPS. Peak fractions were pooled and concentrated before they were snap frozen in liquid nitrogen for storage at -80ºC.

p110γ(PIK3CG). High Five insect cells were infected with baculovirus to drive the expression of human his_{10}-TEV-p110γ(PIK3CG, 1-1104aa). BACMIDs and baculovirus were generated following protocols previously described[109]. After 72 hours of protein expression, cells were harvested and pellets were frozen at -80°C. After thawing, cells were lysed by Dounce homogenization in buffer containing 20 mM Tris [pH 8.0], 300 mM NaCl, 10 mM imidazole, 5% glycerol, 2 mM βME, 1 mM PMSF, 1 Sigma protease inhibitor tablet, 100 µg/ml DNase. Lysate was centrifuged at 140,000 x *g* for 45 minutes in a Beckman TI-70 rotor at 4ºC. NiNTA resin was added to the supernatant and allowed to bind for 70 minutes, then washed with 20 mM Tris [pH 8.0], 300 mM NaCl, 30 mM

imidazole, 5% glycerol, 2 mM βME. Bound protein was eluted in 20 mM Tris [pH 8.0], 300 mM NaCl, 300 mM imidazole, 5% glycerol, 2 mM βME. Peak fractions were pooled and loaded onto a G25 Sephadex desalting column equilibrated in 20 mM Tris [pH 8.0], 100 mM NaCl, 1 mM TCEP. Peak fractions were pooled and loaded onto a 5 ml HiTrap Heparin column. p110γ eluted at ~490 mM NaCl. These fractions were supplemented with 5% glycerol and 0.05% CHAPS. A TEV protease was added to cleave off the his_{10}-TEV tag during an overnight incubation at 4ºC. The protein was concentrated in a 50 kDa MWCO VivaSpin 6 concentrator and loaded on a Superdex 200 gel filtration column equilibrated in 20 mM HEPES [pH 7.5], 150 mM NaCl, 10% glycerol, 0.05% CHAPS, 1 mM TCEP. Peak fractions were pooled and snap frozen in liquid nitrogen for storage at -80ºC.

LBD-SNAP-AF546. The LBD (PIP_3 Lipid Binding Domain) derived from BTK was recombinantly expressed and purified as a his_6-SUMO-BTK(PH-TH,R49S/K52S)-SNAP fusion protein using a protocol previously described[110]. Purified LBD-SNAP was labeled with 1.5x molar excess of SNAP-Surface Alexa546 dye (NEB, Cat# S9132S) overnight at 4ºC in buffer containing 20 mM Tris [pH 8.0], 200 mM NaCl, 1 mM TCEP. The next day, the labeled protein was loaded onto a PD10 desalting column equilibrated in buffer containing 20 mM Tris [pH 8.0], 200 mM NaCl, 10% glycerol, 1 mM TCEP to remove most of the free SNAP dye. It was then concentrated in an Amicon-Ultra concentrator and loaded onto a Superdex 75 column equilibrated in 20 mM Tris [pH 8.0], 200 mM NaCl, 10% glycerol, 1 mM TCEP. Unreacted SNAP dye and labeled protein were separated by

size exclusion chromatography. The peak fractions were pooled, concentrated, aliquoted, and snap frozen in liquid nitrogen for storage at -80ºC.

H-Ras. A gene sequence encoding human H-Ras was expressed in BL21(DE3) Rosetta *E. coli* as a his_6-TEV-H-Ras(1-181aa, C118S) fusion as previously described[111]. Bacteria were grown at 37°C in Terrific Broth to an absorbance of 0.8 at 600 nm. Cultures were shifted to 18°C for 1 hour then induced with 0.1 mM IPTG. Expression was allowed to continue for 20 hours before harvesting. Cells were lysed in 50 mM Na_2HPO_4 [pH 8.0], 300 mM NaCl, 10 mM imidazole, 4 mM βME, 1 mM PMSF, 100 µg/ml DNase by sonication. Lysate was centrifuged at 15,000 rpm (35000 x *g*) for 60 minutes in a Beckman JA-20 rotor at 4ºC. NiNTA resin was added to the supernatant and allowed to bind for 1 hour, then washed with 50 mM Na_2HPO_4 [pH 8.0], 300 mM NaCl, 10 mM imidazole, 4 mM βME. Bound protein was eluted in 50 mM Na_2HPO_4 [pH 8.0], 400 mM NaCl, 500 mM imidazole, 4 mM βME. Peak fractions were pooled and a TEV protease was added to cleave off the his_6-TEV tag. The solution was dialyzed against 4 liters of buffer containing 50 mM Na_2HPO_4 [pH 8.0], 300 mM NaCl, 5% glycerol, 0.4 mM βME. Dialysate containing cleaved protein was recirculated over NiNTA resin. Flowthrough was concentrated in a 10 kDa MWCO Amicon-Ultra concentrator before loading onto a 124 ml Superdex 75 column equilibrated in 20mM Tris [pH 8.0], 200 mM NaCl, 10% glycerol, 0.5 mM TCEP. Peak fractions were pooled, concentrated to a minimum concentration of 500 µM, and snap frozen in liquid nitrogen for storage at -80ºC.

GEF. A gene sequence encoding the catalytic domain of SOS1 (referred to as GEF) was expressed in BL21(DE3) *E. coli* containing vectors for constitutive expression of Trigger factor and rare tRNAs (i.e. pRIL) as a his_6-TEV-SosCat(564-1049aa) fusion protein as previously described[112]. Bacteria were grown at 37°C in Terrific Broth to an absorbance of 0.8 at 600 nm. Cultures were shifted to 18°C for 1 hour then induced with 0.5 mM IPTG. Expression was allowed to continue for 22 hours before harvesting. Cells were lysed in 50 mM Na_2HPO_4 [pH 8.0], 400 mM NaCl, 10 mM imidazole, 4 mM βME, 1 mM PMSF, 100 µg/ml DNase by sonication. Lysate was centrifuged at 15,000 rpm (35000 x g) for 60 minutes in a Beckman JA-20 rotor at 4ºC. NiNTA resin was added to the supernatant and allowed to bind for 1 hour, then washed with 50 mM Na_2HPO_4 [pH 8.0], 400 mM NaCl, 10 mM imidazole, 4 mM βME. Bound protein was eluted in 50 mM Na_2HPO_4 [pH 8.0], 400 mM NaCl, 500 mM imidazole, 4 mM βME. Peak fractions were pooled and a TEV protease was added to cleave off the his_6-TEV tag. The solution was dialyzed against 4 liters of buffer containing 20 mM HEPES [pH 7.0], 400 mM NaCl, 20 mM imidazole, 5% glycerol 0.4 mM βME. Dialysate containing cleaved protein was recirculated over NiNTA resin. Flowthrough was concentrated in a 30 kDa MWCO Amicon-Ultra concentrator to a volume of 5 ml before loading onto a 124 ml Superdex 75 column equilibrated in 20 mM Tris [pH 8.0], 150 mM NaCl, 10% glycerol, 1 mM TCEP. Peak fractions were pooled and snap frozen in liquid nitrogen for storage at -80ºC.

Farnesylated GβGγ complex. Sf9 insect cells were infected with baculovirus (2% vol/vol) to drive the dual expression of his_6-TEV-$G\gamma_2$(1-71aa) and Gb_1(1-340aa)

polyhedrin promoters as previously described[110]. After 48 hours of expression at 27°C, cells were harvested and pellets were frozen at -80°C. Cells were lysed in buffer containing 50 mM HEPES [pH 8.0], 100 mM NaCl, 3 mM $MgCl_2$, 0.1 mM EDTA [pH 8.0], 10 μM GDP, 10 mM βME, 1 Sigma protease inhibitor tablet, 1 mM PMSF, 100 μg/ml DNase by sonication and centrifuged at 800 x *g* at 4ºC. The supernatant was centrifuged at 100,000 x *g* for 30 minutes in a Beckman TI-70 rotor at 4ºC. The pellet was resuspended in 50 mM HEPES [pH 8.0], 50 mM NaCl, 3 mM $MgCl_2$, 1% sodium cholate (wt/vol), 10 μM GDP, 10 mM βME, 1 mM PMSF, Dounce homogenized, stirred for 1 hour, and centrifuged at 100,000 x *g* for 45 minutes in a Beckman TI-70 rotor at 4ºC. The supernatant was diluted 5-fold in 20 mM HEPES [pH 7.7], 100 mM NaCl, 0.1 % $C_{12}E_{10}$ (Polyoxyethylene (10) lauryl ether), 20 mM imidazole, 2 mM βME and allowed to bind to NiNTA resin for 2 hours. The resin was washed with 20 mM HEPES [pH 7.7], 100 mM NaCl, 0.1 % $C_{12}E_{10}$, 20 mM imidazole, 2 mM βME. The Gα subunit was eluted in 20 mM HEPES [pH 7.7], 100 mM NaCl, 0.1 % $C_{12}E_{10}$, 20 mM imidazole, 2 mM βME, 50 mM $MgCl_2$, 10μM GDP, 30 μM $AlCl_3$, 10 mM NaF at 30ºC. The complex was eluted in 20 mM Tris [pH 8.0], 25 mM NaCl, 0.1 % $C_{12}E_{10}$, 200 mM imidazole, 2 mM βME and a his_6 TEV protease was added to cleave the his_6 tag off the $G\gamma_2$ subunit. The solution was loaded onto a G25 Sephadex desalting column equilibrated in 20 mM Tris [pH 8.0], 25 mM NaCl, 8 mM CHAPS, 2 mM TCEP. Peak fractions were pooled and loaded onto a MonoQ anion exchange column. The GβGγ complex eluted at ~180 mM NaCl. These fractions were concentrated in a 30 kDa MWCO Amicon-Ultra concentrator and loaded on a Superdex

75 gel filtration column equilibrated in 20 mM Tris [pH 8.0], 100 mM NaCl, 8 mM CHAPS, 2 mM TCEP. Peak fractions were pooled and snap frozen in liquid nitrogen for storage at -80ºC.

PTEN. PTEN was expressed in High Five insect cells as a PTEN(1-352aa)-GGLPETGGGY-MxeGyrA-his_6. Although not utilized in this study, the LPETGG motif was added for sortase-mediated peptide ligation. The tyrosine positioned N-terminal to the MxeGyrA intein increases the efficiency of DTT-induced intein cleavage. High Five cells expressing PTEN were lysed by Dounce homogenization in buffer containing 50 mM Na_2HPO_4 [pH 8.0], 10 mM imidazole, 300 mM NaCl, 0.1% Triton X-100, 0.5 mM ABESF, 100 µg/ml DNase, Roche protease inhibitor tablet (1 per 100 ml lysis buffer), and no reducing agent. Lysate was clarified by centrifugation at 35,000 rpm in Beckman Ti-70 rotor for 45 minutes. Clarified cell lysate was incubated with 5 ml NiNTA resin in a beaker with a stir bar at 4ºC for 1 hour. Resin was washed with 100 ml buffer containing 50 mM Na_2HPO_4 [pH 8.0], 10 mM imidazole, 400 mM NaCl. PTEN(1-352aa)-GGLPETGGGY-MxeGyrA-his_6 was eluted from the NiNTA resin with 20 ml 50 mM Na_2HPO_4 [pH 8.0], 500 mM imidazole, 400 mM NaCl. The MxeGyrA-his_6 was cleaved off by incubating with 10 mM DTT overnight at 4ºC. To separate PTEN(1-352aa)-GGLPETGGGY (pI = 8.18) and MxeGyrA-his_6 (pI = 5.81), the cleaved protein was desalted into buffer containing 20 mM HEPES [pH 7.0], 50 mM NaCl, 2 mM DTT. The proteins were then load on a MonoS column equilibrated in 20 mM HEPES [pH 7.0], 50 mM NaCl, 2 mM DTT and resolved with a 5-100% salt gradient (100% = 20 mM HEPES [pH 7.0], 1 M NaCl). PTEN eluted

from the MonoS column in the presence of 500 mM NaCl at pH 7.0. Peak fractions were pooled and concentrated in a 10 kDa MWCO VivaSpin 6 concentrator. PTEN was loaded onto a Superdex 75 equilibrated in buffer containing 20 mM Tris [pH 8.5], 200 mM NaCl, 10% glycerol, 0.5 mM TCEP. Peak fractions were pooled, concentrated to 112 μM, and snap frozen in liquid nitrogen for storage at -80ºC.

Supported lipid bilayer experiments

Preparation of supported lipid bilayers. The following lipids were used to generate Small Unilamellar Vesicles (SUVs) and subsequently supported lipid bilayers: 1,2-dioleoyl-sn-glycero- 3-phosphocholine (18:1 DOPC, Avanti #850375C), 1,2-dioleoyl-sn-glycero-3-phospho-L-serine (18:1 DOPS, Avanti #840035C), L-α-phosphatidylinositol-4,5-bisphosphate (Brain PIP_2, Avanti #840046X), 1,2-dioleoyl-sn-glycero-3-phosphoethanolamine-N-[4-(p-maleimidomethyl) cyclohexane-carboxamide] (18:1 MCC-PE, Avanti #780201C), phosphatidylinositol from bovine liver (PI, Avanti #840042C), and 1,2-dioleoyl-sn-glycero-3-[(N-(5-amino-1-carboxypentyl)iminodiacetic acid)succinyl] (18:1 DGS-NTA(Ni), Avanti #790404C). To prepare SUVs, a total of 2 μmoles of lipids were combined in a 35 ml glass round bottom flask containing ~2 ml chloroform.

Lipids were dried to a thin film using rotary evaporation with the glass round-bottom flask submerged in a 42ºC water bath. The lipid film was then resuspended in 2 ml filtered PBS [pH 7.4] (Corning, cat# 46-013-CM), bringing the lipid suspension to a final concentration of 1 mM. All lipid mixtures expressed as percentages (e.g. 98% DOPC, 2% PIP_2) are equivalent to molar fractions. To generate 50 nm SUVs, the 1 mM lipid mixture

was extruded through a 0.05 μm pore size 19 mm polycarbonate (PC) membrane (Cytiva Whatman, Cat# 800308) with filter supports (Cytiva Whatman, Cat# 230300) on both sides of the PC membrane.

To create supported lipid bilayers, coverglass (25x75 mm, IBIDI, Cat #10812) was initially cleaned with 2% Hellmanex III (Fisher, Cat #14-385-864) that was heated to 60-70ºC in a glass coplin jar and incubated for at least 30 minutes. After rinsing the Hellmanex-cleaned glass with MilliQ water, the coverglass was etched with Piranha solution (1:3, hydrogen peroxide:sulfuric acid) for 10-15 minutes. Etched coverglass that was rinsed and stored in MilliQ water, was removed from the Coplin jar and rapidly dried with nitrogen gas before adhering to a 6-well, sticky-side chamber (IBIDI, Cat #80608). To create a supported lipid bilayer, a total lipid concentration of 0.25 mM SUVs in PBS [pH 7.4] was flowed into the IBIDI chamber. After 30 minutes of incubation, supported membranes were washed with 5 ml PBS [pH 7.4] to remove non-absorbed SUVs. Membrane defects were then blocked for ~5 minutes with 1 mg/ml β-casein (ThermoFisher, Cat #37528) diluted in PBS [pH 7.4]. To reduce the fraction of immobile proteins on SLBs, the 10 mg/ml β-casein solution was centrifuged in a TLA120.2 at 100,000 rpm (434,513 x *g*) for 30 minutes at 4ºC using an Optima MAX-TL ultracentrifuge. After blocking bilayers with β-casein, membranes were washed again with 1 ml PBS [pH 7.4] and 1 ml PBS [pH 7.4], 1 mM $MgCl_2$, 100 μM GDP, 0.1 mM TCEP prior to SpyCatcher or H-Ras conjugation. Prior to imaging, supported membranes were washed with TIRF-M imaging buffer.

Membrane conjugation. Conjugation of SpyCatcher to supported membranes was achieved as previously described[110]. SpyCatcher containing a single N-terminal cysteine (i.e. thiol) was coupled to supported membranes containing 2% MCC-PE lipids. For membrane coupling, 20 μM SpyCatcher in buffer containing PBS [pH 7.4], 1 mM $MgCl_2$, 0.1 mM TCEP was incubated in a flow chamber for 2 hours at 23ºC. Unreacted MCC-PE lipids were then quenched for 10 minutes in 5 mM βME diluted in PBS [pH 7.4]. Quenched membranes were then washed and stored in PBS [pH 7.4], 1 mM $MgCl_2$, 0.1 mM TCEP prior to imaging.

To attach SpyTag-EGFP-EFR3A or EGFP-SpyTag to membrane-bound SpyCatcher, a solution containing 0.1-100 nM protein was flowed into the prepared chamber. After a 20 minute incubation, unbound SpyTag proteins were flushed from the chamber with TIRF-M buffer. Based on fluorescence brightness, incubating 100 nM EGFP-SpyTag for 20 minutes resulted in a final membrane density of 10-50 tethered molecules per μm^2.

For experiments involving membrane conjugated H-Ras, β-casein-blocked supported lipid bilayers containing MCC-PE lipids were incubated for 2 hours with 30-35 μM H-Ras at 23ºC in buffer containing PBS [pH 7.4], 1 mM $MgCl_2$, 100 μM GDP, 0.1 mM TCEP. Bilayers were quenched in PBS [pH 7.4], 5 mM βME for 10 minutes before washing with PBS [pH 7.4], 1 mM $MgCl_2$, 100 μM GDP, 0.1 mM TCEP. The resulting Ras membrane density ranged from 1000-2000 molecules/μm^2 as previously described[33].

For experiments involving GβGγ, bilayers were incubated with 25 nM GβGγ (native farnesyl lipid anchor) for 20 minutes. Unbound GβGγ was flushed out of the chamber with TIRF-M imaging buffer.

TIRF microscopy imaging buffer. All supported lipid bilayer TIRF-M experiments were performed in 200 µl reaction volumes using the following reaction buffer: 20 mM HEPES [pH 7.0], 150 mM NaCl, 1 mM ATP (Sigma, Cat #A2383-10G), 100 µM GTP, 5 mM $MgCl_2$, 0.5 mM EGTA, 20 mM glucose, 200 µg/ml β-casein (ThermoScientific, Cat #37528), 20 mM βME, 320 µg/ml glucose oxidase (Serva, Cat #22780.01 *Aspergillus niger*), 50 µg/ml catalase (Sigma, Cat #C40-100MG Bovine Liver), and 2 mM Trolox (Cayman Chemicals, Cat #10011659). For ATP spike-in experiments, ATP was initially omitted from buffer and 1 mM ATP was spiked in at indicated timepoint. Perishable reagents (i.e. glucose oxidase, catalase, and Trolox) were added 5-10 minutes before initiating biochemical reconstitutions on SLBs and acquiring images. All reactions in this study were reconstituted and visualized on a TIRF microscope at 23ºC.

Microscope hardware and imaging acquisition. Imaging experiments were performed using an inverted Nikon Ti2 microscope using either a 60x (1.49 NA) or 100x (1.49 NA) oil immersion Nikon TIRF objective. The x-axis and y-axis positions were controlled using a Nikon motorized stage, joystick, and NIS element software. Fluorescently labeled proteins were excited with either a 488, 561, or 637 nm OBIS laser diode (Coherent Inc. Santa Clara, CA) controlled with a Vortran laser launch (Sacramento, CA) and acousto-optic tuneable filters (AOTF) control. Excitation and

emission light was transmitted through a multi-bandpass quad filter cube (C-TIRF ULTRA HI S/N QUAD 405/488/561/638; Semrock) containing a dichroic mirror. For bulk excitation of fluorescent biosensors, laser power measured through a 60x TIRF objective ranged from 0.5-2 mW. Fluorescence emission was detected on an iXion Life 897 EMCCD camera (Andor Technology Ltd., UK) after passing through a Nikon Ti2 emission filter wheel containing the following 25 mm emission filters: ET525/50M, ET600/50M, ET700/75M (Semrock). All experiments were performed at room temperature (23ºC). Microscope hardware was controlled with Nikon NIS elements.

Single particle tracking and analysis

Single fluorescent PI4KIIIα complexes bound to supported lipid bilayers were identified and tracked using the ImageJ/Fiji TrackMate plugin[113,114] as previously described[109]. Image stacks were loaded into ImageJ/Fiji as .nd2 files. Using the LoG detector, fluorescent particles were identified based on their size, brightness, and signal-to-noise ratio. The LAP tracker was used to generate trajectories that followed particle displacement as a function of time. Particle trajectories were then filtered based on Track Start (particles at start of movie were removed), Track End (particles at end of movie were removed), Duration (particles present for less than 2 frames were removed), and Track displacement (immobilized particles were removed). The output files from TrackMate were then analyzed using Prism 11 graphing software.

To calculate the cumulative membrane binding frequency of AF647-PI4KIIIα, data were extracted from 1 minute single-molecule TIRF microscopy movies collected at 20

frames/s. Every AF647-PI4KIIIα membrane docking event tracked via the TrackMate plugin was time stamped. This allowed us to determine the exact frame when an AF647-PI4KIIIα molecule was first detected, which was then scored as a single-membrane binding event. Although every AF647-PI4KIIIα molecules was tracked until membrane dissociation or photobleaching, only new AF647-PI4KIIIα membrane docking events were counted to calculate the cumulative membrane binding frequency. Data shown in **Fig. 2.1c** and **Fig. 2.2d** were collected with three technical replicates.

To calculate membrane dwell times as shown in **Fig. 2.2e**, Cumulative Distribution Frequency (CDF) plots were created. The bin size was set to the image acquisition frame interval (i.e. 52 ms). The $\log_{10}$(1-cumulative distribution frequency) was plotted as a function of dwell time and fit to a single or double exponential curve as previously described[109]. Each data set contained dwell times measured for n >1000 trajectories.

BRIDGE TO CHAPTER THREE

In Chapter Two, we discussed how the membrane localization and activity of enzymes in the PI3K superfamily are regulated by lipidated proteins. Specifically, we demonstrated that the GTP-bound form of Ras GTPase is an important activator of PI3Kγ. Ras is itself activated downstream of ligand-bound plasma membrane receptors, a process that often occurs asymmetrically across the cell cortex. In cells, mechanisms of signal adaptation limit the duration of Ras signaling events. To study the dynamics of Ras and PIP_3 signaling reactions in vitro, a mimetic for this type of transient, spatially patterned

activation is required. In Chapter Three, we describe the development of a light-inducible system that allows us to spatiotemporally control Ras activation on SLBs.

CHAPTER THREE

RECONSTITUTION OF SPATIOTEMPORALLY CONTROLLED RAS ACTIVATION USING LIGHT-INDUCED HETERODIMERIZATION

*This chapter contains previously published and unpublished co-authored material.

Doerr, S., Olavarrieta-Colasurdo, A. & Hansen, S. D. Reconstitution of Ras-PI3Kγ membrane communication and feedback using light-induced signaling inputs. *BioRxiv* (2026).

The following experiments were designed and performed by Dr. Scott Hansen and Sophia Doerr.

INTRODUCTION

Because Ras signaling at the plasma membrane governs the localization and activity of numerous effector molecules within diverse signaling pathways, the spatial and temporal regulation of Ras activation has considerable implications for cell behavior and health[18]. Ras molecules are activated by GEFs (Guanine Nucleotide Exchange Factors) and inactivated by GAPs (GTPase Activating Proteins) and most oncogenic Ras mutations impact its interactions with these regulators[18]. Although innovative reconstitutions on Supported Lipid Bilayers (SLBs) have provided biochemical insight into small GTPase regulation[31,115,116], kinetic measurements are often made using GAPs and GEFs in isolation to drive reactions in a single, irreversible direction. By contrast, cell signaling reactions involving small GTPases are typically transient and reversible due to global negative regulation and product-induced negative feedback loops[23]. The duration

of Ras activation is not trivial since different signaling time scales can lead to distinct cell fates[22]. Cellular Ras activity is also spatially regulated, both within plasma membrane microdomains[117,118] and across the entire cell cortex[21,83]. Importantly, GAPs and GEFs often localize to the same cellular regions where they compete to establish distinct steady-state levels of Ras(GTP)[18,116,119]. The dynamic interconversion between Ras(GDP) and Ras(GTP) gives rise to unique cellular emergent properties such as bistability[120], cortical excitability[24], and polarity[121].

To mimic the spatiotemporal dynamics of cell signaling events, we developed an assay that relies on the iLID (improved Light-Inducible Dimer) system[35] to reversibly control the membrane localization of regulatory signaling molecules in vitro. This system leverages the light-inducible heterodimerization of an engineered *Avena sativa* LOV2 domain (iLID) and bacterial SspB (Stringent response protein B)[35,36]. Exposure to blue light leads to undocking of the Jα helix within the iLID protein. This exposes an SsrA peptide capable of association with SspB. For cell biologists, this system has become an important tool for investigating cell polarity and signal transduction due to its rapid kinetics and high spatial precision[122,123]. Notable applications include the recruitment of Rho-family GEFs to modulate the barrier strength of an endothelial cell monolayer[124], the recruitment of PI3K to steer migrating neutrophils[125], and the recruitment of a RasGEF to spatially pattern Erk signaling in *Drosophila* embryos[126]. Here, we demonstrate the utility of the iLID-SspB system for controlling inputs to signaling reactions in vitro. Light-induced heterodimerization allows us to rapidly shift steady-state reaction conditions and visualize

the dynamic response of a reconstituted Ras activation reaction in the presence of GAP-mediated negative regulation. Combining this system with spatial control granted by a DMD (Digital Micromirror Device) enables us to trigger transient Ras activation in defined, micron-scale bilayer regions.

RESULTS

A 488 nm light pulse results in transient iLID-SspB heterodimerization on supported lipid bilayers

We optimized the iLID system[35] to control the localization of purified proteins on SLBs. For these experiments, purified his_{10}-mNeonGreen-iLID (referred to as iLID) was stably tethered to SLBs using nickel-chelating lipids and visualized by TIRF-M (Total Internal Reflection Fluorescence Microscopy). In the absence of 488 nm light, iLID adopts a conformation that sterically occludes its SsrA peptide from interacting with its soluble binding partner, SspB (**Fig. 2a**)[35]. Although iLID is considered "closed" in the dark, it is still conformationally dynamic and displays a weak affinity for some SspB variants[35]. To measure the degree of light-independent association between the two proteins, we compared the membrane absorption kinetics and relative equilibrium membrane densities of three previously isolated SspB variants (nano, micro, and milli)[36] in the presence of membrane-tethered iLID (**Fig. 3.1b**). In the absence of 488 nm light, equilibrium membrane density of the high-affinity SspB(nano) variant was ≥10-fold greater than those of SspB(micro) and SspB(milli).

After allowing the SspB variants to reach equilibrium in the presence of membrane-tethered iLID, we compared their light-induced membrane recruitment. For these experiments, we used a single, 50 ms pulse of 488 nm light (~50 μW) to shift iLID into the "open" conformation and allow it to associate with SspB. In all cases, this resulted in an immediate increase in AF647-SspB membrane localization that peaked within 10 seconds of the 488 nm activating signal (**Fig. 3.1b, c**). SspB(nano) displayed the highest total membrane recruitment, SspB(micro) exhibited a modest increase in membrane intensity, and the change in the SspB(milli) signal was nearly undetectable. All three SspB variants dissociated from bilayers with exponential kinetics based on the reversion of iLID to the "closed", dark-state conformation (**Fig. 3.1b**).

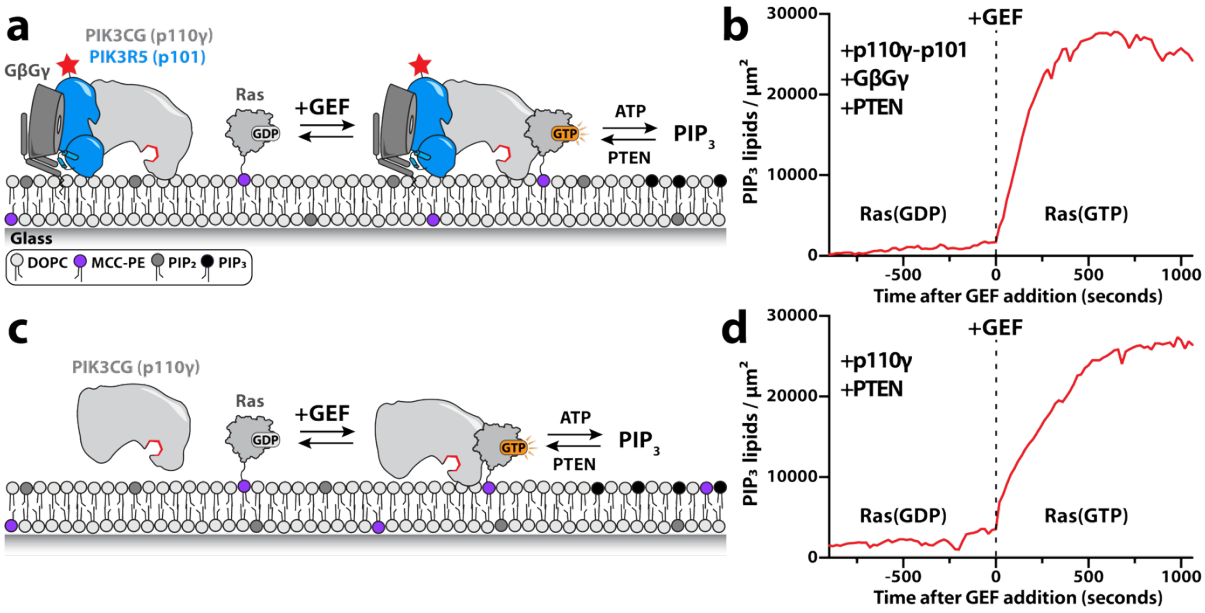

Figure 3.1 A 488 nm light pulse results in transient iLID-SspB heterodimerization on supported lipid bilayers
(a) Schematic cartoon showing his$_{10}$-mNG-iLID tethered to an SLB via a NiNTA lipid. In the dark, its binding partner, AF647-SspB, is predominantly in solution. A pulse of 488 nm light activates iLID resulting in AF647-SspB membrane recruitment. **(b)** SspB variants (nano, micro, and milli)

have distinct membrane absorption properties in the absence of 488 nm light and in response to activating light. All SspB variants exponentially dissociate from the membrane in the dark. **(c)** Representative TIRF-M images showing membrane fluorescence of iLID and AF647-SspB(micro) in the absence and presence of uniform 488 nm light. **(b, c)** Membrane composition: 94% DOPC, 2% NiNTA (+iLID bound), 2% MCC-PE, and 2% PIP_2 lipids.

SspB membrane recruitment can be spatially controlled

To mimic the polarized membrane signaling that occurs in vivo, we established an approach to spatially control the blue light-induced activation of membrane-tethered iLID on SLBs using a digital micromirror device (DMD) (**Fig. 3.2a, b**). For different 488-nm illumination patterns, we visualized the corresponding SspB(micro) membrane localization and defined the limits of our ability to detect iLID-SspB heterodimerization (**Fig. 3.2c, d** and **Supplementary Fig. 1**). For all light patterns, lateral membrane diffusion of iLID caused SspB(micro) membrane localization to expand slightly beyond the initially defined region of activation. Although the AF647-SspB signal always decayed rapidly after a light pulse, we could repeatedly activate iLID in the same membrane region without observing a decrease in SspB recruitment (**Fig. 3.2e, f**).

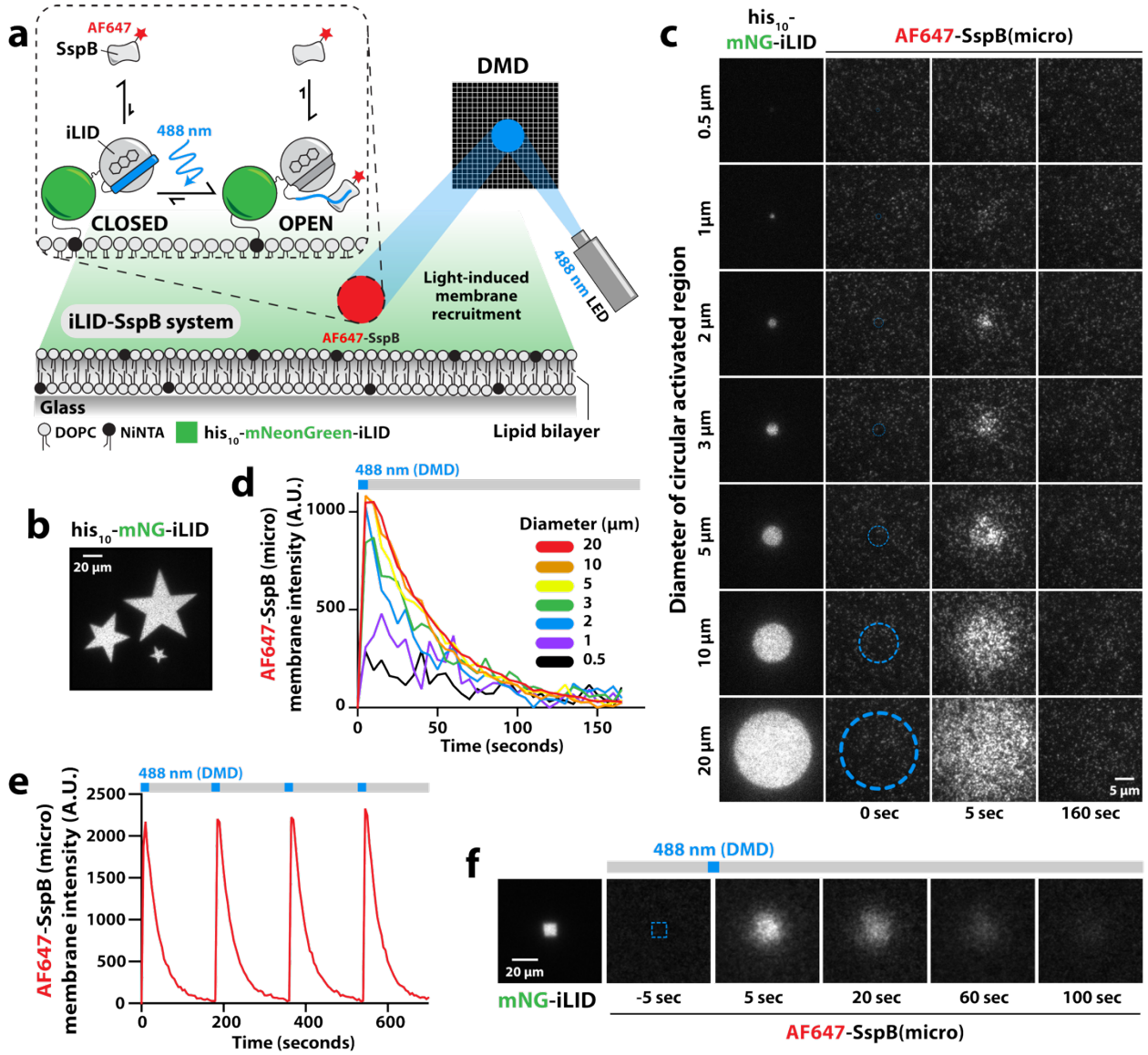

Figure 3.2 SspB membrane recruitment can be spatially controlled
(a) A digital micromirror device (DMD) can be used to spatially control the 488 nm light-induced activation of membrane-tethered iLID and recruitment of AF647-SspB. **(b)** TIRF-M image showing DMD-generated patterns of 488 nm-excited iLID. **(c)** TIRF-M images showing DMD-generated circles (20, 10, 5, 3, 2, 1, 0.5 µm in diameter) of 488 nm-excited iLID and the resulting transient AF647-SspB(micro) membrane recruitment. **(d)** Kinetic traces showing AF647-SspB(micro) membrane recruitment and dissociation measured in the activated iLID circles shown in **(c). (e)** Repeated light-dependent membrane recruitment of AF647-SspB(micro) to the same 20 µm-diameter circle. **(f)** Montage of TIRF-M images showing the time-dependent change in AF647-SspB(micro) membrane localization following DMD-guided activation of iLID. **(b, e, f)** Membrane

composition: 94% DOPC, 2% NiNTA (+iLID conjugated), 2% MCC-PE, and 2% PIP_2 lipids. **(c, d)** Membrane composition: 94% DOPC, 2% NiNTA (+iLID bound), 2% MCC-PE, and 4% PIP_2 lipids.

SspB membrane recruitment can be tuned by varying the intensity of activating light

Using spatially patterned light, we next sought to tune SspB membrane recruitment by modulating the intensity of blue light used to activate iLID. Visualization of SspB membrane recruitment as a function of blue light intensity revealed that iLID was maximally activated in the presence of light at 10% LED power (~15 μW, **Fig. 3.3a-c**). Lower levels of activating blue light resulted in less SspB membrane recruitment. To quantify the fold change in SspB membrane recruitment, we accounted for both the basal level of light-independent recruitment and the maximum light-induced membrane recruitment (**Fig. 3.3d**). SspB(nano) and SspB(micro) both displayed much larger fold changes in membrane recruitment than SspB(milli) with SspB(nano) slightly outperforming SspB(micro) across different light intensities (**Fig. 3.3e**). Comparing dissociation kinetics revealed that the dissociation half-times for SspB(nano, micro, milli) were relatively insensitive to the strength of the activating blue light although the three variants displayed different dissociation half-times that were correlated with their respective affinities (**Fig. 3.3f**).

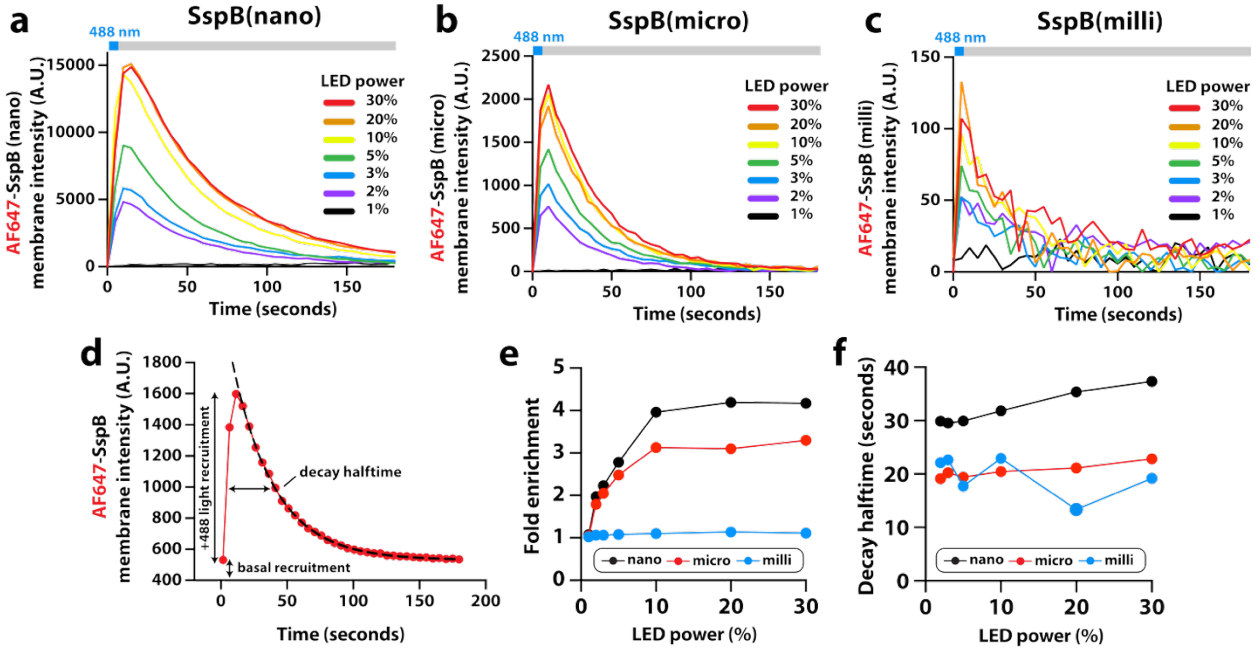

Figure 3.3 SspB membrane recruitment can be tuned by varying the intensity of activating light

(a-c) Kinetic traces showing membrane recruitment and dissociation of 50 nM AF647-SspB (nano, micro, and milli) measured using a 488 nm light pulse over a range of intensities (1-30% LED power, 0-50 μW, conversion in **Supplementary Fig. 2**). **(d)** Representative kinetic trace of AF647-SspB(micro) membrane recruitment and dissociation. Fold membrane enrichment was calculated using (basal recruitment + 488 nm light recruitment)/basal recruitment. Fitting to a non-linear one phase decay curve (dashed line) was used to calculated signal decay halftime. **(e)** Quantification of AF647-SspB(nano, micro, and milli) fold membrane enrichment as a function of LED power. **(f)** Quantification of AF647-SspB(nano, micro, and milli) signal decay halftime as a function of LED power. **(a-f)** Membrane composition: 94% DOPC, 2% NiNTA (+iLID bound), 2% MCC-PE, and 2% PIP_2 lipids.

With the goal of spatially controlling Ras activation on SLBs, we designed and purified the catalytic domain of the SOS1 (Son of Sevenless Homolog 1) RasGEF fused to SspB(nano, micro, and milli). Similar to SspB(micro) alone, we observed robust and transient recruitment of the GEF-SspB fusion proteins to membrane-tethered iLID following patterned illumination with 488 nm light (**Fig. 3.4**). The only notable difference we observed between the GEF-SspB fusions and the original SspB proteins was that

GEF-SspB(micro) exhibited larger fold changes in membrane recruitment than GEF-SspB(nano) across a range of light intensities (**Fig. 3.3e**). Based on its relatively low level of light-independent membrane recruitment and moderately large increase in light-dependent membrane localization, we determined GEF-SspB(micro) (subsequently referred to as GEF-SspB) to be the most versatile for reconstituting patterned Ras membrane activation.

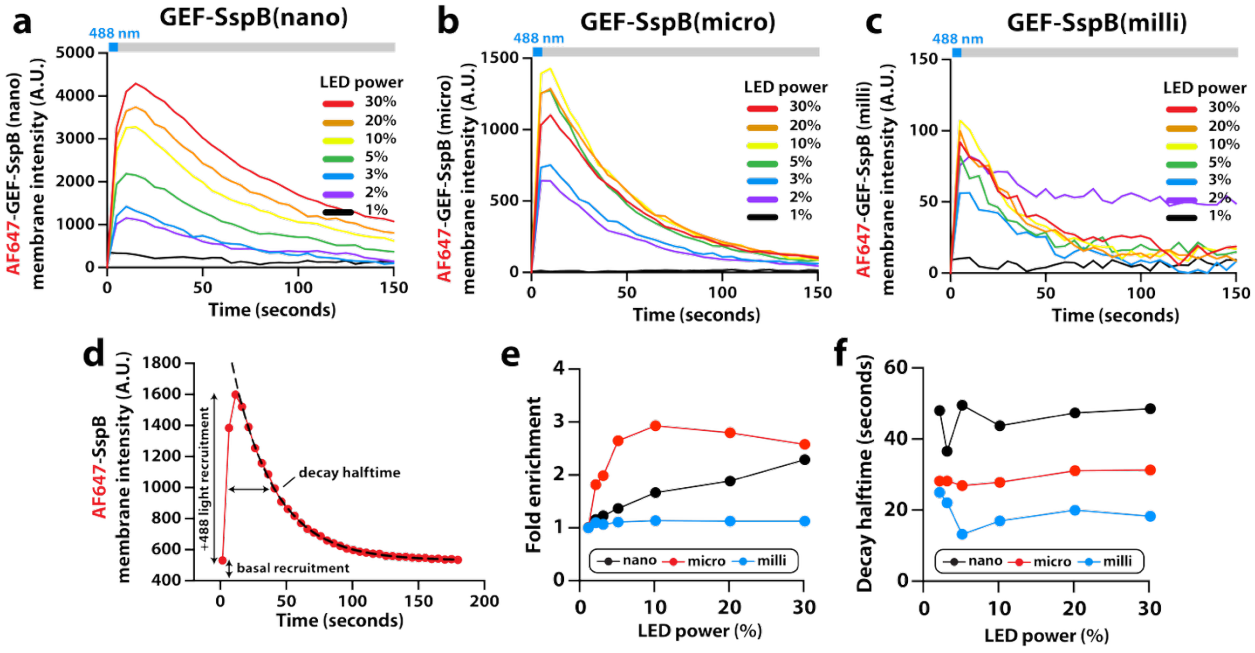

Figure 3.4 GEF-SspB membrane recruitment can be tuned by varying the intensity of activating light

(a-c) Kinetic traces showing membrane recruitment and dissociation of 50 nM AF647-GEF-SspB (nano, micro, and milli) measured using a 488 nm light pulse over a range of intensities (1-30% LED power, 0-50 μW, conversion in **Supplementary Fig. 2**). **(d)** Representative kinetic trace of AF647-SspB(micro) membrane recruitment and dissociation. Fold membrane enrichment was calculated using (basal recruitment + 488 nm light recruitment)/basal recruitment. Fitting to a non-linear one phase decay curve (dashed line) was used to calculated signal decay halftime. **(e)** Quantification of AF647-GEF-SspB(nano, micro, and milli) fold membrane enrichment as a function of LED power. **(f)** Quantification of AF647-GEF-SspB(nano, micro, and milli) signal decay halftime as a function of LED power. **(a-c, e, f)** Membrane composition: 98% DOPC lipids and 2% NiNTA lipids (+iLID bound).

Membrane-tethered Ras can be locally and transiently activated with light

GTPases are toggled between their active, GTP-bound state and their inactive, GDP-bound state by GEFs and GAPs, respectively (**Fig. 1.1**). To measure the kinetics of GAP- and GEF-mediated regulation of membrane-conjugated Ras, we visualized the change in membrane localization of a fluorescently labeled RBD (Ras(GTP) binding domain) derived from c-Raf kinase (**Fig. 3.5a**). We conjugated purified H-Ras to SLBs in a physiologically relevant orientation using maleimide lipids, as previously described[33]. To mimic the dynamic rise and fall in Ras activity that is commonly observed in cell signaling, we established conditions to trigger the transient light-induced activation of Ras in the context of negative regulation imposed by the soluble RasGAP NF1 (Neurofibromatosis type 1, subsequently referred to as GAP) (**Fig. 3.5b**). Immediately following light-induced membrane recruitment of GEF-SspB, we detected a local increase in AF546-RBD (i.e. active Ras) fluorescence intensity, indicating that we were successful in spatially controlling Ras activation (**Fig. 3.5c, d**). This local Ras(GTP) signal decayed back to baseline following membrane dissociation of GEF-SspB and GAP-mediated GTP hydrolysis (**Fig. 3.5b-d**). The timescale of Ras activation and deactivation was comparable to signaling dynamics observed in cells[127].

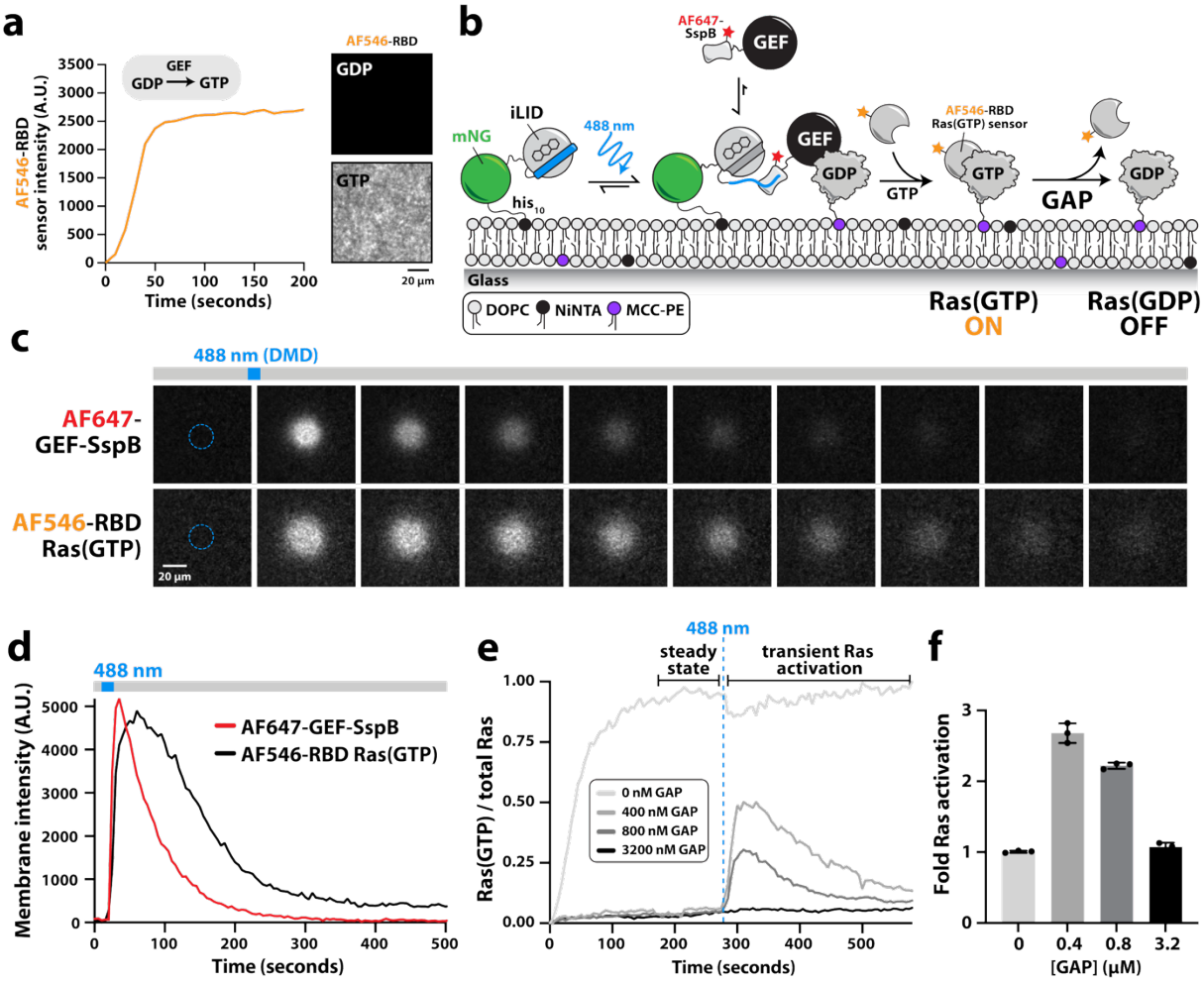

Figure 3.5 Membrane-tethered Ras can be locally and transiently activated with light
(a) Kinetics of membrane-anchored Ras activation in the presence of GEF and no GAP. Ras activation was monitored with 50 nM AF546-labeled Ras binding domain (RBD). Representative images show bulk membrane localization and specificity of AF546-RBD on bilayers with inactive Ras(GDP) and active Ras(GTP). **(b)** Cartoon schematic showing how light-induced activation of iLID drives membrane recruitment of AF647-GEF-SspB to locally activate membrane-anchored Ras. Global GAP regulation reverses light-mediated activation of Ras. **(c)** Representative TIRF-M montages showing the time-dependent change in AF647-GEF-SspB(micro) membrane localization and Ras activation following local iLID activation with patterned 488 nm light (dashed blue circle). Images are separated by 25 seconds. **(d)** Kinetic traces showing membrane recruitment and dissociation of AF647-GEF-SspB(micro) and AF546-RBD following a 50 ms 488 nm light pulse. **(e)** Varying GAP concentrations (0-3200 nM) modulate the initial steady-state fraction of activated Ras and response to local light-induced activation by GEF-SspB(micro). **(f)** Quantification of the light-induced fold increase in Ras(GTP) as a function of global GAP concentration in **(e)**. Fold activation was calculated using (steady-state light-independent Ras activation + peak 488 nm light dependent activation)/steady-state light-independent activation.

Data are presented as mean values +/- standard deviation, n = 3. Membrane composition: **(c-f)** 92% DOPC, 2% NiNTA (+iLID bound), 2% MCC-PE (+Ras bound), and 4% PIP_2 lipids. Membrane in **(a)** lacks NiNTA lipids. For all reactions, GEF refers to the catalytic domain of SOS1. 30% LED power was used for all activating light pulses.

In vivo, the total RasGAP concentration can range from approximately 50 to 200 nM[128,129]. However, these regulatory molecules are structurally variable and exist within complex regulatory networks making it difficult to estimate the total cellular concentration of "active" RasGAP. To determine the relationship between GAP concentration and steady-state Ras(GTP) levels, we tested our light-inducible Ras activation system over a range of GAP concentrations (**Fig. 3.5e, f**). For these experiments, we allowed reactions containing membrane-tethered Ras and GEF-SspB to reach an initial steady state of Ras activation in the presence of global GAP-mediated negative regulation. Then, we used a transient pulse of 488 nm light guided by the DMD to drive membrane recruitment of GEF-SspB. We quantified the corresponding fold change in Ras(GTP) on membranes (**Fig. 3.5e, f**). In the absence of GAP, we observed no light-induced Ras activation since all the available Ras molecules were already GTP-bound due to unopposed global GEF activity. Conversely, when GAP was present at the high concentration of 3.2 μM, most Ras molecules remained GDP-bound and the change in Ras activation upon illumination was undetectable. In the intermediate GAP concentration range of 400-800 nM we measured robust increases in Ras(GTP) following light-induced activation with GEF-SspB. These Ras(GTP) signals decayed back to the baseline in minutes. We used GAP concentrations between 400 and 810 nM for all the optogenetic experiments described in Chapter Four. By combining transient, light-mediated Ras activation and global GAP regulation, we

developed a unique in vitro reconstitution that resembles the spatiotemporal dynamics of Ras activation in vivo.

DISCUSSION

This work establishes a new technique for reconstituting membrane signaling reactions. We devised an approach by which we can observe unique steady-state conditions of membrane-anchored Ras GTPase in the presence of both positive and negative regulators. By suppressing spurious activation of Ras through global, GAP-mediated negative regulation we mimic a cellular state prior to receptor agonist-induced pathway activation. We then utilize transient, light-induced membrane recruitment of a RasGEF via the iLID-SspB system to trigger the activation of Ras GTPase in a spatially controlled manner.

Cells establish precise, system-level steady-state signaling conditions by balancing complex networks of positive and negative regulators. The total concentrations of cell surface receptors, small GTPases, GEFs, GAPs, lipid kinases, and lipid phosphatases vary between cell types, creating unique thresholds for activation, rates of signal amplification, and cellular outcomes[130]. The total cellular concentration of RasGAPs and RasGEFs can range from 50 to 200 nM[128,129]. However, the system-level concentrations and activities of GAPs and GEFs are difficult to estimate due to our incomplete understanding of their regulatory mechanisms (e.g. autoinhibition). This makes it challenging to approximate biologically relevant strengths of global Ras activation and inhibition. In our assay, we use a single GAP (NF1) at concentrations

between 400 and 800 nM which we experimentally determined to be sufficient to suppress most GEF-mediated Ras activation. This global, GAP-driven negative regulation stands in for the intricate, system-level Ras regulatory modules that exist across cell types. Importantly, the light-based signaling inputs and corresponding responses occur on a biologically relevant time scale (i.e. seconds to minutes)[127].

Light-inducible heterodimerization offers opportunities for spatiotemporally controlling the localization and activation of a wide range of biological molecules in vitro. Similar techniques have been used in vivo for diverse purposes including activating RhoA, Cdc42, and Rac1 GTPases[124,131,132] and modulating the localization of PIP lipid kinases[125], mitotic spindle apparatus proteins[133], myosin phosphatases[134], actin nucleation promoting factors[135], and entire organelles[136]. A recent study demonstrated that light-inducible recruitment of an actin nucleation promoting factor could be used to control the assembly of branched actin networks in vitro on SLBs[135]. Allowing for fast, reversible, and spatially localized perturbations, light-inducible dimerization systems represent a powerful tool for future biochemical reconstitutions.

METHODS

Protein expression, purification, and labeling

H-Ras and GEF were purified as described in Chapter Two.

mNeonGreen-iLID. A gene sequence encoding iLID was expressed in Rosetta 2 pLysS *E. coli* as a his_{10}-mNG-iLID fusion protein. Bacteria were grown at 37°C in Terrific Broth to an absorbance of 0.8 at 600 nm. Cultures were shifted to 18°C for 1 hour then

induced with 0.05 mM IPTG. Expression was allowed to continue for 22 hours before harvesting. Cells were lysed by sonication in buffer containing 50 mM Na_2HPO_4 [pH 8.0], 400 mM NaCl, 0.4 mM βME, 1 mM PMSF, 100 µg/ml DNase. Lysate was centrifuged at 15,000 rpm (35000 x g) for 60 minutes in a Beckman JA-20 rotor at 4ºC. Lysate was circulated over a 5 ml HiTrap chelating column (Cytiva, Cat# GE17-0409-01) charged with 100 mM $CoCl_2$ for 10-15 minutes. Column was washed with 50 mM Na_2HPO_4 [pH 8.0], 400 mM NaCl, 10 mM imidazole, 0.4 mM βME. Bound protein was eluted in 50 mM Na_2HPO_4 [pH 8.0], 400 mM NaCl, 500 mM imidazole, 0.4 mM βME. Peak fractions were pooled and dialyzed against 4 liters of buffer containing 25 mM Na_2HPO_4 [pH 8.0], 400 mM NaCl, 500 mM imidazole, 0.4 mM βME. Dialysate was recirculated over a 5 ml HiTrap chelating column and concentrated in a 5 kDa MWCO Vivaspin 20 concentrator to a volume of 5 ml before loading onto a 124 ml Superdex 75 column equilibrated in 20 mM HEPES [pH 7.0], 200 mM NaCl, 10% glycerol, 1 mM TCEP. Peak fractions were pooled, concentrated to a minimum concentration of 200 µM, and snap frozen in liquid nitrogen for storage at -80ºC. The his_{10} tag caused the his_{10}-mNG-iLID protein aggregate after long-term storage in the -80ºC. Before performing SLB experiments, we removed aggregated his_{10}-mNG-iLID by size exclusion chromatography (i.e. Superdex 75).

SspB(milli, micro, nano). Genes encoding SspB affinity variants were expressed as his_{10}-SUMO3-KCK-SpyCatcher-SspB fusion proteins in Rosetta 2 pLysS *E. coli*. Note that the SpyCatcher was simply used as a generic place holder fusion protein. It was not combined with SpyTag in this study. Bacteria were grown at 37°C in Terrific Broth to an

absorbance of 0.8 at 600 nm. Cultures were then shifted to 18°C for 1 hour before inducing with 0.05 mM IPTG. Expression was allowed to continue for 22 hours before harvesting. Cells were lysed in 50 mM Na_2HPO_4 [pH 8.0], 400 mM NaCl, 0.4 mM βME, 1 mM PMSF, 100 µg/ml DNase by sonication. Lysate was centrifuged at 15,000 rpm (35000 x g) for 60 minutes in an Avanti JA-17 rotor at 4ºC. Lysate was circulated over a 5 ml HiTrap chelating column (Cytiva, Cat# GE17-0409-01) charged with 100 mM $CoCl_2$ for ten minutes. Column was washed with 50 mM Na_2HPO_4 [pH 8.0], 400 mM NaCl, 10 mM imidazole, 0.4 mM βME. Bound protein was eluted in 50 mM Na_2HPO_4 [pH 8.0], 400 mM NaCl, 500 mM imidazole, 0.4 mM βME. Peak fractions were pooled and his_6-SenP2 (SUMO protease) was added to cleave off the his_{10}-SUMO3 tag. The solution was dialyzed overnight against 4 liters of buffer containing 20 mM HEPES [pH 7.0], 200 mM NaCl, 10% glycerol, 0.4 mM βME. Dialysate was concentrated in a 5 kDa MWCO Vivaspin 20 concentrator to a volume of 5 ml before loading onto a 124 ml Superdex 75 column equilibrated in 20 mM HEPES [pH 7.0], 200 mM NaCl, 10% glycerol, 1 mM TCEP. Peak fractions were pooled and snap frozen in liquid nitrogen for storage at -80ºC.

GEF-SspB(milli, micro, nano). Gene sequences encoding his_{10}-SUMO3-KCK-SosCat(564-1049aa)-SspB were expressed in Rosetta 2 pLysS *E. coli* to generate chimeric light-regulatable GEFs. Bacteria were grown at 37°C in Terrific Broth to an absorbance of 0.8 at 600 nm. Cultures were shifted to 18°C for 1 hour then induced with 0.05 mM IPTG. Expression was allowed to continue for 22 hours before harvesting. Cells were lysed in 50 mM Na_2HPO_4 [pH 8.0], 400 mM NaCl, 0.4 mM βME, 1 mM PMSF, 100

μg/ml DNase by sonication. Lysate was centrifuged at 15,000 rpm (35000 x g) for 60 minutes in a Beckman JA-20 rotor at 4ºC. Lysate was circulated over a 5 ml HiTrap chelating column (Cytiva GE17-0409-01) inoculated with 100mM $CoCl_2$ for ten minutes. Column was washed with 50 mM Na_2HPO_4 [pH 8.0], 400 mM NaCl, 10 mM imidazole, 0.4 mM βME. Bound protein was eluted in 50 mM Na_2HPO_4 [pH 8.0], 400 mM NaCl, 500 mM imidazole, 0.4 mM βME. Peak fractions were pooled and SenP2 protease was added to cleave off the his_{10}-SUMO3 tag. The solution was dialyzed overnight against 4 liters of buffer containing 25 mM Na_2HPO_4 [pH 8.0], 400 mM NaCl, 500 mM imidazole, 0.4 mM βME. Dialysate was recirculated over a 5 ml HiTrap chelating column and concentrated in a 5 kDa MWCO Vivaspin 20 concentrator to a volume of 5 ml before loading onto a 124 ml Superdex 75 column equilibrated in 20 mM HEPES [pH 7.0], 200 mM NaCl, 10% glycerol, 1 mM TCEP. Peak fractions were pooled, concentrated to a minimum concentration of 200 μM, and snap frozen in liquid nitrogen for storage at -80ºC.

AF546-SNAP-RBD and AF647-SNAP-RBD. A gene sequence encoding the Ras(GTP) binding domain (RBD) derived from human cRaf kinase was expressed in Rosetta 2 pLysS *E. coli* cells as a his_6-GST-PP-SNAP-GSGSGS-RBD (Raf1, K65E) fusion protein as previously described[137]. Bacteria were grown at 37°C in Terrific Broth to an absorbance of 0.8 at 600 nm. Cultures were shifted to 18°C for 1 hour then induced with 0.5 mM IPTG. Expression was allowed to continue for 22 hours before harvesting. Cells were lysed in 50 mM Na_2HPO_4 [pH 8.0], 400 mM NaCl, 0.4 mM BME, 1 mM PMSF, 100 μg/mL DNase, 1 mg/mL lysozyme by sonication. Lysate was centrifuged at 15,000

rpm (35000 x g) for 60 minutes in a Beckman JA-20 rotor at 4ºC. Lysate was circulated over a 5 mL HiTrap chelating column (Cytiva, Cat# GE17-0409-01) charged with 100mM $CoCl_2$ for ten minutes. Column was washed with 50 mM Na_2HPO_4 [pH 8.0], 400 mM NaCl, 10 mM imidazole, 0.4 mM BME. Bound protein was eluted in 50 mM Na_2HPO_4 [pH 8.0], 400 mM NaCl, 500 mM imidazole, 0.4 mM βME. Peak fractions were pooled and the his_6-GST tag was cleaved off with PreScission protease (derived from human rhinovirus 3C protease), while dialyzing into buffer containing 20 mM HEPES [pH 7.5], 400 mM NaCl, 5% glycerol, 0.4 mM βME. Dialysate containing cleaved protein was recirculated over a 5 mL HiTrap chelating column. Flowthrough was concentrated in a 5 kDa MWCO Vivaspin 20 concentrator to a volume of 5 mL before loading onto a 124 mL Superdex 75 column equilibrated in 20mM HEPES [pH 7.0], 200 mM NaCl, 10% glycerol, 1 mM TCEP. Peak fractions were pooled and snap frozen in liquid nitrogen for storage at -80ºC.

Purified SNAP-RBD was labeled with 1.5x molar excess of SNAP-Surface Alexa546 dye (NEB, Cat# S9132S) or SNAP-Surface Alexa647 dye (NEB, Cat# S9136S) overnight at 4ºC in buffer containing 20 mM Tris [pH 8.0], 200 mM NaCl, 1 mM TCEP. The next day, the labeled protein was loaded onto a PD10 desalting column equilibrated in buffer containing 20 mM Tris [pH 8.0], 200 mM NaCl, 10% glycerol, 1 mM TCEP to remove most of the free SNAP dye. It was then concentrated in an Amicon-Ultra concentrator and loaded onto a Superdex 75 column equilibrated in 20 mM Tris [pH 8.0], 200 mM NaCl, 10% glycerol, 1 mM TCEP. Unreacted SNAP dye and labeled protein were

separated by size exclusion chromatography. The peak fractions were pooled, concentrated, aliquoted, and snap frozen in liquid nitrogen for storage at -80ºC.

GAP. The RasGAP domain derived from NF1 (Neurofibromatosis type 1) was expressed in Rosetta 2 pLysS *E. coli* as a his_6-MBP-TEV-NF1(1-333aa) fusion. Bacteria were grown at 37°C in Terrific Broth to an absorbance of 0.8 at 600 nm. Cultures were shifted to 18°C for 1 hour then induced with 0.5 mM IPTG. Expression was allowed to continue for 22 hours before harvesting. Cells were lysed in 50 mM Na_2HPO_4 [pH 8.0], 400 mM NaCl, 0.4 mM βME, 1 mM PMSF, 100 µg/mL DNase, 1 mg/mL lysozyme by sonication. Lysate was centrifuged at 15,000 rpm (35000 x g) for 60 minutes in a Beckman JA-20 rotor at 4ºC. Lysate was circulated over a 5 mL HiTrap chelating column (Cytiva, Cat# GE17-0409-01) charged with 100 mM $CoCl_2$ for ten minutes. Column was washed with 50 mM Na_2HPO_4 [pH 8.0], 400 mM NaCl, 10 mM imidazole, 0.4 mM βME. Bound protein was eluted in 50 mM Na_2HPO_4 [pH 8.0], 400 mM NaCl, 500 mM imidazole, 0.4 mM βME. Peak fractions containing the eluted protein were pooled, mixed with TEV protease, and dialyzed against buffer containing 25 mM Na_2HPO_4 [pH 8.0], 400 mM NaCl, 0.4 mM βME at 4ºC overnight. The next day, dialysate was recirculated over a 5 mL HiTrap chelating column to capture the his_6-MBP-TEV tag. The flow through containing NF1(1-333aa) was concentrated in a 5 kDa MWCO Vivaspin 20 concentrator and loaded onto a Superdex 75 column equilibrated in buffer containing 20 mM HEPES [pH 7], 200 mM NaCl, 10% glycerol, 1 mM TCEP. Peak fractions containing monodispersed NF1

were pooled, concentrated to 250 µM, and snap frozen in liquid nitrogen prior to storage at -80ºC.

Supported lipid bilayer experiments

Preparation of supported lipid bilayers. The following lipids were used to generate Small Unilamellar Vesicles (SUVs) and subsequently supported lipid bilayers: 1,2-dioleoyl-sn-glycero- 3-phosphocholine (18:1 DOPC, Avanti #850375C), L-α-phosphatidylinositol-4,5-bisphosphate (Brain PIP_2, Avanti #840046X), 1,2-dioleoyl-sn-glycero-3-phosphoethanolamine-N-[4-(p-maleimidomethyl) cyclohexane-carboxamide] (18:1 MCC-PE, Avanti #780201C), and 1,2-dioleoyl-sn-glycero-3-[(N-(5-amino-1-carboxypentyl)iminodiacetic acid)succinyl] (18:1 DGS-NTA(Ni), Avanti #790404C). To prepare SUVs, a total of 2 µmoles of lipids were combined in a 35 ml glass round bottom flask containing ~2 ml chloroform.

Lipids were dried to a thin film using rotary evaporation with the glass round-bottom flask submerged in a 42ºC water bath. The lipid film was then resuspended in 2 ml filtered PBS [pH 7.4] (Corning, cat# 46-013-CM), bringing the lipid suspension to a final concentration of 1 mM. All lipid mixtures expressed as percentages (e.g. 98% DOPC, 2% PIP_2) are equivalent to molar fractions. To generate 50 nm SUVs, the 1 mM lipid mixture was extruded through a 0.05 µm pore size 19 mm polycarbonate (PC) membrane (Cytiva Whatman, Cat# 800308) with filter supports (Cytiva Whatman, Cat# 230300) on both sides of the PC membrane.

To create supported lipid bilayers, coverglass (25x75 mm, IBIDI, Cat #10812) was initially cleaned with 2% Hellmanex III (Fisher, Cat #14-385-864) that was heated to 60-70ºC in a glass coplin jar and incubated for at least 30 minutes. After rinsing the Hellmanex-cleaned glass with MilliQ water, the coverglass was etched with Piranha solution (1:3, hydrogen peroxide:sulfuric acid) for 10-15 minutes. Etched coverglass that was rinsed and stored in MilliQ water, was removed from the Coplin jar and rapidly dried with nitrogen gas before adhering to a 6-well, sticky-side chamber (IBIDI, Cat #80608). To create a supported lipid bilayer, a total lipid concentration of 0.25 mM SUVs in PBS [pH 7.4] was flowed into the IBIDI chamber. After 30 minutes of incubation, supported membranes were washed with 5 ml PBS [pH 7.4] to remove non-absorbed SUVs. Membrane defects were then blocked for ~5 minutes with 1 mg/ml β-casein (ThermoFisher, Cat #37528) diluted in PBS [pH 7.4]. To reduce the fraction of immobile proteins on SLBs, the 10 mg/ml β-casein solution was centrifuged in a TLA120.2 at 100,000 rpm (434,513 x *g*) for 30 minutes at 4ºC using an Optima MAX-TL ultracentrifuge. After blocking bilayers with β-casein, membranes were washed again with 1 ml PBS [pH 7.4] and 1 ml PBS [pH 7.4], 1 mM $MgCl_2$, 100 μM GDP, 0.1 mM TCEP prior to H-Ras conjugation. Prior to imaging, supported membranes were washed with TIRF-M imaging buffer.

Membrane conjugation. For experiments involving membrane conjugated H-Ras, β-casein-blocked supported lipid bilayers containing MCC-PE lipids were incubated for 2 hours with 30-35 μM H-Ras at 23ºC in buffer containing PBS [pH 7.4], 1 mM $MgCl_2$,

100 μM GDP, 0.1 mM TCEP. Bilayers were quenched in PBS [pH 7.4], 5 mM βME for 10 minutes before washing with PBS [pH 7.4], 1 mM $MgCl_2$, 100 μM GDP, 0.1 mM TCEP. The resulting Ras membrane density ranged from 1000-2000 molecules/μm^2 as previously described[33].

For experiments involving iLID, bilayers containing NiNTA lipids were incubated with 20-50 nM his_{10}-mNG-iLID for 20 minutes at 23ºC. Unbound his_{10}-mNG-iLID was flushed out of the chamber with TIRF-M imaging buffer.

TIRF microscopy imaging buffer. All supported lipid bilayer TIRF-M experiments were performed in 200 μl reaction volumes using the following reaction buffer: 20 mM HEPES [pH 7.0], 150 mM NaCl, 1 mM ATP (Sigma, Cat #A2383-10G), 100 μM GTP, 5 mM $MgCl_2$, 0.5 mM EGTA, 20 mM glucose, 200 μg/ml β-casein (ThermoScientific, Cat #37528), 20 mM βME, 320 μg/ml glucose oxidase (Serva, Cat #22780.01 *Aspergillus niger*), 50 μg/ml catalase (Sigma, Cat #C40-100MG Bovine Liver), and 2 mM Trolox (Cayman Chemicals, Cat #10011659). Perishable reagents (i.e. glucose oxidase, catalase, and Trolox) were added 5-10 minutes before initiating biochemical reconstitutions on SLBs and acquiring images. All reactions in this study were reconstituted and visualized on a TIRF microscope at 23ºC.

Microscope hardware and imaging acquisition. Imaging experiments were performed using an inverted Nikon Ti2 microscope using either a 60x (1.49 NA) or 100x (1.49 NA) oil immersion Nikon TIRF objective. The x-axis and y-axis positions were controlled using a Nikon motorized stage, joystick, and NIS element software.

Fluorescently labeled proteins were excited with either a 488, 561, or 637 nm OBIS laser diode (Coherent Inc. Santa Clara, CA) controlled with a Vortran laser launch (Sacramento, CA) and acousto-optic tuneable filters (AOTF) control. Excitation and emission light was transmitted through a multi-bandpass quad filter cube (C-TIRF ULTRA HI S/N QUAD 405/488/561/638; Semrock) containing a dichroic mirror. For bulk excitation of fluorescent biosensors, laser power measured through a 60x TIRF objective ranged from 0.5-2 mW. Fluorescence emission was detected on an iXion Life 897 EMCCD camera (Andor Technology Ltd., UK) after passing through a Nikon Ti2 emission filter wheel containing the following 25 mm emission filters: ET525/50M, ET600/50M, ET700/75M (Semrock). All experiments were performed at room temperature (23ºC). Microscope hardware was controlled with Nikon NIS elements.

Spatially patterned light. A Mightex Polygon400 digital micromirror device (DMD) controlled by NIS elements was used for patterned illumination. For activation of membrane bound iLID, excitation light from a SOLA SE light engine (Lumencor, 380-680 nm range of wavelengths) was filtered using a Chroma 488 nm long-pass dichroic mirror (25.5 x 36 x 2 mm; Cat #ZT488rdc-UF2). The dichroic mirror was mounted at 45º angle in a Nikon Ti2 LAPP (Cat #Ti2-LA-BM-E) prior to entering the microscope filter turret. This setup reflects iLID activating light from the Polygon400 DMD to the sample. The 488LP dichroic allowed transmission of 561 nm and 647 nm laser excitation light to image fluorescently labeled SspB, GEFs, and activity biosensors following activation of iLID. Following repetitive illumination of the same membrane region with 488 nm light, we

observed a very slight increase in light-independent basal SspB recruitment. This potentially represents an accumulation of iLID protein that does not transition back to its "closed", dark-state conformation. For this reason, we changed the field of view between light-induced activation steps in the same reaction chamber for subsequent experiments.

Data analysis

Fold enrichment and fold activation. To calculate the fold membrane enrichment of SspB fusion proteins (**Fig. 3.3e** and **Fig. 3.4e**) we took into account both the basal level of light-independent recruitment and the maximum light-induced membrane recruitment, as previously described[138]. Fold membrane enrichment of AF647-SspB fusion proteins was calculated using (basal light-independent recruitment + peak 488 nm light dependent recruitment)/basal light-independent recruitment. The same equation was used to calculate fold Ras activation in **Fig. 3.5e, f**: (steady-state light-independent Ras activation + peak 488 nm light dependent activation)/steady-state light-independent activation.

Decay halftime. To calculate the decay halftime of the AF647-SspB membrane signal (**Fig. 3.3f** and **Fig. 3.4f**), kinetic traces were fit to a non-linear one phase decay curve using Prism GraphPad 10: Y = (Y0 - Plateau)*exp(-K*X) + Plateau where Y0 is the Y value at time 0, Plateau is the Y value at infinite times, and K is the rate constant, expressed in reciprocal of the X axis time units.

BRIDGE TO CHAPTER FOUR

In Chapter Three, we described the development of an in vitro light-inducible experimental system that mimics transient, spatially patterned Ras activation downstream

of cell surface receptors. In Chapter Two, we established Ras(GTP) as an important activator of PI3Kγ, which produces PIP_3 at the plasma membrane. In Chapter Four, we reconstitute communication between light-inducible Ras activation and PI3Kγ lipid kinase activity. We introduce positive feedback circuitry to this signaling module and observe spatiotemporal amplification of Ras activation and PIP_3 generation.

CHAPTER FOUR

POSITIVE FEEDBACK DRIVES THE SPATIOTEMPORAL AMPLIFICATION OF RAS ACTIVATION AND PIP_3 GENERATION IN VITRO

*This chapter contains previously published co-authored material.

Doerr, S., Olavarrieta-Colasurdo, A. & Hansen, S. D. Reconstitution of Ras-PI3Kγ membrane communication and feedback using light-induced signaling inputs. *BioRxiv* (2026).

The following experiments were designed and performed by Dr. Scott Hansen and Sophia Doerr.

INTRODUCTION

Together, phosphatidylinositol phosphate (PIP) lipids and small GTPases function downstream of plasma membrane receptors to govern essential cellular processes like growth, trafficking, and cytoskeletal reorganization. The abundance and spatial distribution of PIP lipids and activated small GTPases are controlled by an interconnected network of positive and negative feedback loops[13,15,23,139]. Positive feedback in plasma membrane-associated signaling events functions to amplify external signals and break spatial symmetry through the rapid generation of molecular concentration gradients within cells[24,140,141]. It is challenging to decipher how specific feedback circuits control the spatiotemporal dynamics of individual signaling modules in vivo due to redundancy and crosstalk within signaling networks. To understand feedback circuitry in signal processing,

a bottom-up reductionist biochemistry approach is necessary to complement a large body of existing cell biology research.

In Chapter Two, we reconstituted Ras(GTP)-dependent PI3Kγ activation in the presence of GβGγ and PTEN (Phosphatase and Tensin Homolog). In Chapter Three, we developed a method to control the spatial and temporal activation of membrane-anchored Ras using the iLID-SspB system. Here, we establish communication between light-inducible Ras activation and PI3Kγ lipid kinase activity on Supported Lipid Bilayers (SLBs) and visualize the spatiotemporal evolution of this signaling module by TIRF-M (Total Internal Reflection Fluorescence Microscopy). To investigate the impact of feedback on Ras and PIP_3 signaling reactions, we introduce positive feedback loops mediated by GEFs (Guanine Nucleotide Exchange Factors) to our light-inducible system and determine conditions under which the reconstituted Ras-PI3Kγ module overcomes negative regulation imposed by a GAP (GTPase Activating Protein) and PTEN. We demonstrate how positive feedback results in the spatiotemporal amplification of both Ras activation and PI3Kγ-dependent PIP_3 production and show that the dynamics of the resulting activity wave depend on feedback loop architecture and the membrane diffusivity of the constituent molecules. This work establishes a novel assay for systematically studying how positive feedback enables membrane signaling reactions to outpace global negative regulation and drive spatial patterning programs. Deciphering how the activation of small GTPases and the interconversion of PIP lipids function in

concert provides insight into the mechanisms that govern signal transduction across cell types.

RESULTS

A chimeric GEF mediates a positive feedback loop

In cells, GEFs bind activated GTPases or downstream products to generate recruitment-based feedback loops that amplify membrane signaling reactions[13,26,27,107]. We hypothesized that GEF-mediated positive feedback would alter the spatiotemporal dynamics of light-inducible Ras activation in our reconstituted system. To test this, we designed a simple feedback circuit that relies on a minimal RasGEF catalytic domain derived from SOS1 (Son of Sevenless Homolog 1) fused to a Ras(GTP) binding domain (RBD) (**Fig. 4.1a**). This chimeric GEF, which we refer to as $GEF_{Ras(GTP)}$, binds with high specificity to Ras(GTP). Although SOS1 naturally exhibits positive feedback based on differential Ras binding to its catalytic and allosteric binding sites, our engineered GEF allowed us to bypass complexity associated with SOS1 autoinhibition mediated by an N-terminal Dbl homology domain[112]. To assess the feedback potential of this chimeric GEF, we compared Ras nucleotide exchange in the presence of 4 nM $GEF_{Ras(GTP)}$, SOS1 HDPC (Histone, Dbl Homology, Pleckstrin Homology, and Catalytic domains of SOS1), and GEF (SOS1 catalytic domain alone) on SLBs in the absence of GAP (**Fig. 4.1b**). $GEF_{Ras(GTP)}$ activity resulted in rapid, sigmoidal Ras activation consistent with strong recruitment-based positive feedback whereas GEF activity resulted in slower, more hyperbolic Ras activation and SOS1 HDPC produced an intermediate kinetic trace.

Moreover, in the presence of GAP and high $GEF_{Ras(GTP)}$ concentrations (>30 nM), we observed the spontaneous formation of bistable patterns of Ras(GDP) and Ras(GTP) on supported membranes (**Fig. 4.1c**). These patterns were reminiscent of previously reported PIP lipid compositional patterns that arise due to competing lipid kinases and phosphatases that exhibit positive feedback based on product binding[30]. Depending on the balance of GAP and GEF activity, we could shift the bistable system to steady-state conditions that either eliminated Ras(GTP) or caused Ras to be activated across the entire bilayer. The kinetics of Ras activation and the spontaneous symmetry breaking observed in the presence of $GEF_{Ras(GTP)}$ indicate that were successful in introducing GEF-mediated positive feedback to our reconstitution.

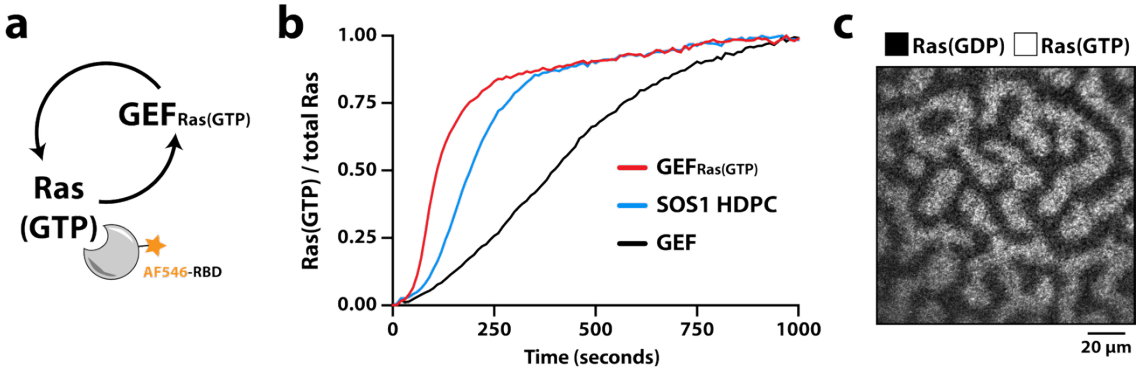

Figure 4.1 A chimeric GEF mediates a positive feedback loop
(a) $GEF_{Ras(GTP)}$ is recruited by molecules of Ras(GTP) which allows it to activate additional Ras molecules. Ras(GTP) can be visualized via an AF546-RBD biosensor. **(b)** Rapid, sigmoidal Ras activation in the presence of 4 nM $GEF_{Ras(GTP)}$ and slower, more hyperbolic Ras activation in the presence of 4 nM GEF. 4 nM SOS1 HDPC results in intermediate Ras activation kinetics. **(c)** Representative TIRF-M image showing Ras(GTP) (AF647-RBD) patterns spontaneously formed in the presence of 30 nM $GEF_{Ras(GTP)}$ and 600 nM GAP in the absence of 488 nm activating light. **(b, c)** Membrane composition: 92% DOPC, 2% NiNTA, 2% MCC-PE (+Ras bound), and 4% PIP_2 lipids.

Light-inducible Ras feedback circuit requires a threshold density of activated Ras molecules to exhibit amplification

Membrane signaling reactions often require a threshold concentration of activator to overcome global negative regulation[142–145]. To determine the requirements to amplify and persistently outpace GAP-mediated regulation following local production of Ras(GTP), we varied the intensity of activating light to recruit a range of GEF-SspB (i.e. initiator) membrane densities (**Fig. 4.2**). These experiments were performed under steady-state conditions that eliminated spontaneous Ras(GTP) pattern formation through GAP activity. Following a low, 2.2-fold membrane enrichment of GEF-SspB, we found that $GEF_{Ras(GTP)}$ was unable amplify local Ras(GTP) enough to overcome GAP-mediated negative regulation. Instead, the local Ras(GTP) signal rapidly disappeared. Repetitive local stimulation with low-intensity light was similarly unable to trigger the Ras(GTP) amplification (**Supplementary Fig. 3**). By contrast, when GEF-SspB membrane enrichment was greater than 3.7-fold, the Ras(GTP) signal not only persisted long after GEF-SspB dissociated but also resulted in the expansion of the fluorescent region across the bilayer (**Fig. 4.2**). Based on this experiment, we determined that this self-propagating system requires a threshold Ras(GTP) density of ~35% (~350 out of ~1000 total molecules/μm^2) to overcome global inhibition and amplify.

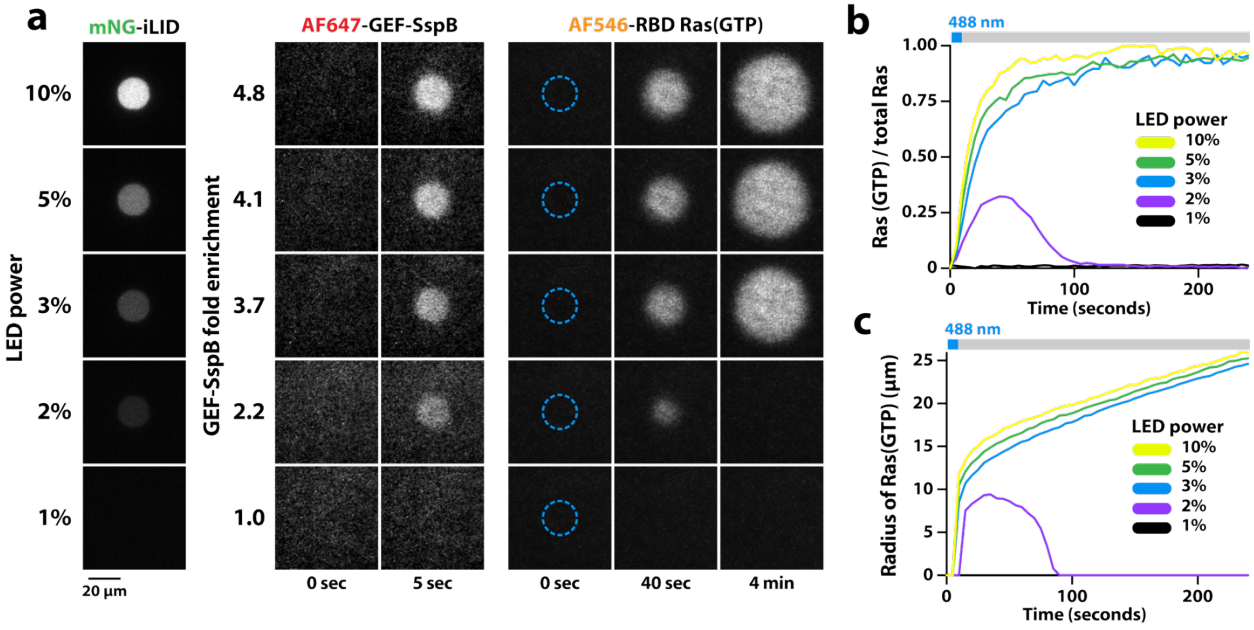

Figure 4.2 Light-inducible Ras feedback circuit requires a threshold density of activated Ras molecules to exhibit amplification
(a) Representative TIRF-M images showing the region of iLID emission following excitation with patterned 488 nm light over a range of % LED power (left, see **Supplementary Fig. 2**), AF647-GEF-SspB membrane localization with corresponding fold enrichment (middle), and the resulting Ras activation over time (right) in the presence of 544 nM GAP. **(b)** Change in the fraction of locally activated Ras over time for the experiment shown in **(a). (f)** Change in the radii (µm) of the regions of AF546-RBD fluorescence over time for the experiment shown in **(a)**. **(a-c)** Membrane composition: 92% DOPC, 2% NiNTA (+iLID bound), 2% MCC-PE (+Ras bound), and 4% PIP_2 lipids.

Positive feedback drives Ras(GTP) spatial amplification as a Fisher-KPP wave

To confirm that the spatial amplification of Ras(GTP) was indeed due to the presence of GEF-mediated positive feedback, we performed two identical Ras activation experiments with either $GEF_{Ras(GTP)}$ or an equivalent concentration of GEF lacking positive feedback (**Fig. 4.3a**). Whereas Ras activation following light-mediated activation (30% LED power) in the control experiment remained local and transient due to global inhibition, the presence of the $GEF_{Ras(GTP)}$-mediated positive feedback loop allowed the

Ras activation reaction to locally outpace GAP activity. The resulting AF546-RBD (active Ras) signal grew in intensity and expanded across the bilayer with an average velocity of 0.06 μm/second (**Fig. 4.3a-c**).

The sharp boundaries and rapid expansion of the Ras(GTP) region we observed in the presence of $GEF_{Ras(GTP)}$ are reminiscent of a Fisher-KPP wave[146]. In its simplest form, the Fisher-KPP equation describes a propagating wave that arises due to diffusion and nonlinear logistic growth. To estimate the diffusion coefficient of Ras(GTP) in an expanding Fisher-KPP wave, we evaluated the wave velocity ($v \approx 2\sqrt{D * k_{net}}$) and wave front width ($w \approx \sqrt{D/k_{net}}$) (**Fig. 4.3c, d**). Based on a wave velocity of 0.06 μm/second and a wave width of 10.5 μm, we calculated a diffusion coefficient of 0.35 μm^2/second for membrane bound Ras(GTP). This estimate was in good agreement with an experimentally determined Ras(GTP) diffusion coefficient of ~0.5 μm^2/second which we measured through single particle tracking of AF647-RBD bound to Ras(GTP) (**Fig. 4.3e**).

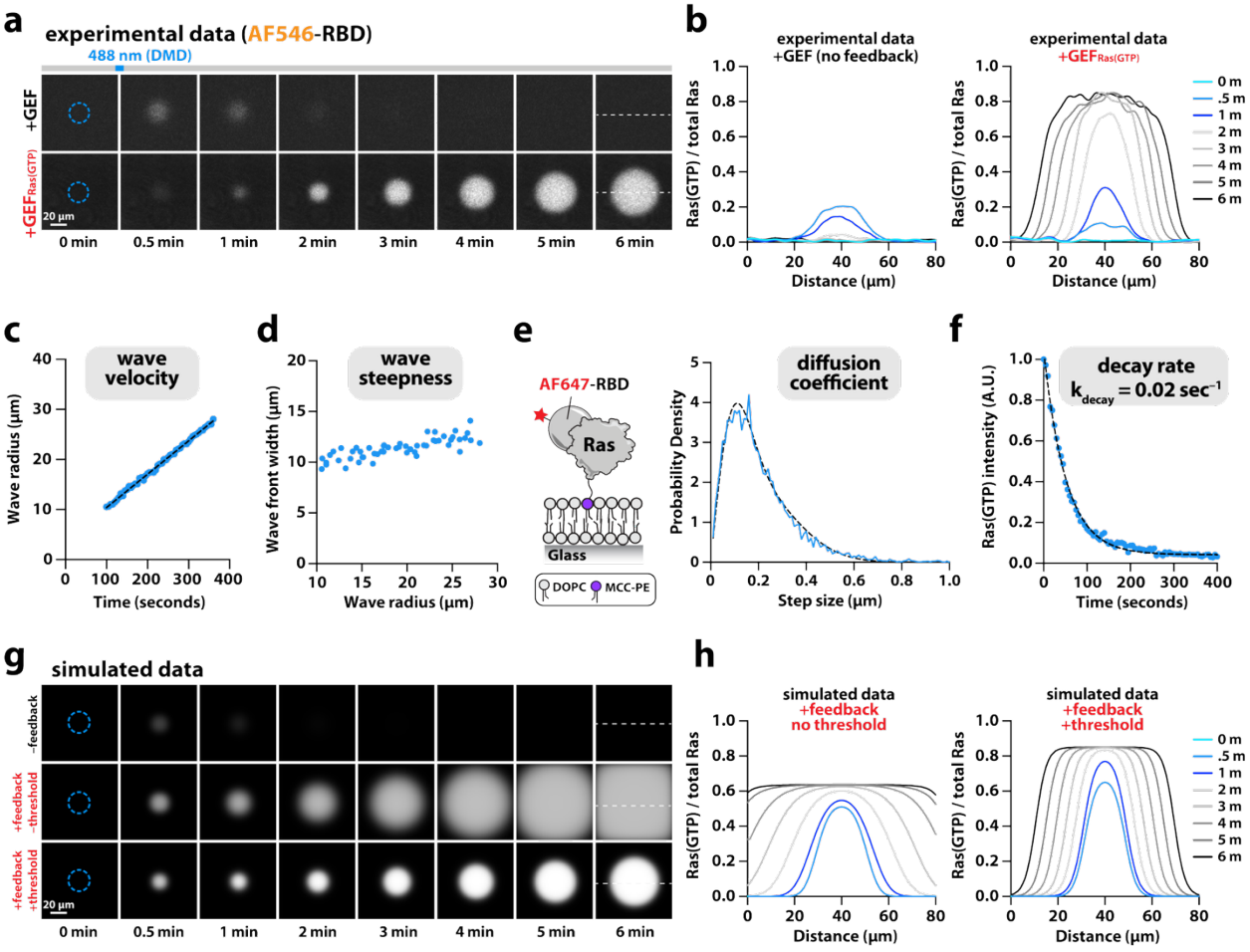

Figure 4.3 Positive feedback drives Ras(GTP) spatial amplification as a Fisher-KPP wave
(a) Representative TIRF-M montages showing the time-dependent change in Ras activation following a 488 nm light pulse in a 20 μm-diameter circular membrane region in the presence of 10 nM GEF or 10 nM $GEF_{Ras(GTP)}$ and 400 nM GAP. **(b)** Intensity line scans showing the fraction of locally activated Ras over time for the experiments shown in **(a)**. **(c)** Wave radius (μm) over time for the experiment shown in **(a)**. Wave front velocity (slope) was 0.06 μm/sec. **(d)** Wave front width measured in the experiment shown in **(a)**. Width is defined as the distance over which the AF546-RBD intensity is 10-90% of the total AF546-RBD membrane intensity. **(e)** Single molecule diffusion of Ras(GTP) measured by tracking AF647-RBD. Step size distribution plots were generated from single molecule tracking in the presence of 10 pM AF647-RBD. Data fit to a two species model yielded the following values: D1 = 0.192 μm^2/sec, D2 = 0.827 μm^2/sec, α = 0.44, n = 11240 displacement events. **(f)** GAP-mediated decay in the experiment shown in **(a)**. Integrated intensity of AF546-RBD sensor bound to Ras(GTP) fit to a single exponential decay curve (k_{decay} = 0.02 sec^{-1}). **(g)** Montages of simulated images obtained using the Fisher-KPP equation with no positive feedback (top), feedback without an activation threshold (middle), and feedback with an activation threshold (bottom). **(h)** Intensity line scans showing the fraction of locally activated Ras over time for the simulations shown in **(g)**. See **Supplementary Fig. 4** for

intensity line scans showing the fraction of locally activated Ras over time for the simulation lacking positive feedback. **(a-f)** Membrane composition: 92% DOPC, 2% NiNTA (+iLID bound), 2% MCC-PE (+Ras bound), and 4% PIP_2 lipids. 30% LED power was used for activating light pulses.

In contrast to the original Fisher-KPP equation, our reaction-diffusion model also requires a decay term to represent global GAP-mediated inhibition. To estimate the decay rate, we quantified the kinetics of reversible light-induced Ras activation measured in the absence of GEF-mediated positive feedback (**Fig. 4.3a**). In this experiment, decay in the Ras(GTP) signal is due to a combination of diffusion away from the initial site of Ras activation and GAP-mediated inhibition. By quantifying the disappearance of the Ras(GTP) signal in the activation site as well as the surrounding membrane region, we eliminated the contribution of Ras(GTP) diffusion to the overall decay rate. Fitting the decay curve to a single exponential allowed us to calculate a decay rate of 0.02 sec^{-1} (**Fig. 4.3f**).

Using experimentally measured parameters (**Fig. 5c-f**), we simulated the spatial distribution of membrane bound Ras(GTP) as a Fisher-KPP wave in the presence of GAP-mediated decay. Like our biochemical reconstitutions, we found that our simulations required positive feedback for signal amplification and wave expansion (**Fig. 5g**). Comparing our initial simulations to the experimental data revealed discrepancies including a ~5-fold increased wave velocity and a more diffuse wave front (**Fig. 5g**). To reconcile these differences, we considered that wave propagation requires a threshold Ras(GTP) density of ~35% (~350 out of ~1000 total molecules/μm^2) (**Fig. 4.2**). Ras(GTP) molecules that diffuse outside the wave boundaries are rapidly inactivated. Incorporating

an activation threshold into our model sharpened the wave boundary and slowed the wave velocity (**Fig. 5g, h**). The resulting bistable Fisher-KPP wave matched the spatial expansion we observed in our experiments with GEF-mediated positive feedback remarkably well (**Fig. 5a, g**). Similar wave dynamics were observed in simulations using diffusion coefficients ranging from 0.3-0.6 μm^2/second (**Supplementary Fig. 5**). However, simulations with faster Ras(GTP) diffusion (i.e. >0.7 μm^2/sec) could not support signal amplification and wave expansion since the positive feedback circuit could not sustain activity above the activation threshold and outpace GAP-mediated inhibition

Diffusion modulates spatial coupling between Ras activation and PIP_3 synthesis

In the experiments described in Chapter Two, we visualized PIP_3 production by the PI3Kγ heterodimer consisting of the p110γ catalytic subunit and the p101 regulatory subunit using an AF546-labeled LBD (PIP_3 Lipid Binding Domain) derived from BTK (Bruton's Tyrosine Kinase). We found that the PI3Kγ complex can be activated on SLBs by GβGγ subunits and that its lipid kinase activity is substantially enhanced in the presence of both GβGγ and Ras(GTP). We also showed that including soluble PTEN lipid phosphatase in our reconstitution prevented GβGγ-dependent, Ras-independent PIP_3 generation and that PI3Kγ activity was able to overcome PTEN-mediated lipid dephosphorylation when we rapidly activated Ras by introducing a GEF. PI3Kγ, membrane-bound Ras, membrane-bound GβGγ, and PTEN comprise a switchable, reconstituted signaling module that only leads to PIP_3 generation when Ras is active. Notably, in the presence of GAP and high concentrations (>30 nM) of $GEF_{Ras(GTP)}$ we

observed spatial correlation between spontaneously formed patterns of Ras(GTP) and regions of AF546-LBD fluorescence (i.e. PIP_3) (**Fig. 4.4b**). Interestingly, although the overlap between the two signals was unambiguous, the boundaries of the Ras(GTP) regions were consistently sharper than those of PIP_3.

To study the spatial coupling between Ras(GTP) and PIP_3 production on membranes, we combined our reconstituted Ras-PI3Kγ module in the presence of global negative regulators (i.e. GAP and PTEN) with light-inducible Ras activation (**Fig. 4.4a**). First, we examined the spatiotemporal amplification of Ras(GTP) and PIP_3 following transient membrane recruitment of the GEF-SspB initiator in the presence of $GEF_{Ras(GTP)}$-mediated positive feedback (**Fig. 4.4c, d**). As previously observed, light-induced recruitment of GEF-SspB resulted in the local production of Ras(GTP), which was then spatially amplified by $GEF_{Ras(GTP)}$. Compared to reconstitutions performed in the absence of membrane-anchored GβGγ, these Ras(GTP) waves expanded more slowly due to molecular crowding (**Supplementary Fig. 6**). Under these conditions, we also found that local PI3Kγ activity was able to outcompete PTEN-mediated dephosphorylation of PIP_3. Although PIP_3 generation lagged behind that of Ras(GTP), the region of AF546-LBD biosensor fluorescence tracked the Ras(GTP) signal and expanded beyond the original light-activated region. These results demonstrate that a minimal GEF-mediated positive feedback loop is sufficient for both Ras activation and downstream PI3Kγ-dependent PIP_3 production to overcome global GAP- and PTEN-mediated inhibition.

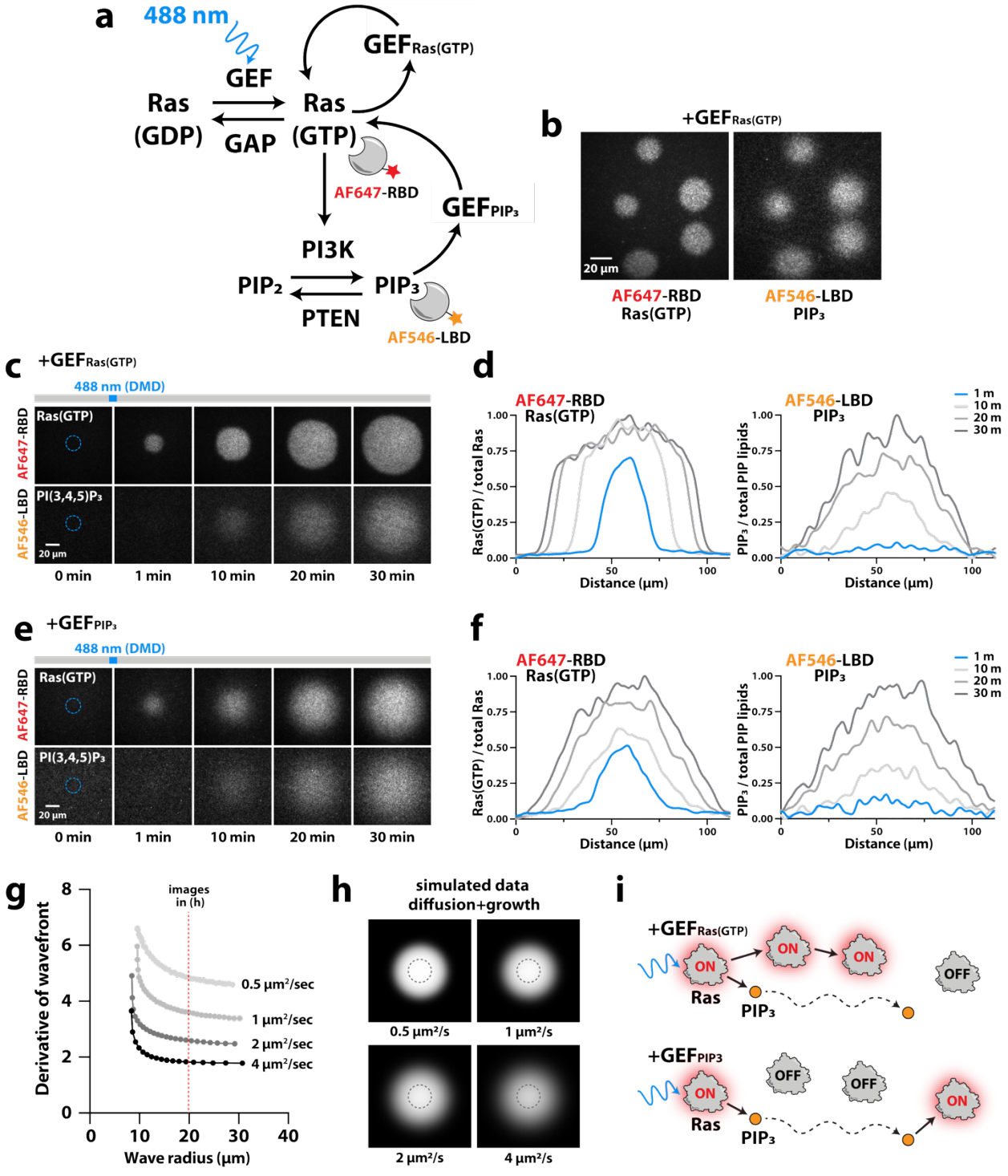

Figure 4.4 Diffusion modulates spatial coupling between Ras activation and PIP_3 synthesis

(a) Diagram of communication between light-induced Ras activation and PI3Kγ-dependent PIP_3 generation. Adding $GEF_{Ras(GTP)}$ or GEF_{PIP3} to the module introduces a positive feedback loop. **(b)** Ras(GTP) and PIP_3 spontaneously form bistable patterns in the presence of GAP and high concentrations of $GEF_{Ras(GTP)}$. Representative TIRF-M images showing PI3Kγ-dependent PIP_3 generation colocalizing with regions of spontaneous Ras activation in the absence of activating light. **(c)** Representative montages showing the time-dependent change in Ras activation and PIP_3 generation following a 488 nm light pulse (blue circle) in the presence of the $GEF_{Ras(GTP)}$-mediated positive feedback loop and 450 nM GAP. **(d)** Intensity line scans corresponding to the experiment shown in **(c)**. **(e)** Representative montages showing the time-dependent change in Ras activation and PIP_3 generation following a 488 nm light pulse (blue circle) in the presence of the GEF_{PIP3}-mediated feedback loop and 810 nM GAP. **(f)** Intensity line scans corresponding to the experiment shown in **(e)**. **(g)** Ras(GTP) Fisher-KPP waves were simulated with varying Ras membrane diffusivity. The steepness (i.e. derivative) of the Ras(GTP) wave edge changes based on the diffusivity of Ras as the activated region expands. **(h)** Images of simulated Ras(GTP) Fisher-KPP waves following expansion to a radius of 20 μm. The dashed circle represents the initial region of Ras activation. **(i)** Model for different wave characteristics observed in the presence of $GEF_{Ras(GTP)}$ and GEF_{PIP3}. **(b-f)** Membrane composition: 92% DOPC, 2% NiNTA (+iLID bound), 2% MCC-PE (+Ras bound), and 4% PIP_2 lipids, +GβGγ-farnesyl. 30% LED power was used for activating light pulses.

In vivo, GEFs mediate feedback loops that drive GTPase activation based on PIP_3-dependent membrane recruitment and activation[13,107]. Having successfully reconstituted Ras(GTP)-PI3Kγ communication in the presence of positive feedback, we aimed to reconstitute a second GEF-mediated feedback circuit that could amplify Ras signaling downstream of PI3Kγ-dependent PIP_3 production (**Fig. 4.4a**). Much like for the $GEF_{Ras(GTP)}$-mediated feedback loop, we engineered this feedback loop by fusing a BTK-derived LBD (PIP_3 Lipid Binding Domain) to a SOS1 GEF domain to generate a chimeric activator we refer to as GEF_{PIP3}. Following transient, light-induced membrane recruitment of the GEF-SspB initiator, GEF_{PIP3} was indeed able to drive the spatial expansion of Ras(GTP) and PIP_3 generation on membranes (**Fig. 4.4e, f**). These activity waves exhibited similar dynamics to those we observed in the presence of $GEF_{Ras(GTP)}$. The results of introducing $GEF_{Ras(GTP)}$ and GEF_{PIP3} to our reconstituted pathway provide

evidence for the sufficiency of simple, GEF-mediated feedback circuits to produce PIP_3 signal amplification, an essential step in numerous cell signaling pathways[11–15].

Although the PIP_3 signal was spatially correlated with Ras(GTP) in the presence of both $GEF_{Ras(GTP)}$ and GEF_{PIP3}, we observed a pronounced difference in the boundary steepness of Ras(GTP) waves when comparing the two feedback circuits (**Fig. 4.4b-f**). Positive feedback mediated by $GEF_{Ras(GTP)}$ invariably resulted in a uniformly bright Ras(GTP) region with a steep wavefront (**Fig. 4.4c, d**). The PIP_3 wavefronts were less defined than those of Ras(GTP). Importantly, when Ras activation depended on the generation of rapidly diffusing PIP_3 lipids due to GEF_{PIP3}, the Ras(GTP) wavefront more closely resembled the gradual boundary of the PIP_3 region. Overall, these observations are consistent with the markedly different diffusion coefficients of membrane-tethered Ras (0.3-0.6 μm^2/second) and lipids within the supported membrane (~3 μm^2/second) (**Fig. 4.3** and **Supplementary Fig. 7**). To model the effect of diffusivity on wavefront expansion and steepness, we simulated Fisher-KPP wave growth using a range of diffusion coefficients for the membrane bound species (i.e. Ras or PIP_3) (**Fig. 4.4g, h**). Following spatially patterned activation, simulated Fisher-KPP waves expanded at rates proportional to the diffusion coefficient. However, the steepness of the wave boundary decreased as diffusivity increased (**Fig. 4.4g**), a result that is consistent with the spatial coupling observed between Ras(GTP) and PIP_3 in our reconstitution. These results support a model in which the lateral membrane diffusion of reacting species together with

regulatory circuit architecture modulate the spatial coupling and evolution of membrane signaling reactions (**Fig. 4.4i**).

DISCUSSION

This study establishes a framework for reconstituting communication and feedback between membrane signaling reactions involving small GTPases, PIP lipids, and the enzymes that regulate their production. The iLID-SspB system allows us to rapidly shift reactions at steady state into new signaling regimes in a spatially controlled manner. Using this technique, we examined two membrane recruitment-based positive feedback circuits and the requirements for a reconstituted Ras-PI3Kγ signaling module to overcome global negative regulation and amplify in space and time. We demonstrated that an initial threshold density of membrane-localized GEF is required to outcompete GAP-mediated Ras regulation. When this threshold is achieved, GEF-mediated positive feedback triggers signal amplification in the form of an expanding Fisher-KPP wave. Otherwise, the membrane signaling reaction resets with dynamics reminiscent of cellular signal adaptation[23]. For a feedback circuit that links Ras activation to PIP_3 production, the spatiotemporal coupling of the two reactions is regulated by differences in lateral membrane diffusion of Ras(GTP) and PIP_3 lipids. Our observations support the conclusions of kinetic modeling work in which less diffusive molecules exhibit more robust polarity in two-component reaction-diffusion systems with positive feedback based on product binding[140].

In vivo, communication between Ras and PIP_3 exists within an extensive and interconnected network of positive and negative feedback loops. Positive feedback in the cellular Ras-PI3K signaling module can at least in part be attributed to GEFs that are recruited to the plasma membrane by active Ras itself and direct interactions with downstream PIP_3. These GEFs function analogously to the chimeric GEFs used in our assay although they contain additional layers of regulation, such as reversible autoinhibition. In nature, processive membrane association of RasGEFs also plays a role in increasing local Ras(GTP) density and promiscuous GEFs that bind multiple classes of small GTPases via their allosteric or catalytic domains amplify signaling events beyond direct Ras signaling[28,31,147,148]. There is also a large body of evidence supporting Ras-independent feedback circuits mediated by downstream effectors in the PI3K signaling pathway. For example, PIP_3 generation promotes the recruitment of GEFs such as Vav, P-Rex, and the DOCK/ELMO complex, which activate Rac GTPase[107,149–153]. GTPases including Rac, Cdc42, and RhoG, which are activated in parallel and downstream of Ras, can also stimulate PI3K activity. PI3K-mediated PIP_3 generation and Rac activation lead to the formation of branched actin networks which deform the membrane and produce force at the leading edge of migratory cells[154,155]. Dendritic actin networks also promote PIP_3 production by delivering signaling molecules including PI3K and various GEFs to the cell cortex in a polarized manner[14,29,83,156–158]. Cell biological evidence points to the presence of myriad positive feedback circuits in signaling networks and computational modeling has led to speculation about considerably more. Few of these circuits have been

interrogated through biochemical reconstitution. Our study represents an exploration of a single regulatory module that is known to influence hundreds of signaling molecules in living cells.

Steady-state cellular conditions can also be altered by mutations to the molecules that comprise signaling networks. Dysregulation of key nodes like Ras and PI3K has long been known to have severe cellular consequences which has flagged these molecules and their associated regulators as important cancer therapeutic targets[3,18,19,39,79,145,159,160]. The negative regulators we used in our in vitro assay, NF1 RasGAP and PTEN phosphatase, are well-characterized tumor suppressors that prevent aberrant Ras and PIP_3 signaling[17,161]. Cancer cell lines which have lost NF1 RasGAP expression exhibit elevated steady-state levels of Ras(GTP)[162]. Conversely, enhancing the membrane binding of PTEN in cells expressing constitutively active PI3K leads to a marked decrease in membrane PIP_3[86]. Biochemical reconstitution of GTPase and PIP lipid signaling in the presence of mutated GTPases, kinases, and their respective regulators will shed light on how the relationships between these molecules determine the properties of healthy and diseased cells. In addition to influencing steady-state conditions, alterations to regulatory modules via mutations or relative protein concentrations can affect how signaling networks transition between steady states. For this reason, it is important to monitor the dynamic evolution of reactions in addition to measuring steady state conditions when investigating perturbations to signaling networks.

One aspect of cell signaling that was not explored in this study is negative feedback, which can be broadly categorized as long-range or local. Long-range negative feedback mediated by cortical membrane-cytoskeletal tension allows for the establishment and maintenance of asymmetry over the length of a polarized cell[163,164]. By contrast, local negative feedback relies on the products of specific biochemical reactions recruiting negative regulators and is fundamental for signal adaptation. In the context of directed cell migration, local negative feedback prevents cells from becoming "polarity-locked" by maintaining their flexibility and sensitivity to changes in environmental signals[15,23,125,141,149,165]. GAPs, which directly oppose GEF activity, are natural candidates for mediating local delayed negative feedback[29,166]. Unsurprisingly, various GAPs have been shown to serve functions in directed cell migration[167,168] and signal adaptation[149]. Like GEFs, some GAPs may be directly recruited to the membrane by small GTPases[168]. Additionally, there is evidence for different classes of GAPs binding to PIP_3 and a downstream product, $PI(3,4)P_2$[169–172]. $PI(3,4)P_2$ which is converted from PIP_3 by 5-phosphatases has also been shown to play a role in adaptive endocytic pathways through which activated receptors are turned over at the leading edge of migrating cells[173]. Interestingly, actin networks, which promote PI3K activity and mediate long-range negative feedback, also participate in local negative feedback by inhibiting Rac and Rho GTPases[149,174,175]. Filamentous actin is hypothesized to deliver GAPs directly to the membrane and may also physically drive the dissociation of signaling molecules through network treadmilling[29,176]. We relied on transient inputs and global negative regulation to

build reversibility into our assay. This work provides a foundation for future reconstitutions of adaptive modules that depend on both positive and negative feedback regulation.

METHODS

Protein expression, purification, and labeling

PI3Kγ, AF546-LBD, H-Ras, GEF, GβGγ-farnesyl, PTEN, his_{10}-mNeonGreen-iLID, GEF-SspB, AF546-RBD, AF647-RBD, and GAP were purified as described in Chapter Two.

$GEF_{Ras(GTP)}$. A gene sequence encoding the $GEF_{Ras(GTP)}$ chimera was expressed in BL21 *E. coli* as a his_{10}-TEV-SUMO3-SosCat(564-1049aa)-SNAP-RBD fusion protein. Bacteria were grown at 37°C in Terrific Broth to an absorbance of 0.8 at 600 nm. Culture was shifted to 27°C for 1 hour then induced with 0.1 mM IPTG. Expression was allowed to continue for 13 hours before harvesting. Cells were lysed in 50 mM Na_2HPO_4 [pH 8.0], 400 mM NaCl, 0.4 mM βME, 1 mM PMSF, 100 µg/mL DNase by sonication. Lysate was centrifuged at 15,000 rpm (35000 x g) for 60 minutes in a Beckman JA-20 rotor at 4ºC. Lysate was circulated over a 5 mL HiTrap chelating column (Cytiva GE17-0409-01) charged with 100 mM $CoCl_2$ for ten minutes. Column was washed with 50 mM Na_2HPO_4 [pH 8.0], 400 mM NaCl, 10 mM imidazole, 0.4 mM βME. Bound protein was eluted in 50 mM Na_2HPO_4 [pH 8.0], 400 mM NaCl, 500 mM imidazole, 0.4 mM βME. Peak fractions were pooled and a his_6-SenP2 SUMO protease was added to cleave off the SUMO3 tag. The solution was dialyzed against 4 liters of buffer containing 20 mM HEPES [pH 7.5], 400 mM NaCl, 5% glycerol, 0.4 mM βME. Dialysate containing cleaved protein was

recirculated over the HiTrap chelating column for 90 minutes. Flowthrough was concentrated in a 30 kDa MWCO Amicon-Ultra concentrator before loading onto a desalting column equilibrated in 20 mM Tris [pH 8.0], 150 mM NaCl, 10% glycerol, 1 mM TCEP. Peak fractions were pooled and snap frozen in liquid nitrogen for storage at -80ºC.

A portion of the purified $GEF_{Ras(GTP)}$ (SOS1(564-1049aa)-SNAP-RBD) was labeled with 1.5x molar excess SNAP-Surface Alexa546 dye (NEB, Cat# S9132S) overnight at 4ºC in buffer containing 20 mM Tris [pH 8.0], 200 mM NaCl, 1 mM TCEP. The next day, the labeled protein was loaded onto a PD10 desalting column equilibrated in buffer containing 20 mM Tris [pH 8.0], 200 mM NaCl, 10% glycerol, 1 mM TCEP to remove most of the free SNAP dye. It was then concentrated in an Amicon-Ultra concentrator and loaded onto a Superdex 75 column equilibrated in 20 mM Tris [pH 8.0], 200 mM NaCl, 10% glycerol, 1 mM TCEP. Unreacted SNAP dye and labeled protein were separated by size exclusion chromatography. The peak fractions were pooled, concentrated, aliquoted, and snap frozen in liquid nitrogen for storage at -80ºC.

GEF_{PIP3}. The protein referred to as GEF_{PIP3} comprises an LBD (PIP_3 Lipid Binding Domain) derived from BTK fused to the catalytic domain of SOS1(564-1049aa). This chimeric protein was expressed using a gene sequence encoding his_6-SUMO-BTK(R49S/K52S)-SOS1(564-1049aa) in BL21(DE3) *E. coli* containing vectors for constitutive expression of Trigger factor and rare tRNAs (i.e. pRIL). Bacteria were grown at 37°C in Terrific Broth to an absorbance of 0.8 at 600 nm. Cultures were shifted to 18°C for 1 hour then induced with 0.1 mM IPTG. Expression was allowed to continue for 18

hours before harvesting. Cells were lysed in 50 mM Na_2HPO_4 [pH 8.0], 400 mM NaCl, 10 mM imidazole, 4 mM βME, 1 mM PMSF, 100 µg/mL DNase by sonication. Lysate was centrifuged at 15,000 rpm (35000 x *g*) for 60 minutes in a Beckman JA-20 rotor at 4ºC. NiNTA resin was added to the supernatant and allowed to bind for 1 hour, then washed with 50 mM Na_2HPO_4 [pH 8.0], 400 mM NaCl, 10 mM imidazole, 4 mM βME. Bound protein was eluted in 50 mM Na_2HPO_4 [pH 8.0], 400 mM NaCl, 500 mM imidazole, 4 mM βME. Peak fractions were pooled and an Ulp1 protease was added to cleave off the his_6-SUMO tag. The solution was dialyzed against 4 liters of buffer containing 50 mM Na_2HPO_4 [pH 8.0], 300 mM NaCl, 20 mM imidazole, 5% glycerol, 0.4 mM βME. Dialysate containing cleaved protein was recirculated over NiNTA resin. Flowthrough was loaded onto a G25 Sephadex desalting column equilibrated in 20 mM HEPES [pH 7.0], 50 mM NaCl, 1 mM TCEP. Peak fractions were pooled and loaded onto a HiTrap CaptoS cation exchange column. GEF_{PIP3} eluted in the presence of 450 mM NaCl. These fractions were concentrated in a 50 kDa MWCO Amicon-Ultra concentrator and snap frozen in liquid nitrogen for storage at -80ºC.

Supported lipid bilayer experiments

Preparation of supported lipid bilayers. The following lipids were used to generate Small Unilamellar Vesicles (SUVs) and subsequently supported lipid bilayers: 1,2-dioleoyl-sn-glycero- 3-phosphocholine (18:1 DOPC, Avanti #850375C), L-α-phosphatidylinositol-4,5-bisphosphate (Brain PIP_2, Avanti #840046X), 1,2-dioleoyl-sn-glycero-3-phosphoethanolamine-N-[4-(p-maleimidomethyl) cyclohexane-carboxamide]

(18:1 MCC-PE, Avanti #780201C), and 1,2-dioleoyl-sn-glycero-3-[(N-(5-amino-1-carboxypentyl)iminodiacetic acid)succinyl] (18:1 DGS-NTA(Ni), Avanti #790404C). To prepare SUVs, a total of 2 μmoles of lipids were combined in a 35 ml glass round bottom flask containing ~2 ml chloroform.

Lipids were dried to a thin film using rotary evaporation with the glass round-bottom flask submerged in a 42ºC water bath. The lipid film was then resuspended in 2 ml filtered PBS [pH 7.4] (Corning, cat# 46-013-CM), bringing the lipid suspension to a final concentration of 1 mM. All lipid mixtures expressed as percentages (e.g. 98% DOPC, 2% PIP_2) are equivalent to molar fractions. To generate 50 nm SUVs, the 1 mM lipid mixture was extruded through a 0.05 μm pore size 19 mm polycarbonate (PC) membrane (Cytiva Whatman, Cat# 800308) with filter supports (Cytiva Whatman, Cat# 230300) on both sides of the PC membrane.

To create supported lipid bilayers, coverglass (25x75 mm, IBIDI, Cat #10812) was initially cleaned with 2% Hellmanex III (Fisher, Cat #14-385-864) that was heated to 60-70ºC in a glass coplin jar and incubated for at least 30 minutes. After rinsing the Hellmanex-cleaned glass with MilliQ water, the coverglass was etched with Piranha solution (1:3, hydrogen peroxide:sulfuric acid) for 10-15 minutes. Etched coverglass that was rinsed and stored in MilliQ water, was removed from the Coplin jar and rapidly dried with nitrogen gas before adhering to a 6-well, sticky-side chamber (IBIDI, Cat #80608). To create a supported lipid bilayer, a total lipid concentration of 0.25 mM SUVs in PBS [pH 7.4] was flowed into the IBIDI chamber. After 30 minutes of incubation, supported

membranes were washed with 5 ml PBS [pH 7.4] to remove non-absorbed SUVs. Membrane defects were then blocked for ~5 minutes with 1 mg/ml β-casein (ThermoFisher, Cat #37528) diluted in PBS [pH 7.4]. To reduce the fraction of immobile proteins on SLBs, the 10 mg/ml β-casein solution was centrifuged in a TLA120.2 at 100,000 rpm (434,513 x *g*) for 30 minutes at 4ºC using an Optima MAX-TL ultracentrifuge. After blocking bilayers with β-casein, membranes were washed again with 1 ml PBS [pH 7.4] and 1 ml PBS [pH 7.4], 1 mM $MgCl_2$, 100 μM GDP, 0.1 mM TCEP prior to H-Ras conjugation. Prior to imaging, supported membranes were washed with TIRF-M imaging buffer.

Membrane conjugation. For experiments involving membrane conjugated H-Ras, β-casein-blocked supported lipid bilayers containing MCC-PE lipids were incubated for 2 hours with 30-35 μM H-Ras at 23ºC in buffer containing PBS [pH 7.4], 1 mM $MgCl_2$, 100 μM GDP, 0.1 mM TCEP. Bilayers were quenched in PBS [pH 7.4], 5 mM βME for 10 minutes before washing with PBS [pH 7.4], 1 mM $MgCl_2$, 100 μM GDP, 0.1 mM TCEP. The resulting Ras membrane density ranged from 1000-2000 molecules/μm^2 as previously described[33].

For experiments involving iLID and/or GβGγ, bilayers containing NiNTA lipids were incubated with 20-50 nM his_{10}-mNG-iLID and/or GβGγ for 20 minutes at 23ºC. Unbound his_{10}-mNG-iLID and/or GβGγ was flushed out of the chamber with TIRF-M imaging buffer.

TIRF microscopy imaging buffer. All supported lipid bilayer TIRF-M experiments were performed in 200 μl reaction volumes using the following reaction buffer: 20 mM

HEPES [pH 7.0], 150 mM NaCl, 1 mM ATP (Sigma, Cat #A2383-10G), 100 μM GTP, 5 mM $MgCl_2$, 0.5 mM EGTA, 20 mM glucose, 200 μg/ml β-casein (ThermoScientific, Cat #37528), 20 mM βME, 320 μg/ml glucose oxidase (Serva, Cat #22780.01 *Aspergillus niger*), 50 μg/ml catalase (Sigma, Cat #C40-100MG Bovine Liver), and 2 mM Trolox (Cayman Chemicals, Cat #10011659). Perishable reagents (i.e. glucose oxidase, catalase, and Trolox) were added 5-10 minutes before initiating biochemical reconstitutions on SLBs and acquiring images. All reactions in this study were reconstituted and visualized on a TIRF microscope at 23ºC.

Microscope hardware and imaging acquisition. Imaging experiments were performed using an inverted Nikon Ti2 microscope using either a 60x (1.49 NA) or 100x (1.49 NA) oil immersion Nikon TIRF objective. The x-axis and y-axis positions were controlled using a Nikon motorized stage, joystick, and NIS element software. Fluorescently labeled proteins were excited with either a 488, 561, or 637 nm OBIS laser diode (Coherent Inc. Santa Clara, CA) controlled with a Vortran laser launch (Sacramento, CA) and acousto-optic tuneable filters (AOTF) control. Excitation and emission light was transmitted through a multi-bandpass quad filter cube (C-TIRF ULTRA HI S/N QUAD 405/488/561/638; Semrock) containing a dichroic mirror. For bulk excitation of fluorescent biosensors, laser power measured through a 60x TIRF objective ranged from 0.5-2 mW. Fluorescence emission was detected on an iXion Life 897 EMCCD camera (Andor Technology Ltd., UK) after passing through a Nikon Ti2 emission filter wheel containing the following 25 mm emission filters: ET525/50M, ET600/50M,

ET700/75M (Semrock). All experiments were performed at room temperature (23ºC). Microscope hardware was controlled with Nikon NIS elements.

Spatially patterned light. A Mightex Polygon400 digital micromirror device (DMD) controlled by NIS elements was used for patterned illumination. For activation of membrane bound iLID, excitation light from a SOLA SE light engine (Lumencor, 380-680 nm range of wavelengths) was filtered using a Chroma 488 nm long-pass dichroic mirror (25.5 x 36 x 2 mm; Cat #ZT488rdc-UF2). The dichroic mirror was mounted at 45º angle in a Nikon Ti2 LAPP (Cat #Ti2-LA-BM-E) prior to entering the microscope filter turret. This setup reflects iLID activating light from the Polygon400 DMD to the sample. The 488LP dichroic allowed transmission of 561 nm and 647 nm laser excitation light to image fluorescently labeled SspB, GEFs, and activity biosensors following activation of iLID. Following repetitive illumination of the same membrane region with 488 nm light, we observed a very slight increase in light-independent basal SspB recruitment. This potentially represents an accumulation of iLID protein that does not transition back to its "closed", dark-state conformation. For this reason, we changed the field of view between light-induced activation steps in the same reaction chamber for subsequent experiments.

Fisher-KPP wave simulations

A Fisher-KPP wave is a propagating wave that arises in reaction-diffusion systems with positive feedback[146]. The simplified Fisher-KPP equation follows:

$$\frac{\partial u}{\partial t} = D\nabla^2 + ru(1 - \frac{u}{K})$$

where ∇^2 is the Laplacian of u. In this simplified form of the Fisher-KPP equation, the growth term (r) lacks a nonlinear activation threshold and an opposing decay rate. To model the amplification and expansion of Ras(GTP) with an activation threshold in the presence of global GAP-mediated decay, we modified the Fisher-KPP equation as follows:

$$\frac{\partial Ras(GTP)}{\partial t} = D\left(\frac{\partial^2 Ras(GTP)}{\partial x^2} + \frac{\partial^2 Ras(GTP)}{\partial y^2}\right) + k_{growth} - k_{decay}$$

$$k_{growth} = r * Ras(GTP)\left(1 - \frac{Ras(GTP)}{Ras(total)}\right)\left(\frac{Ras(GTP)}{Ras(threshold)}\right)$$

$$k_{decay} = \lambda * Ras(GTP)$$

The concentration of Ras(GTP) at position x and time t was defined as u(x,t) or Ras(GTP)(x,t). Variables in the above equation are defined as follows: D is the diffusion coefficient (μm^2/second) of Ras(GTP), r is the intrinsic growth rate (sec^{-1}), and λ is the global GAP-mediated decay rate (sec^{-1}). $Ras(threshold)$ is the fraction of $Ras(total)$ required to overcome global GAP-mediated inhibition and persist. The maximum or total Ras density (*K*) was 1000 molecules/μm^2 although the absolute number of Ras molecules does not influence the simulation output. The threshold Ras(GTP) membrane density was empirically determined to be 0.35 (350 out of 1000 total molecules/μm^2) based on experiments shown in **Fig. 4.2**. The term $r * Ras(GTP)\left(1 - \frac{Ras(GTP)}{Ras(total)}\right)$ represents a logistic growth model in which the growth rate decreases as Ras(GTP) approaches $Ras(total)$. The term $\left(\frac{Ras(GTP)}{Ras(threshold)}\right)$ represents a non-linear activation term that creates

bistability in the Fisher-KPP wave. For net growth and wave expansion, k_{growth} must be greater than k_{decay}.

Using the experimental data shown in **Fig. 4.3**, the diffusion coefficient for Ras was estimated based on the following relationships:

$$wave\ width(w) \approx \sqrt{\frac{D}{k_{net}}}$$

$$wave\ velocity(v) \approx \sqrt{D * k_{net}}$$

The wave width (μm) was defined as the distance over which the Ras(GTP) biosensor membrane intensity is 10-90% of the total Ras(GTP) biosensor membrane intensity, which is directly proportional to the total Ras(GTP) membrane density. The relationship between the wave width (μm) of the wave front is equal to the square root of diffusion coefficient (μm^2/second) divided by the net growth rate ($second^{-1}$, $k_{net} = k_{growth} - k_{decay}$) for the overall reaction.

Data analysis

Fold enrichment and fold activation. To calculate the fold membrane enrichment of GEF-SspB (**Fig. 4.2**) we took into account both the basal level of light-independent recruitment and the maximum light-induced membrane recruitment, as previously described[138]. Fold membrane enrichment of AF647-GEF-SspB was calculated using (basal light-independent recruitment + peak 488 nm light dependent recruitment)/basal light-independent recruitment.

Wave radius over time. Ras(GTP) wave radius (μm) (**Fig. 4.2c**) was calculated as a function of time based on AF546-RBD fluorescence using the manual thresholding Fiji/ImageJ plugin[114]. Starting with an 8-bit image stack, images were globally thresholded at a pixel value of 40. Outlier fluorescent speckles caused by immobilized proteins and membrane defects smaller than 9 pixels were removed. The images were subsequently eroded using Fiji/ImageJ. These thresholded image stacks were further analyzed using Python code executed in Spyder 6 software. For each image in the time stack, radii were measured from the centroid of the Ras(GTP) region at 15 degree intervals (24 total) and averaged.

Intensity line scans. To generate the intensity line scans in **Fig. 4.3** and **Fig. 4.4**, images were first blurred in Fiji/ImageJ[114] using a Gaussian equation with a variance of 1.5 μm. Intensities were measured along a horizontal line at the center of each image. To determine the steepness of Fisher-KPP waves (**Fig. 4.4g**) we calculated the derivative at the wave front inflection point using Prism GraphPad 11.

Single particle tracking (Fig. 4.3e and Supplementary Fig. 7). Single molecules of AF647-RBD and Rhodamine PE and were identified and tracked using the ImageJ/Fiji TrackMate plugin as previously described[109,113]. Using the LoG detector in the TrackMate plugin, fluorescent particles were identified based on their size (~6 pixel diameter), brightness, and signal-to-noise ratio. The LAP tracker was used to generate trajectories that followed single molecule displacement (or step size in μm) as a function of time. Particle trajectories were filtered based on Track Start (particles at start of movie were

removed), Track End (particles at end of movie were removed), Duration (particles present for less than 2 frames were removed), and Track displacement. Immobilized particles were filtered out of the data at a frequence of 1-2% of all trajectories. The output files from TrackMate were then analyzed using Prism GraphPad 11.

Step-size distributions of single-particle trajectories were plotted in Prism. For all analyses presented here, the bin size for the step size distribution was 0.01 μm. For curving fitting, the step size distributions were plotted as probability density versus step size (μm). This was achieved by dividing the frequency distribution (i.e. y-axis values) by the bin size (0.01 μm). The probability density versus step size plots were fit to one- or two-species distributions as previously described[109].

BRIDGE TO CHAPTER FIVE

In Chapter Four, we demonstrated that GEF-mediated positive feedback results in the spatial and temporal amplification of a reconstituted Ras-PI3Kγ signaling module. We found that the dynamics of Ras activation and PIP_3 generation depend on input strength, feedback circuit architecture, and lateral membrane diffusion. Chapter Five will summarize the previous three chapters, discuss how these findings contribute to our understanding of plasma membrane signaling, and highlight future directions.

CHAPTER FIVE

CONCLUDING REMARKS

To execute specialized functions, cells must sense and respond to diverse signals. The plasma membrane serves as the interface between the intracellular and extracellular environments, where large networks of biochemical reactions translate external cues into specific cellular behaviors and fates[16,18,24,29]. The research presented in this dissertation plays a part in unraveling the complexity of cellular signal transduction through the reconstitution of molecular interactions and feedback circuits on supported lipid bilayers.

Historically, plasma membrane PI(4)P was viewed primarily as a precursor to the PIP_2 signaling lipid. However, recent studies have revealed that PI(4)P plays a more substantial role in organizing membrane signaling than previously recognized[8,61] and PI4KIIIα, the kinase responsible for plasma membrane PI(4)P production, has emerged as a therapeutic target[6,7,50]. In Chapter Two, we described two mechanisms by which PI4KIIIα activity can be modulated: nanobody-mediated disruption of the PI4KIIIα-EFR3 interaction to prevent membrane recruitment of the enzyme complex[46] and phosphorylation of a conserved kinase domain residue to directly inhibit its catalytic activity[89]. These biochemical insights provide a foundation for future in vivo studies that will determine the relevance of these regulatory mechanisms within the native cellular context.

PI3Kγ is a key initiator of signaling cascades in hematopoietic cells and, like all Class I PI3Ks, is frequently misregulated in cancers and other human diseases[3,38–40]. In

Chapter Two, we reconstituted the activity of the PI3Kγ complex consisting of the p110γ catalytic subunit and the p101 regulatory subunit as well as of the isolated p110γ catalytic subunit. We examined how these proteins integrate signaling inputs from Ras(GTP) and GβGγ. While the free p110γ catalytic subunit can be activated by Ras(GTP) in the absence of GβGγ, the activity of the full p110γ-p101 complex depends on GβGγ and is insensitive to Ras(GTP) alone. However, under antagonistic pressure from PTEN lipid phosphatase in the presence of GβGγ, Ras activation is sufficient to stimulate rapid PIP_3 production by the PI3Kγ complex.

To further probe the spatial dynamics of Ras and PI3Kγ activation, we established a light-inducible system to initiate signaling reactions in defined regions of supported membranes. Described in Chapter Three, this approach depends on the transient heterodimerization of membrane-tethered iLID[35] and soluble GEF-SspB. Upon GEF-SspB membrane recruitment, we observed local activation of membrane-conjugated Ras. In Chapter Four, we linked light-inducible Ras activation to PI3Kγ-dependent PIP_3 synthesis. A key feature of this reconstitution is global GAP- and PTEN-mediated inhibition. In unstimulated cells, these factors oppose spurious Ras(GTP) and PIP_3 generation, thereby guarding against cancerous phenotypes[17,86,161,162]. However, in vivo negative regulation of Ras and PI3Kγ is often more complex than direct inhibition. For example, in Chapter Two, we showed that many of the same cell surface receptors that activate PI3K are among the most likely to inhibit PI4KIIIα though phosphorylation. Decreased PI4KIIIα activity potentially feeds back to attenuate PIP_3 and Ras signaling by

limiting the PIP_2 substrate of PI3K or decreasing the plasma membrane density of PS. This and numerous other proposed negative feedback circuits have yet to be interrogated in vivo or in vitro.

To overcome layers of negative regulation and enter signaling states, cells rely on positive feedback loops that amplify Ras and PIP_3 signaling downstream of receptor activation. In Chapter Four, we explored two GEF-mediated positive feedback loops and showed that they drive the propagation of Ras activation and PIP_3 synthesis as an expanding, bistable Fisher-KPP wave. Importantly, even in the presence of positive feedback, the reconstituted Ras-PI3Kγ module can only outpace GAP-and PTEN-mediated inhibition when a threshold initial density of Ras(GTP) is achieved, a regulatory mechanism that is mirrored in living systems[142–145]. Additionally, we found that differences in the membrane diffusion coefficients of Ras and PIP_3 molecules influence the spatiotemporal dynamics of positive feedback-dependent traveling waves. We have established a foundation for reconstituting and investigating feedback architecture within membrane-associated signaling reactions. In the future, similar techniques could be applied to studying both positive and negative feedback in systems involving diverse lipid modifying enzymes under various regulatory pressures, Ras- and Rho-family GTPases along with their cognate activators and inhibitors, and actin networks.

Together, the findings described in this dissertation demonstrate the power of bottom-up biochemical reconstitutions for defining the minimal requirements that give rise to complex cellular processes. By isolating individual reactions and regulatory circuits,

this work has clarified fundamental principles of plasma membrane signal transduction and identified potential avenues for therapeutic intervention in pathways frequently dysregulated in human disease.

APPENDIX

SUPPLEMENTARY INFORMATION PERTAINING TO CHAPTERS THREE AND FOUR

*This appendix contains previously published co-authored material.

Doerr, S., Olavarrieta-Colasurdo, A. & Hansen, S. D. Reconstitution of Ras-PI3Kγ membrane communication and feedback using light-induced signaling inputs. In review.

The following experiments were designed and performed by Dr. Scott Hansen, Andrés Olavarrieta-Colasurdo, and Sophia Doerr.

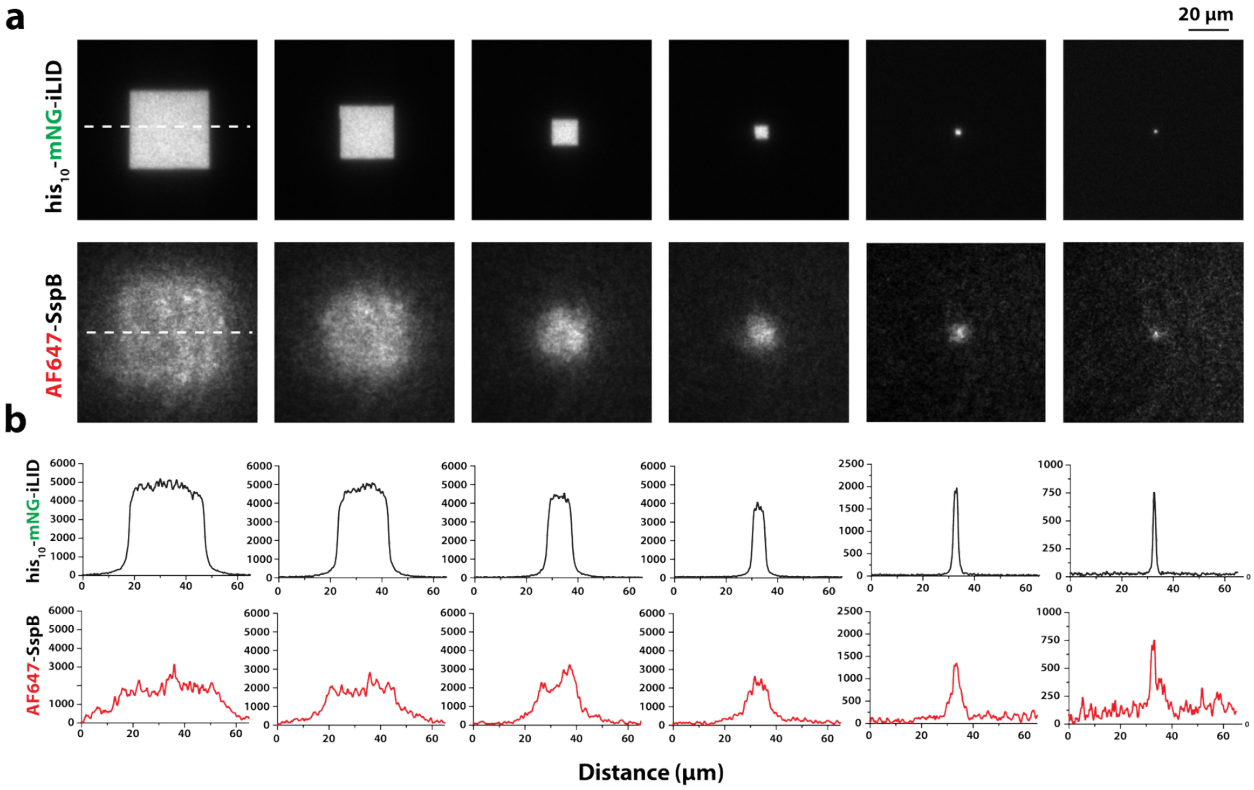

Supplementary Figure 1 SspB membrane recruitment as a function of pattern size
(a) TIRF-M images showing excited his_{10}-mNG-iLID in squares of different side lengths (900, 400, 100, 25, 4, 1 μm^2) on bilayers and corresponding AF647-SspB(micro) membrane localization. **(b)** Line scans showing fluorescence intensity of membrane-tethered his_{10}-mNG-iLID and

membrane-recruited AF647-SspB(micro) 5 seconds after a 488 nm pulse of light. A representative line scan (dashed line) is shown in **(a)**. **(a, b)** Membrane composition: 96% DOPC, 2% NiNTA (+iLID bound), 2% MCC-PE lipids. All experiments contained a solution concentration of 100 nM AF647-SspB(micro).

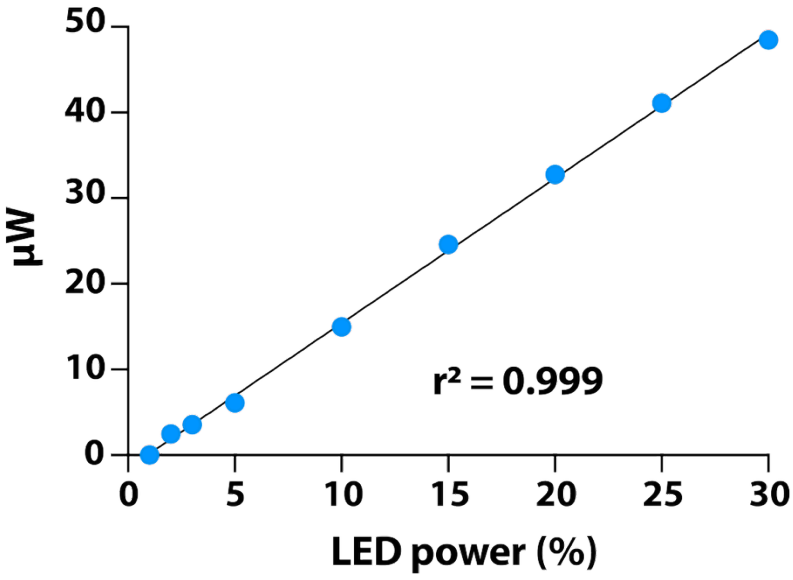

Supplementary Figure 2 Calibration of LED power for iLID activation
Intensity of 488 nm light (µW) measured through a 60x TIRF objective as a function of the LED power (%) from SOLA SE light engine. Intensity was measured using a Newport power meter positioned in place of the glass coverslip. r^2 value represents the coefficient of determination.

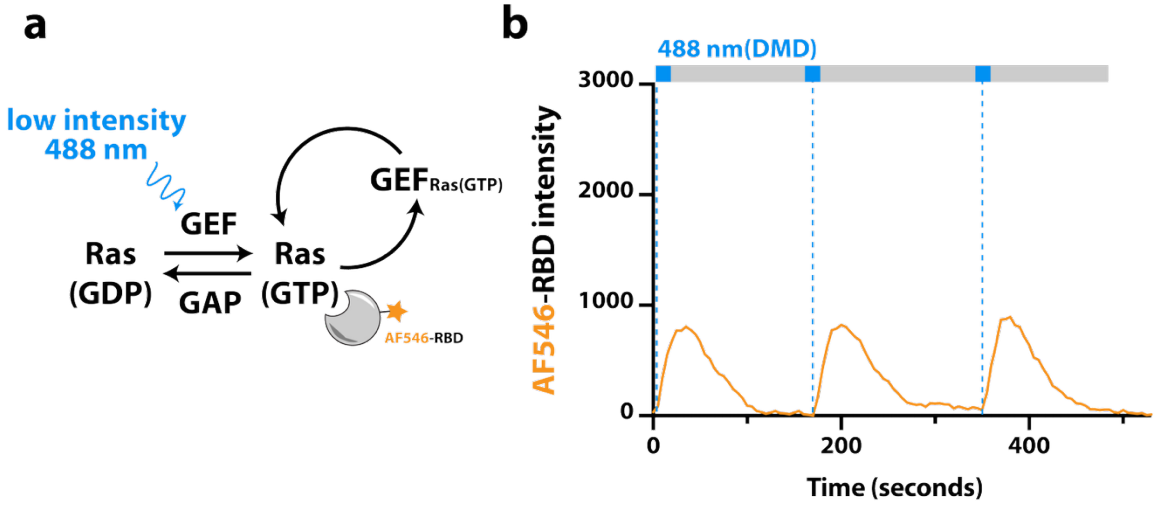

Supplementary Figure 3 Repetitive low light-induced membrane recruitment of GEF-SspB does not trigger Ras(GTP) amplification

(a) Diagram of light-inducible Ras activation module in the presence of low intensity activating light. Global GAP activity prevents Ras activation until light-induced recruitment of GEF-SspB generates a transient pool of Ras(GTP), which can be visualized via an AF546-RBD biosensor. This reaction is amplified by a positive feedback loop mediated by $GEF_{Ras(GTP)}$. **(b)** Time delayed membrane recruitment of AF647-GEF-SspB(micro) does not trigger signal amplification when fold enrichment is too low. Reactions contained 10 nM $GEF_{Ras(GTP)}$, 10 nM AF647-GEF-SspB(micro), 544 nM GAP, and 50 nM AF546-RBD. Membrane composition: 92% DOPC, 2% NiNTA (+iLID bound), 2% MCC-PE (+Ras bound), and 4% PIP_2.

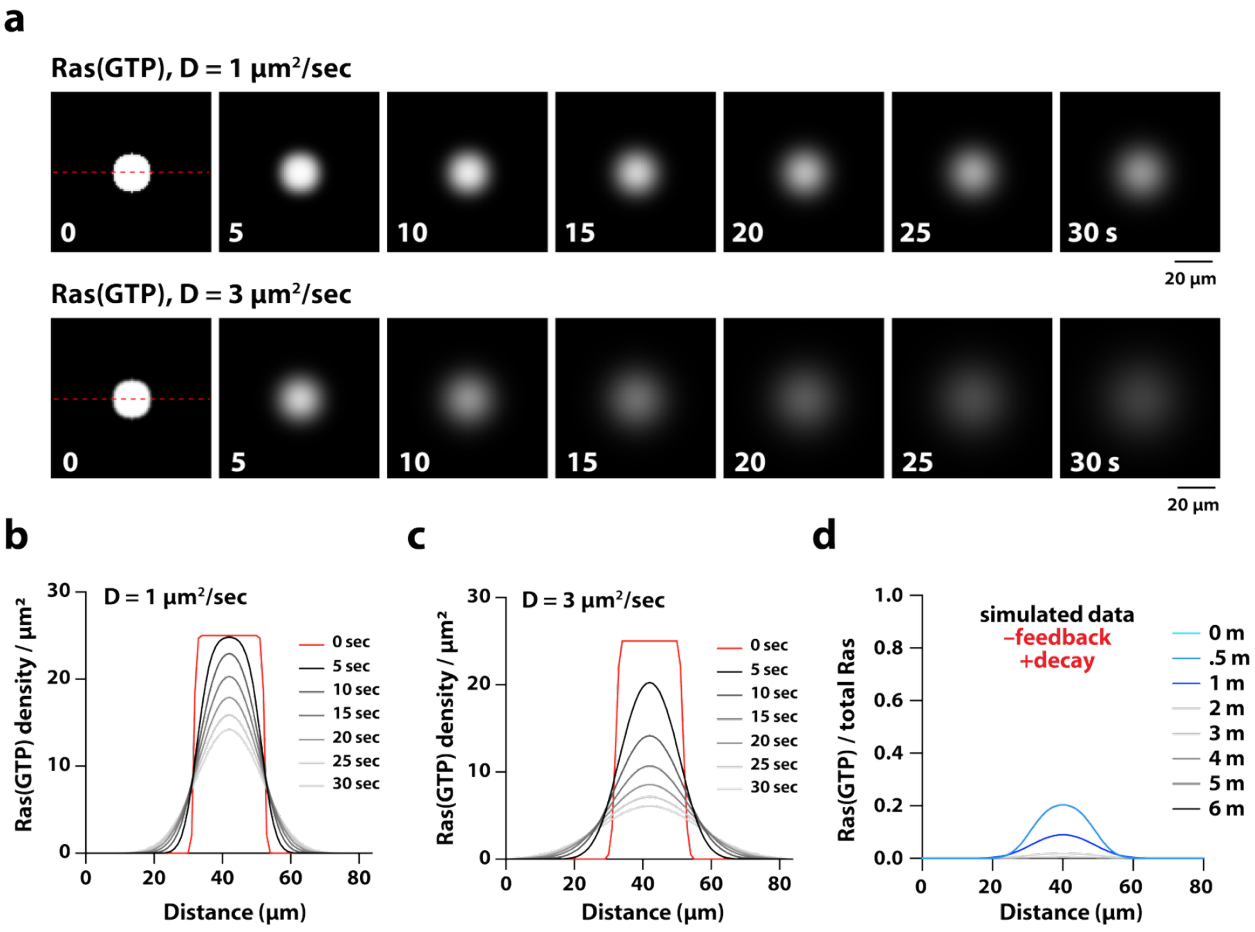

Supplementary Figure 4 Fisher-KPP waves simulated in the absence of logistic growth and GAP-mediated decay

(a) Montages showing the change in Ras(GTP) membrane intensity for Fisher-KPP wave simulations lacking positive feedback and GAP-mediated decay. Reactions were simulated with Ras(GTP) diffusion coefficients (D) of 1 or 3 μm^2/second. Red dashed lines represent the position of line scans plotted below. **(b, c)** The distance Ras(GTP) diffuses from original site of activation as a function of time depends on its diffusion coefficient. Line scans showing the Ras(GTP) membrane density (molecules/μm^2) as a function of the membrane position for simulations performed with **(b)** D = 1 μm^2/second or **(c)** D = 3 μm^2/second. Legends indicate time following

initial Ras activation (solid red line) which seeds 25 Ras(GTP)/μm^2. **(d)** Intensity line scans showing the fraction of locally activated Ras over time for the simulation lacking positive feedback shown in **Fig. 4.3g**.

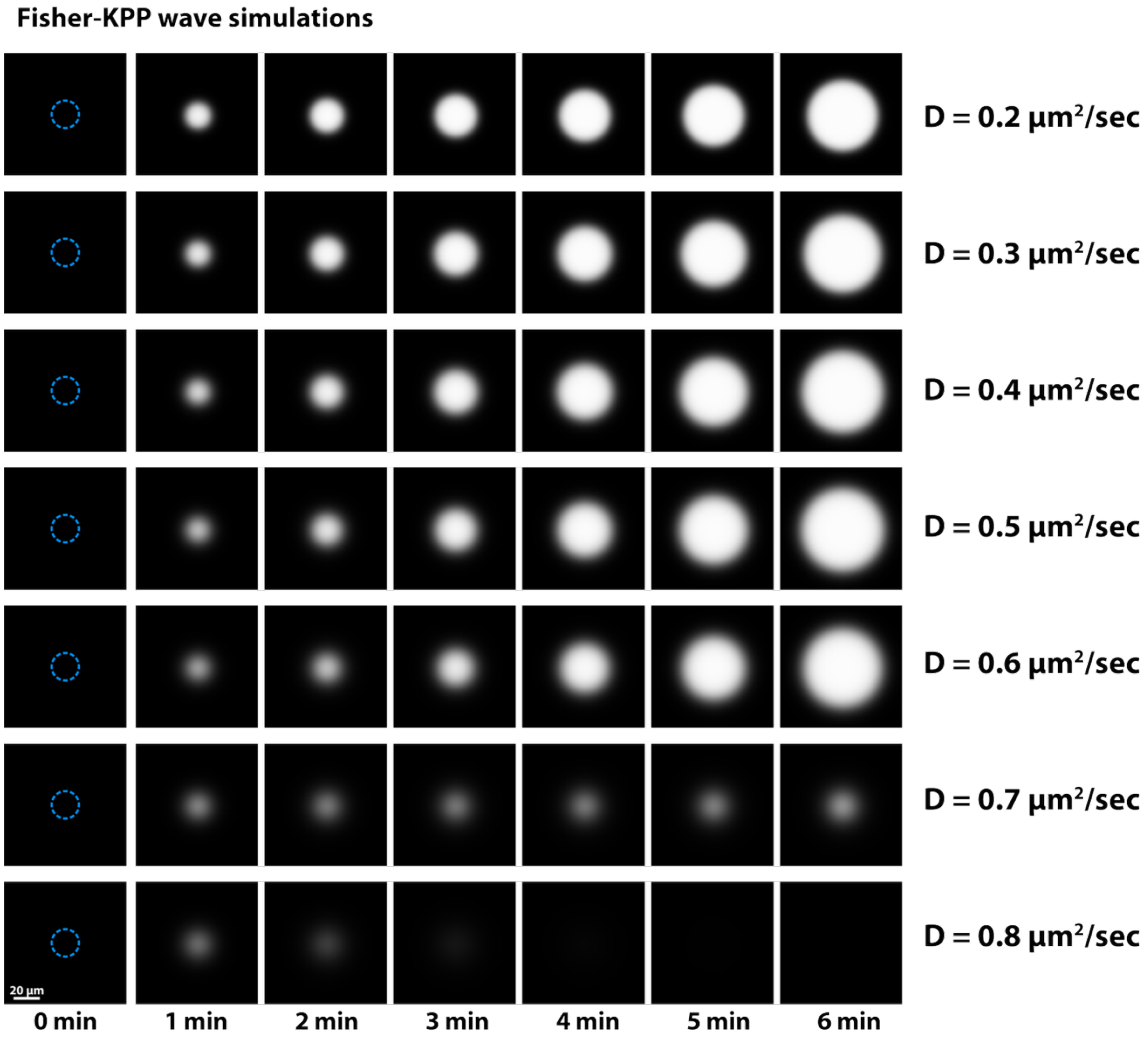

Supplementary Figure 5 Fisher-KPP waves simulated over a range of diffusion coefficients Montages of simulated images obtained using the Fisher-KPP equation with Ras(GTP) diffusion coefficients ranging from 0.2-0.8 μm^2/second. In all other respects, these simulations were identical to the simulation that contained feedback and an experimentally determined activation threshold shown in **Fig. 4.3g, h**.

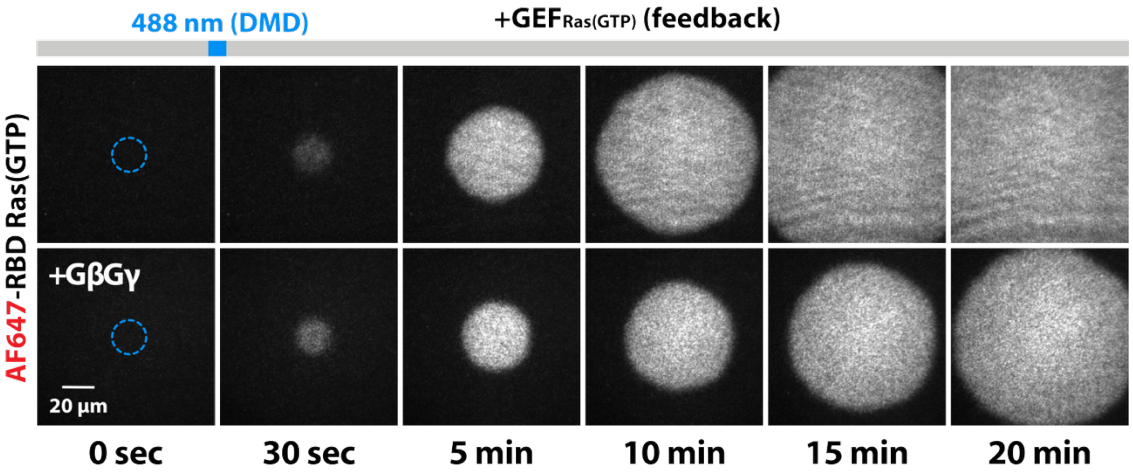

Supplementary Figure 6 Membrane-anchored GβGγ reduces the rate of Ras(GTP) wave expansion

Representative montages showing the time-dependent change in Ras activation following a 488 nm light pulse (blue circle) in the presence of the $GEF_{Ras(GTP)}$-mediated positive feedback loop, 450 nM GAP, and either 0 nM (top) or 25 nM membrane-anchored GβGγ. Membrane composition: 92% DOPC, 2% NiNTA (+iLID bound), 2% MCC-PE (+Ras bound), and 4% PIP_2 lipids, +/-GβGγ-farnesyl. 30% LED power was used for activating light pulses.

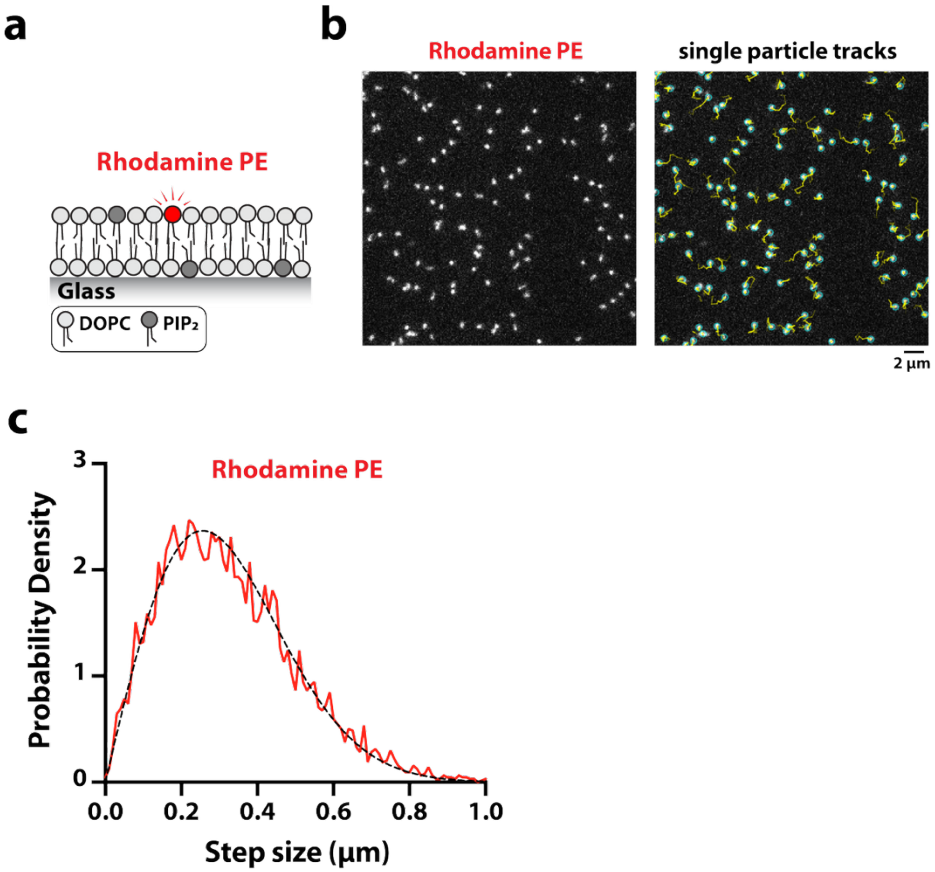

Supplementary Figure 7 Lipid diffusion coefficient measured by single particle tracking **(a)** Experimental design for visualizing Rhodamine PE (Lissamine Rhodamine Phosphatidylethanolamine) diffusion in supported lipid bilayers using single molecule TIRF-M. **(b)** Representative TIRF-M image showing the localization of Rhodamine PE. Single particle detection (light blue circles) and trajectories (fading yellow lines) show dynamic lateral diffusion of lipids. **(c)** Step size distribution based on frame-to-frame single molecule displacements (µm) measured in the presence of 0.00001% molar fraction Rhodamine PE. Dashed black line represents the curve fit used to calculate the diffusion coefficient: D = 2.76 μm^2/second, n = 6361 events.

REFERENCES

1. Balla, T. Phosphoinositides: Tiny Lipids With Giant Impact on Cell Regulation. *Physiological Reviews* **93**, 1019–1137 (2013).
2. Burke, J. E., Triscott, J., Emerling, B. M. & Hammond, G. R. V. Beyond PI3Ks: targeting phosphoinositide kinases in disease. *Nat Rev Drug Discov* **22**, 357–386 (2023).
3. Burke, J. E. Structural Basis for Regulation of Phosphoinositide Kinases and Their Involvement in Human Disease. *Molecular Cell* **71**, 653–673 (2018).
4. Berger, K. L. *et al.* Roles for endocytic trafficking and phosphatidylinositol 4-kinase III alpha in hepatitis C virus replication. *Proc. Natl. Acad. Sci. U.S.A.* **106**, 7577–7582 (2009).
5. Berger, K. L., Kelly, S. M., Jordan, T. X., Tartell, M. A. & Randall, G. Hepatitis C Virus Stimulates the Phosphatidylinositol 4-Kinase III Alpha-Dependent Phosphatidylinositol 4-Phosphate Production That Is Essential for Its Replication. *J Virol* **85**, 8870–8883 (2011).
6. Adhikari, H. *et al.* Oncogenic KRAS is dependent upon an EFR3A-PI4KA signaling axis for potent tumorigenic activity. *Nat Commun* **12**, 5248 (2021).
7. Kattan, W. E. *et al.* Components of the phosphatidylserine endoplasmic reticulum to plasma membrane transport mechanism as targets for KRAS inhibition in pancreatic cancer. *Proc. Natl. Acad. Sci. U.S.A.* **118**, e2114126118 (2021).

8. Chung, J. *et al.* PI4P/phosphatidylserine countertransport at ORP5- and ORP8-mediated ER–plasma membrane contacts. *Science* **349**, 428–432 (2015).
9. Wills, R. C. & Hammond, G. R. V. PI(4,5)P2: signaling the plasma membrane. *Biochemical Journal* **479**, 2311–2325 (2022).
10. Hammond, G. R. V. *et al.* PI4P and PI(4,5)P2 Are Essential But Independent Lipid Determinants of Membrane Identity. *Science* **337**, 727–730 (2012).
11. Stephens, L. R., Hughes, K. T. & Irvine, R. F. Pathway of phosphatidylinositol(3,4,5)-trisphosphate synthesis in activated neutrophils. *Nature* **351**, 33–39 (1991).
12. Servant, G. *et al.* Polarization of Chemoattractant Receptor Signaling During Neutrophil Chemotaxis. *Science* **287**, 1037–1040 (2000).
13. Fivaz, M., Bandara, S., Inoue, T. & Meyer, T. Robust Neuronal Symmetry Breaking by Ras-Triggered Local Positive Feedback. *Current Biology* **18**, 44–50 (2008).
14. Sasaki, A. T. *et al.* G protein–independent Ras/PI3K/F-actin circuit regulates basic cell motility. *The Journal of Cell Biology* **178**, 185–191 (2007).
15. Brandman, O. & Meyer, T. Feedback Loops Shape Cellular Signals in Space and Time. *Science* **322**, 390–395 (2008).
16. Burke, J. E. & Williams, R. L. Synergy in activating class I PI3Ks. *Trends in Biochemical Sciences* **40**, 88–100 (2015).
17. Lee, Y.-R., Chen, M. & Pandolfi, P. P. The functions and regulation of the PTEN tumour suppressor: new modes and prospects. *Nat Rev Mol Cell Biol* **19**, 547–562 (2018).

18. Kolch, W., Berta, D. & Rosta, E. Dynamic regulation of RAS and RAS signaling. *Biochemical Journal* **480**, 1–23 (2023).
19. Cherfils, J. & Zeghouf, M. Regulation of Small GTPases by GEFs, GAPs, and GDIs. *Physiological Reviews* **93**, 269–309 (2013).
20. Suire, S. *et al.* GPCR activation of Ras and PI3Kγ in neutrophils depends on PLCβ2/β3 and the RasGEF RasGRP4: PI3Kγ regulation by a PLCβ/RasGRP4/Ras pathway. *The EMBO Journal* **31**, 3118–3129 (2012).
21. Iwamoto, K., Matsuoka, S. & Ueda, M. Excitable Ras dynamics-based screens reveal RasGEFX is required for macropinocytosis and random cell migration. *Nat Commun* **16**, 117 (2025).
22. Toettcher, J. E., Weiner, O. D. & Lim, W. A. Using Optogenetics to Interrogate the Dynamic Control of Signal Transmission by the Ras/Erk Module. *Cell* **155**, 1422–1434 (2013).
23. Hoeller, O., Gong, D. & Weiner, O. D. How to Understand and Outwit Adaptation. *Developmental Cell* **28**, 607–616 (2014).
24. Devreotes, P. N. *et al.* Excitable Signal Transduction Networks in Directed Cell Migration. *Annu. Rev. Cell Dev. Biol.* **33**, 103–125 (2017).
25. Doerr, S., Olavarrieta-Colasurdo, A. & Hansen, S. D. Reconstitution of Ras-PI3Kγ membrane communication and feedback using light-induced signaling inputs. *BioRxiv* (2026).

26. Margarit, S. M. *et al.* Structural Evidence for Feedback Activation by Ras·GTP of the Ras-Specific Nucleotide Exchange Factor SOS. *Cell* **112**, 685–695 (2003).
27. Nakamura, Y., Hibino, K., Yanagida, T. & Sako, Y. Switching of the positive feedback for RAS activation by a concerted function of SOS membrane association domains. *BIOPHYSICS* **13**, 1–11 (2016).
28. Yang, H. W. *et al.* Cooperative Activation of PI3K by Ras and Rho Family Small GTPases. *Molecular Cell* **47**, 281–290 (2012).
29. Müller, P. M. *et al.* Systems analysis of RhoGEF and RhoGAP regulatory proteins reveals spatially organized RAC1 signalling from integrin adhesions. *Nat Cell Biol* **22**, 498–511 (2020).
30. Hansen, S. D. *et al.* Stochastic geometry sensing and polarization in a lipid kinase–phosphatase competitive reaction. *Proc. Natl. Acad. Sci. U.S.A.* **116**, 15013–15022 (2019).
31. Huang, W. Y. C. *et al.* Phosphotyrosine-mediated LAT assembly on membranes drives kinetic bifurcation in recruitment dynamics of the Ras activator SOS. *Proc. Natl. Acad. Sci. U.S.A.* **113**, 8218–8223 (2016).
32. Ziemba, B. P., Burke, J. E., Masson, G., Williams, R. L. & Falke, J. J. Regulation of PI3K by PKC and MARCKS: Single-Molecule Analysis of a Reconstituted Signaling Pathway. *Biophysical Journal* **110**, 1811–1825 (2016).
33. Iversen, L. *et al.* Ras activation by SOS: Allosteric regulation by altered fluctuation dynamics. *Science* **345**, 50–54 (2014).

34. Veggiani, G., Zakeri, B. & Howarth, M. Superglue from bacteria: unbreakable bridges for protein nanotechnology. *Trends in Biotechnology* **32**, 506–512 (2014).
35. Guntas, G. *et al.* Engineering an improved light-induced dimer (iLID) for controlling the localization and activity of signaling proteins. *Proc. Natl. Acad. Sci. U.S.A.* **112**, 112–117 (2015).
36. Zimmerman, S. P. *et al.* Tuning the Binding Affinities and Reversion Kinetics of a Light Inducible Dimer Allows Control of Transmembrane Protein Localization. *Biochemistry* **55**, 5264–5271 (2016).
37. Hammond, G. R. V. & Burke, J. E. Novel roles of phosphoinositides in signaling, lipid transport, and disease. *Current Opinion in Cell Biology* **63**, 57–67 (2020).
38. Vadas, O., Burke, J. E., Zhang, X., Berndt, A. & Williams, R. L. Structural Basis for Activation and Inhibition of Class I Phosphoinositide 3-Kinases. *Sci. Signal.* **4**, (2011).
39. Mognol, G. P., Ghebremedhin, A. & Varner, J. A. Targeting PI3Kγ in cancer. *Trends in Cancer* https://linkinghub.elsevier.com/retrieve/pii/S2405803325000093 (2025).
40. Nürnberg, B. & Beer-Hammer, S. Function, Regulation and Biological Roles of PI3Kγ Variants. *Biomolecules* **9**, 427 (2019).
41. Lees, J. A. *et al.* Architecture of the human PI4KIIIα lipid kinase complex. *Proc. Natl. Acad. Sci. U.S.A.* **114**, 13720–13725 (2017).
42. Dornan, G. L. *et al.* Probing the Architecture, Dynamics, and Inhibition of the PI4KIIIα/TTC7/FAM126 Complex. *Journal of Molecular Biology* **430**, 3129–3142 (2018).

43. Baskin, J. M. *et al.* The leukodystrophy protein FAM126A (hyccin) regulates PtdIns(4)P synthesis at the plasma membrane. *Nat Cell Biol* **18**, 132–138 (2016).
44. Bojjireddy, N. *et al.* Pharmacological and Genetic Targeting of the PI4KA Enzyme Reveals Its Important Role in Maintaining Plasma Membrane Phosphatidylinositol 4-Phosphate and Phosphatidylinositol 4,5-Bisphosphate Levels. *Journal of Biological Chemistry* **289**, 6120–6132 (2014).
45. Suresh, S. *et al.* Molecular basis for plasma membrane recruitment of PI4KA by EFR3. *S c i e n c e A d v a n c e s* (2024).
46. Suresh, S. *et al.* Development of an inhibitory TTC7B selective nanobody that blocks EFR3 recruitment of PI4KA. *Journal of Biological Chemistry* **301**, 110886 (2025).
47. Zara, F. *et al.* Deficiency of hyccin, a newly identified membrane protein, causes hypomyelination and congenital cataract. *Nat Genet* **38**, 1111–1113 (2006).
48. Gazzerro, E. *et al.* Hyccin, the Molecule Mutated in the Leukodystrophy Hypomyelination and Congenital Cataract (HCC), Is a Neuronal Protein. *PLoS ONE* **7**, e32180 (2012).
49. Barlow-Busch, I., Shaw, A. L. & Burke, J. E. PI4KA and PIKfyve: Essential phosphoinositide signaling enzymes involved in myriad human diseases. *Current Opinion in Cell Biology* **83**, 102207 (2023).
50. Suresh, S. & Burke, J. E. Structural basis for the conserved roles of PI4KA and its regulatory partners and their misregulation in disease. *Advances in Biological Regulation* **90**, 100996 (2023).

51. Chen, R. *et al.* Whole-exome sequencing identifies tetratricopeptide repeat domain 7A (TTC7A) mutations for combined immunodeficiency with intestinal atresias. *Journal of Allergy and Clinical Immunology* **132**, 656-664.e17 (2013).
52. Agarwal, N. S. *et al.* Tetratricopeptide Repeat Domain 7A (TTC7A) Mutation in a Newborn with Multiple Intestinal Atresia and Combined Immunodeficiency. *J Clin Immunol* **34**, 607–610 (2014).
53. Yang, W. *et al.* Compound heterozygous mutations in TTC7A cause familial multiple intestinal atresias and severe combined immunodeficiency. *Clinical Genetics* **88**, 542–549 (2015).
54. Jardine, S., Dhingani, N. & Muise, A. M. TTC7A: Steward of Intestinal Health. *Cellular and Molecular Gastroenterology and Hepatology* **7**, 555–570 (2019).
55. Biancheri, R. *et al.* Hypomyelination and Congenital Cataract: Broadening the Clinical Phenotype. *Arch Neurol* **68**, 1191 (2011).
56. Waring, M. J. *et al.* Potent, selective small molecule inhibitors of type III phosphatidylinositol-4-kinase α- but not β- inhibit the phosphatidylinostiol signaling cascade and cancer cell proliferation. (2014).
57. Fischer, B. *et al.* Allosteric nanobodies to study the interactions between SOS1 and RAS. *Nat Commun* **15**, 6214 (2024).
58. Rathinaswamy, M. K. *et al.* Structure of the phosphoinositide 3-kinase (PI3K) p110γ-p101 complex reveals molecular mechanism of GPCR activation. *Sci. Adv.* **7**, eabj4282 (2021).

59. Hamers-Casterman, C. *et al.* Naturally occurring antibodies devoid of light chains. *Nature* **363**, 446–448 (1993).

60. Jin, B., Odongo, S., Radwanska, M. & Magez, S. NANOBODIES®: A Review of Diagnostic and Therapeutic Applications. *IJMS* **24**, 5994 (2023).

61. Xǔ, X. J., Tong, C. S. & Wu, M. Distinct impact of PI(4)P flux on PI(4,5)P2 steady states and oscillations. *Proc. Natl. Acad. Sci. U.S.A.* **123**, e2518354123 (2026).

62. Ulengin-Talkish, I. *et al.* Palmitoylation targets the calcineurin phosphatase to the phosphatidylinositol 4-kinase complex at the plasma membrane. *Nat Commun* **12**, 6064 (2021).

63. Shaw, A. L. *et al.* Structure of calcineurin bound to PI4KA reveals dual interface in both PI4KA and FAM126A. *Structure* **32**, 1973-1983.e6 (2024).

64. Guo, P. *et al.* PI4P-mediated solid-like Merlin condensates orchestrate Hippo pathway regulation. *Science* **385**, eadf4478 (2024).

65. Hornbeck, P. V. *et al.* PhosphoSitePlus, 2014: mutations, PTMs and recalibrations. *Nucleic Acids Research* **43**, D512–D520 (2015).

66. Johnson, J. L. *et al.* An atlas of substrate specificities for the human serine/threonine kinome. *Nature* **613**, 759–766 (2023).

67. Yaron-Barir, T. M. *et al.* The intrinsic substrate specificity of the human tyrosine kinome. *Nature* **629**, 1174–1181 (2024).

68. Miller, S. *et al.* Shaping Development of Autophagy Inhibitors with the Structure of the Lipid Kinase Vps34. *Science* **327**, 1638–1642 (2010).

69. Burke, J. E. *et al.* Structures of PI4KIIIβ complexes show simultaneous recruitment of Rab11 and its effectors. *Science* **344**, 1035–1038 (2014).
70. Shaw, A. L., Barlow-Busch, I. & Burke, J. E. Molecular basis for regulation of the class I phosphoinositide 3-kinases (PI3Ks), and their targeting in human disease. *Biochimica et Biophysica Acta (BBA) - Molecular and Cell Biology of Lipids* **1870**, 159689 (2025).
71. Torosyan, H. *et al.* Structures of the PI3Kα/KRas complex on lipid bilayers reveal the molecular mechanism of PI3Kα activation. *BioRxiv* (2025).
72. Rathinaswamy, M. K. *et al.* Disease-related mutations in PI3Kγ disrupt regulatory C-terminal dynamics and reveal a path to selective inhibitors. *eLife* **10**, e64691 (2021).
73. Czupalla, C. *et al.* Identification and Characterization of the Autophosphorylation Sites of Phosphoinositide 3-Kinase Isoforms β and γ. *Journal of Biological Chemistry* **278**, 11536–11545 (2003).
74. Vanhaesebroeck, B. *et al.* Autophosphorylation of p110δ phosphoinositide 3-kinase: a new paradigm for the regulation of lipid kinases in vitro and in vivo. (1999).
75. Lin, T.-Y. *et al.* Epinephrine inhibits PI3K alpha via the Hippo kinases. *Cell Reports* (2023).
76. Pacold, M. E. *et al.* Crystal Structure and Functional Analysis of Ras Binding to Its Effector Phosphoinositide 3-Kinase ✐. 14 (2000).
77. Rynkiewicz, N. K. *et al.* Gβγ is a direct regulator of endogenous p101/p110γ and p84/p110γ PI3Kγ complexes in mouse neutrophils. *Sci. Signal.* **13**, eaaz4003 (2020).

78. Vadas, O. *et al.* Molecular determinants of PI3Kγ-mediated activation downstream of G-protein–coupled receptors (GPCRs). *Proc. Natl. Acad. Sci. U.S.A.* **110**, 18862–18867 (2013).

79. Castellano, E. & Downward, J. RAS Interaction with PI3K: More Than Just Another Effector Pathway. *Genes & Cancer* **2**, 261–274 (2011).

80. Takeda, A. J. *et al.* Human PI3Kγ deficiency and its microbiota-dependent mouse model reveal immunodeficiency and tissue immunopathology. *Nat Commun* **10**, 4364 (2019).

81. Marini Thian *et al.* Germline biallelic PIK3CG mutations in a multifaceted immunodeficiency with immune dysregulation. *haematol* **105**, e488 (2020).

82. Deladeriere, A. *et al.* The regulatory subunits of PI3Kγ control distinct neutrophil responses. *Sci. Signal.* **8**, (2015).

83. Sasaki, A. T., Chun, C., Takeda, K. & Firtel, R. A. Localized Ras signaling at the leading edge regulates PI3K, cell polarity, and directional cell movement. *Journal of Cell Biology* **167**, 505–518 (2004).

84. Gangadhara, G. *et al.* A class of highly selective inhibitors bind to an active state of PI3Kγ. *Nat Chem Biol* **15**, 348–357 (2019).

85. Iijima, M. & Devreotes, P. Tumor Suppressor PTEN Mediates Sensing of Chemoattractant Gradients. *Cell* **109**, 599–610 (2002).

86. Nguyen, H.-N. *et al.* Engineering ePTEN, an enhanced PTEN with increased tumor suppressor activities. *Proc. Natl. Acad. Sci. U.S.A.* **111**, (2014).

87. McMahon, C. *et al.* Yeast surface display platform for rapid discovery of conformationally selective nanobodies. *Nat Struct Mol Biol* **25**, 289–296 (2018).
88. Zakeri, B. *et al.* Peptide tag forming a rapid covalent bond to a protein, through engineering a bacterial adhesin. *Proc. Natl. Acad. Sci. U.S.A.* **109**, (2012).
89. Shaw, A. L. *et al.* Phosphorylation of the C-terminus of PI4KA inhibits lipid kinase activity. *BioRxiv* (2026).
90. Shah, N. H., Löbel, M., Weiss, A. & Kuriyan, J. Fine-tuning of substrate preferences of the Src-family kinase Lck revealed through a high-throughput specificity screen. *eLife* **7**, e35190 (2018).
91. Prasad, K. V. S. *et al.* Phosphatidylinositol (PI) 3-Kinase and PI 4-Kinase Binding to the CD4-p56lck Complex: the p56lck SH3 Domain Binds to PI 3-Kinase but Not PI 4-Kinase. *MOL. CELL. BIOL.* **13**, (1993).
92. Trono, P., Ottavi, F. & Rosano', L. Novel insights into the role of Discoidin domain receptor 2 (DDR2) in cancer progression: a new avenue of therapeutic intervention. *Matrix Biology* **125**, 31–39 (2024).
93. Su, H. & Karin, M. Multifaceted collagen-DDR1 signaling in cancer. *Trends in Cell Biology* **34**, 406–415 (2024).
94. Voena, C., Ambrogio, C., Iannelli, F. & Chiarle, R. ALK in cancer: from function to therapeutic targeting. *Nat Rev Cancer* **25**, 359–378 (2025).

95. Hammond, G. R. V., Machner, M. P. & Balla, T. A novel probe for phosphatidylinositol 4-phosphate reveals multiple pools beyond the Golgi. *Journal of Cell Biology* **205**, 113–126 (2014).

96. Rathinaswamy, M. K. *et al.* Molecular basis for differential activation of p101 and p84 complexes of PI3Kγ by Ras and GPCRs. *Cell Reports* **42**, 112172 (2023).

97. Nakatsu, F. *et al.* PtdIns4P synthesis by PI4KIIIα at the plasma membrane and its impact on plasma membrane identity. *Journal of Cell Biology* **199**, 1003–1016 (2012).

98. Beghein, E. & Gettemans, J. Nanobody Technology: A Versatile Toolkit for Microscopic Imaging, Protein–Protein Interaction Analysis, and Protein Function Exploration. *Front. Immunol.* **8**, 771 (2017).

99. Koenig, P.-A. *et al.* Structure-guided multivalent nanobodies block SARS-CoV-2 infection and suppress mutational escape. *Science* **371**, eabe6230 (2021).

100. Wu, X. *et al.* Structural Insights into Assembly and Regulation of the Plasma Membrane Phosphatidylinositol 4-Kinase Complex. *Developmental Cell* **28**, 19–29 (2014).

101. Koester, A. M. *et al.* EFR3 and phosphatidylinositol 4-kinase IIIα regulate insulin-stimulated glucose transport and GLUT4 dispersal in 3T3-L1 adipocytes. *Bioscience Reports* **42**, BSR20221181 (2022).

102. Fowler, M. L. *et al.* Using hydrogen deuterium exchange mass spectrometry to engineer optimized constructs for crystallization of protein complexes: Case study of PI4KIIIβ with Rab11. *Protein Science* **25**, 826–839 (2016).

103. Zhang, X. *et al.* Structure of Lipid Kinase p110β/p85β Elucidates an Unusual SH2-Domain-Mediated Inhibitory Mechanism. *Molecular Cell* **41**, 567–578 (2011).

104. Hon, W.-C., Berndt, A. & Williams, R. L. Regulation of lipid binding underlies the activation mechanism of class IA PI3-kinases. *Oncogene* **31**, 3655–3666 (2012).

105. Cook, A. S. I. *et al.* Structural pathway for PI3-kinase regulation by VPS15 in autophagy. *Science* eadl3787 (2025).

106. Suire, S. *et al.* Gβγs and the Ras binding domain of p110γ are both important regulators of PI3Kγ signalling in neutrophils. *Nat Cell Biol* **8**, 1303–1309 (2006).

107. Das, B. *et al.* Control of Intramolecular Interactions between the Pleckstrin Homology and Dbl Homology Domains of Vav and Sos1 Regulates Rac Binding. *Journal of Biological Chemistry* **275**, 15074–15081 (2000).

108. Yin, J., Lin, A. J., Golan, D. E. & Walsh, C. T. Site-specific protein labeling by Sfp phosphopantetheinyl transferase. *Nat Protoc* **1**, 280–285 (2006).

109. Hansen, S. D., Lee, A. A., Duewell, B. R. & Groves, J. T. Membrane-mediated dimerization potentiates PIP5K lipid kinase activity. *eLife* **11**, e73747 (2022).

110. Duewell, B. R., Wilson, N. E., Bailey, G. M., Peabody, S. E. & Hansen, S. D. Molecular dissection of PI3Kβ synergistic activation by receptor tyrosine kinases, GβGγ, and Rho-family GTPases. *eLife* **12**, RP88991 (2024).

111. Lee, Y. K. *et al.* Mechanism of SOS PR-domain autoinhibition revealed by single-molecule assays on native protein from lysate. *Nat Commun* **8**, 15061 (2017).

112. Sondermann, H. *et al.* Structural Analysis of Autoinhibition in the Ras Activator Son of Sevenless. *Cell* **119**, 393–405 (2004).

113. Jaqaman, K. *et al.* Robust single-particle tracking in live-cell time-lapse sequences. *Nat Methods* **5**, 695–702 (2008).

114. Schindelin, J. *et al.* Fiji: an open-source platform for biological-image analysis. *Nat Methods* **9**, 676–682 (2012).

115. Armstrong, M. C. *et al.* The biochemical mechanism of Rho GTPase membrane binding, activation and retention in activity patterning. *EMBO J* **44**, 2620–2657 (2025).

116. Lee, A. A. *et al.* Bimodality in Ras signaling originates from processivity of the Ras activator SOS without deterministic bistability. *Sci. Adv.* **10**, eadi0707 (2024).

117. Plowman, S. J., Muncke, C., Parton, R. G. & Hancock, J. F. H-ras, K-ras, and inner plasma membrane raft proteins operate in nanoclusters with differential dependence on the actin cytoskeleton. *Proc. Natl. Acad. Sci. U.S.A.* **102**, 15500–15505 (2005).

118. Prior, I. A., Muncke, C., Parton, R. G. & Hancock, J. F. Direct visualization of Ras proteins in spatially distinct cell surface microdomains. *The Journal of Cell Biology* **160**, 165–170 (2003).

119. Coyle, S. M. & Lim, W. A. Mapping the functional versatility and fragility of Ras GTPase signaling circuits through in vitro network reconstitution. *eLife* **5**, e12435 (2016).

120. Ferrell, J. E. & Machleder, E. M. The Biochemical Basis of an All-or-None Cell Fate Switch in *Xenopus* Oocytes. *Science* **280**, 895–898 (1998).

121. Wang, F. The Signaling Mechanisms Underlying Cell Polarity and Chemotaxis. *Cold Spring Harbor Perspectives in Biology* **1**, a002980–a002980 (2009).

122. Goglia, A. G. & Toettcher, J. E. A bright future: optogenetics to dissect the spatiotemporal control of cell behavior. *Current Opinion in Chemical Biology* **48**, 106–113 (2019).

123. Natwick, D. E. & Collins, S. R. Optimized iLID Membrane Anchors for Local Optogenetic Protein Recruitment. *ACS Synth. Biol.* **10**, 1009–1023 (2021).

124. Mahlandt, E. K. *et al.* Opto-RhoGEFs, an optimized optogenetic toolbox to reversibly control Rho GTPase activity on a global to subcellular scale, enabling precise control over vascular endothelial barrier strength. *eLife* **12**, RP84364 (2023).

125. Town, J. P. & Weiner, O. D. Local negative feedback of Rac activity at the leading edge underlies a pilot pseudopod-like program for amoeboid cell guidance. *PLoS Biol* **21**, e3002307 (2023).

126. Johnson, H. E. *et al.* The Spatiotemporal Limits of Developmental Erk Signaling. *Developmental Cell* **40**, 185–192 (2017).

127. Murakoshi, H. *et al.* Single-molecule imaging analysis of Ras activation in living cells. *Proc. Natl. Acad. Sci. U.S.A.* **101**, 7317–7322 (2004).

128. Hein, M. Y. *et al.* A Human Interactome in Three Quantitative Dimensions Organized by Stoichiometries and Abundances. *Cell* **163**, 712–723 (2015).

129. Cho, N. H. *et al.* OpenCell: Endogenous tagging for the cartography of human cellular organization. *Science* **375**, eabi6983 (2022).

130. Kramer, B. A., Sarabia del Castillo, J. & Pelkmans, L. Multimodal perception links cellular state to decision-making in single cells. *Science* **377**, 642–648 (2022).

131. Uroz, M. *et al.* Regulation of cell cycle progression by cell–cell and cell–matrix forces. *Nat Cell Biol* **20**, 646–654 (2018).

132. Valon, L., Marín-Llauradó, A., Wyatt, T., Charras, G. & Trepat, X. Optogenetic control of cellular forces and mechanotransduction. *Nat Commun* **8**, 14396 (2017).

133. Fielmich, L.-E., Schmidt, R., Dickinson, D. J., Goldstein, B. & Akhmanova, A. Optogenetic dissection of mitotic spindle positioning in vivo.

134. Yamamoto, K. *et al.* Optogenetic relaxation of actomyosin contractility uncovers mechanistic roles of cortical tension during cytokinesis. *Nat Commun* **12**, 7145 (2021).

135. Yamamoto, K. & Miyazaki, M. Optogenetic actin network assembly on lipid bilayer uncovers the network density-dependent functions of actin-binding proteins. *Nature Communications* (2025).

136. Van Bergeijk, P., Adrian, M., Hoogenraad, C. C. & Kapitein, L. C. Optogenetic control of organelle transport and positioning. *Nature* **518**, 111–114 (2015).

137. Huang, W. Y. C. *et al.* A molecular assembly phase transition and kinetic proofreading modulate Ras activation by SOS. *Science* **363**, 1098–1103 (2019).

138. Natwick, D. E. & Collins, S. R. Optimized iLID Membrane Anchors for Local Optogenetic Protein Recruitment. *ACS Synth. Biol.* **10**, 1009–1023 (2021).

139. Weiner, O. D. *et al.* A PtdInsP3- and Rho GTPase-mediated positive feedback loop regulates neutrophil polarity. *Nat Cell Biol* **4**, 509–513 (2002).

140. Chau, A. H., Walter, J. M., Gerardin, J., Tang, C. & Lim, W. A. Designing Synthetic Regulatory Networks Capable of Self-Organizing Cell Polarization. *Cell* **151**, 320–332 (2012).

141. Tyson, J. J., Chen, K. C. & Novak, B. Sniffers, buzzers, toggles and blinkers: dynamics of regulatory and signaling pathways in the cell. *Current Opinion in Cell Biology* **15**, 221–231 (2003).

142. Manz, B. N., Jackson, B. L., Petit, R. S., Dustin, M. L. & Groves, J. T-cell triggering thresholds are modulated by the number of antigen within individual T-cell receptor clusters. *Proc. Natl. Acad. Sci. U.S.A.* **108**, 9089–9094 (2011).

143. Iglesias, P. A. & Devreotes, P. N. Biased excitable networks: how cells direct motion in response to gradients. *Current Opinion in Cell Biology* **24**, 245–253 (2012).

144. Albeck, J. G., Mills, G. B. & Brugge, J. S. Frequency-Modulated Pulses of ERK Activity Transmit Quantitative Proliferation Signals. *Molecular Cell* **49**, 249–261 (2013).

145. Bugaj, L. J. *et al.* Cancer mutations and targeted drugs can disrupt dynamic signal encoding by the Ras-Erk pathway. *Science* **361**, eaao3048 (2018).

146. Deneke, V. E. & Di Talia, S. Chemical waves in cell and developmental biology. *Journal of Cell Biology* **217**, 1193–1204 (2018).

147. Iversen, L. *et al.* Ras activation by SOS: Allosteric regulation by altered fluctuation dynamics. *Science* **345**, 50–54 (2014).

148. Nimnual, A. S., Yatsula, B. A. & Bar-Sagi, D. Coupling of Ras and Rac Guanosine Triphosphatases Through the Ras Exchanger Sos. *Science* **279**, 560–563 (1998).

149. Graziano, B. R. *et al.* A module for Rac temporal signal integration revealed with optogenetics. *Journal of Cell Biology* **216**, 2515–2531 (2017).

150. Welch, H. C. E. *et al.* P-Rex1, a PtdIns(3,4,5)P3- and Gbetagamma-Regulated Guanine-Nucleotide Exchange Factor for Rac. *Cell* **108**, 809–821 (2002).

151. Côté, J.-F., Motoyama, A. B., Bush, J. A. & Vuori, K. A novel and evolutionarily conserved PtdIns(3,4,5)P3-binding domain is necessary for DOCK180 signalling. *Nat Cell Biol* **7**, 797–807 (2005).

152. Nishikimi, A. *et al.* Sequential Regulation of DOCK2 Dynamics by Two Phospholipids During Neutrophil Chemotaxis. *Science* **324**, 384–387 (2009).

153. Premkumar, L. *et al.* Structural Basis of Membrane Targeting by the Dock180 Family of Rho Family Guanine Exchange Factors (Rho-GEFs). *Journal of Biological Chemistry* **285**, 13211–13222 (2010).

154. Srinivasan, S. *et al.* Rac and Cdc42 play distinct roles in regulating PI(3,4,5)P3 and polarity during neutrophil chemotaxis. *Journal of Cell Biology* **160**, 375–385 (2003).

155. Oikawa, T. *et al.* PtdIns(3,4,5)P3 binding is necessary for WAVE2-induced formation of lamellipodia. *Nat Cell Biol* **6**, 420–426 (2004).

156. Inoue, T. & Meyer, T. Synthetic Activation of Endogenous PI3K and Rac Identifies an AND-Gate Switch for Cell Polarization and Migration. *PLoS ONE* **3**, e3068 (2008).

157. Wang, F. *et al.* Lipid products of PI(3)Ks maintain persistent cell polarity and directed motility in neutrophils. *Nat Cell Biol* **4**, 513–518 (2002).

158. Hoeller, O. *et al.* Two distinct functions for PI3-kinases in macropinocytosis. *Journal of Cell Science* jcs.134015 (2013).

159. Gimple, R. C. & Wang, X. RAS: Striking at the Core of the Oncogenic Circuitry. *Front. Oncol.* **9**, 965 (2019).

160. Scheffzek, K. *et al.* The Ras-RasGAP Complex: Structural Basis for GTPase Activation and Its Loss in Oncogenic Ras Mutants. *Science* **277**, 333–339 (1997).

161. Ratner, N. & Miller, S. J. A RASopathy gene commonly mutated in cancer: the neurofibromatosis type 1 tumour suppressor. *Nat Rev Cancer* **15**, 290–301 (2015).

162. Nissan, M. H. *et al.* Loss of NF1 in Cutaneous Melanoma Is Associated with RAS Activation and MEK Dependence. *Cancer Research* **74**, 2340–2350 (2014).

163. De Belly, H. *et al.* Cell protrusions and contractions generate long-range membrane tension propagation. *Cell* **186**, 3049-3061.e15 (2023).

164. Houk, A. R. *et al.* Membrane Tension Maintains Cell Polarity by Confining Signals to the Leading Edge during Neutrophil Migration. *Cell* **148**, 175–188 (2012).

165. Ma, W., Trusina, A., El-Samad, H., Lim, W. A. & Tang, C. Defining Network Topologies that Can Achieve Biochemical Adaptation. *Cell* **138**, 760–773 (2009).

166. Rincón, E., Rocha-Gregg, B. L. & Collins, S. R. A map of gene expression in neutrophil-like cell lines. *BMC Genomics* **19**, 573 (2018).

167. Belliveau, N. M. *et al.* Whole-genome screens reveal regulators of differentiation state and context-dependent migration in human neutrophils. *Nat Commun* **14**, 5770 (2023).

168. Xu, X. *et al.* GPCR-controlled membrane recruitment of negative regulator C2GAP1 locally inhibits Ras signaling for adaptation and long-range chemotaxis. *Proc. Natl. Acad. Sci. U.S.A.* **114**, (2017).

169. Lockyer, P. J. *et al.* Identification of the Ras GTPase-activating protein GAP1m as a phosphatidylinositol-3,4,5-trisphosphate-binding protein in vivo. *Current Biology* **9**, 265–269 (1999).

170. Seoh, M. L., Ng, C. H., Yong, J., Lim, L. & Leung, T. ArhGAP15, a novel human RacGAP protein with GTPase binding property[1]. *FEBS Letters* **539**, 131–137 (2003).

171. Battram, A. M. *et al.* The Phosphatidylinositol 3,4,5-trisphosphate (PI(3,4,5)P3) Binder Rasa3 Regulates Phosphoinositide 3-kinase (PI3K)-dependent Integrin αIIbβ3 Outside-in Signaling. *Journal of Biological Chemistry* **292**, 1691–1704 (2017).

172. Li, X. *et al.* Mutually inhibitory Ras-PI(3,4)P2 feedback loops mediate cell migration. *Proc. Natl. Acad. Sci. U.S.A.* **115**, (2018).

173. Posor, Y. *et al.* Spatiotemporal control of endocytosis by phosphatidylinositol-3,4-bisphosphate. *Nature* **499**, 233–237 (2013).

174. Bement, W. M. *et al.* Activator–inhibitor coupling between Rho signalling and actin assembly makes the cell cortex an excitable medium. *Nat Cell Biol* **17**, 1471–1483 (2015).

175. Ryan, G. L., Petroccia, H. M., Watanabe, N. & Vavylonis, D. Excitable Actin Dynamics in Lamellipodial Protrusion and Retraction. *Biophysical Journal* **102**, 1493–1502 (2012).

176. Michaud, A. *et al.* A versatile cortical pattern-forming circuit based on Rho, F-actin, Ect2, and RGA-3/4. *Journal of Cell Biology* **221**, e202203017 (2022).